


nature electronics



**A 3D twist on
stretchable electronics**

Three-dimensional integrated stretchable electronics

Zhenlong Huang^{1,2,9}, Yifei Hao^{1,3,9}, Yang Li^{1,9}, Hongjie Hu⁴, Chonghe Wang¹, Akihiro Nomoto¹, Taisong Pan², Yue Gu⁴, Yimu Chen¹, Tianjiao Zhang⁴, Weixin Li^{1,3}, Yusheng Lei¹, NamHeon Kim¹, Chunfeng Wang^{1,5}, Lin Zhang¹, Jeremy W. Ward⁶, Ayden Maralani⁷, Xiaoshi Li¹, Michael F. Durstock⁶, Albert Pisano^{1,4,7}, Yuan Lin² and Sheng Xu^{1,4,7,8*}

Stretchable electronics is an emerging technology that creates devices with the ability to conform to nonplanar and dynamic surfaces such as the human body. Current stretchable configurations are constrained to single-layer designs due to limited material processing capabilities in soft electronic systems. Here we report a framework for engineering three-dimensional integrated stretchable electronics by combining strategies in material design and advanced microfabrication. Our three-dimensional devices are built layer by layer through transfer printing pre-designed stretchable circuits on elastomers and creating vertical interconnect accesses using laser ablation and controlled soldering. Our approach enables a higher integration density on stretchable substrates than single-layer approaches and allows new functionalities that would be difficult to implement with conventional single-layer designs. Using this engineering framework, we create a stretchable human-machine interface testbed that is based on a four-layer design and offers eight-channel sensing and Bluetooth data communication capabilities.

Stretchable electronics could be of use in applications related to healthcare^{1–4}, consumer electronics^{5–10} and human-machine interfaces^{11–13}. Stretchable electronic devices are typically implemented in large-area, low-density, single-layer formats^{14,15}. However, these configurations limit the level of integration and functional complexity that can be achieved. The ability to incorporate commercial-off-the-shelf (COTS) components with stretchable substrates would enable the use of decades of integrated circuit development in complementary metal-oxide-semiconductor technology¹⁶. Moreover, it is expected that the surface density of functional components in a single layer will reach a bottleneck because of fabrication and mechanical design constraints^{17,18}. Although it is possible to integrate more functions by combining all the chips of a system into one or two chips, an alternative approach could be to integrate the existing components into multiple layers, thereby creating stretchable electronics in three dimensions. The major challenge for three-dimensional (3D) stretchable electronic systems, however, is the efficient and scalable formation of complex and robust interlayer electrical connectivity.

In this Article, we report a framework for 3D integrated stretchable systems with interlayer electrical connectivity that enables a higher level of integration than single-layer approaches. Our approach builds the stretchable electronics layer by layer through transfer printing pre-designed stretchable circuits on each layer of elastomer. Vertical interconnect accesses (VIAs) formed by laser ablation and controlled soldering allow the connection density to accommodate state-of-the-art circuit components and functions.

Design and characterization of the 3D stretchable system

The framework is demonstrated in a device testbed with a stretchable four-layer design. The structure and circuit design is shown in Fig. 1a. The device is built layer by layer (see Methods for details). Each layer employs an ‘island-bridge’ layout to accommodate the mechanical mismatch between the rigid functional components and the silicone elastomer matrix¹⁹. Each ‘island’ hosts a functional component, ranging from electrodes and sensors, to active (amplifiers and radiofrequency components) and passive (resistors, capacitors and inductors) components. The components are interconnected in-plane by stretchable ‘bridges’—bilayers of Cu/Polyimide (PI) thin film in a serpentine geometry that buckles in response to matrix deformation. VIAs for interlayer electrical connection are created from conductive fillings in craters in silicone. The dashed lines in Fig. 1a indicate the distribution and positions of the VIAs in the system, with the cross-sectional schematics shown in Supplementary Fig. 1. Between the layers, an ultralow modulus silicone is used to encapsulate the components for mechanical robustness and minimize constraints on the stretchability of the overall device. The overall device dimensions are approximately 30 × 19 × 2 (L × W × T) mm³ (Fig. 1b), which is comparable to a U.S. dollar coin. The final system achieved stretchabilities of 50%, 35% and 20% in the vertical, horizontal and equal-biaxial directions, respectively (Supplementary Figs. 2–4), which are sufficient to accommodate typical skin deformations (~20%)¹. The device deformation is highly reversible and can be stretched for more than 2,000 cycles (Supplementary Fig. 5). The exceptional compliance and robustness of the system when twisted and poked are shown in Fig. 1b.

¹Department of Nanoengineering, University of California San Diego, La Jolla, CA, USA. ²State Key Laboratory of Electronic Thin films and Integrated Devices, University of Electronic Science and Technology of China, Chengdu, China. ³Biomedical Engineering, School of Precision Instrument and Opto-electronics Engineering, Tianjin University, Tianjin, China. ⁴Materials Science and Engineering Program, University of California San Diego, La Jolla, CA, USA. ⁵The Key Laboratory of Materials Processing and Mold of Ministry of Education, School of Materials Science and Engineering, School of Physics & Engineering, Zhengzhou University, Zhengzhou, China. ⁶Soft Matter Materials Branch, Materials and Manufacturing Directorate, The Air Force Research Laboratory, Wright-Patterson Air Force Base, OH, USA. ⁷Department of Electrical and Computer Engineering, University of California San Diego, La Jolla, CA, USA. ⁸Department of Bioengineering, University of California San Diego, La Jolla, CA, USA. ⁹These authors contributed equally: Zhenlong Huang, Yifei Hao, Yang Li. *e-mail: shengxu@ucsd.edu

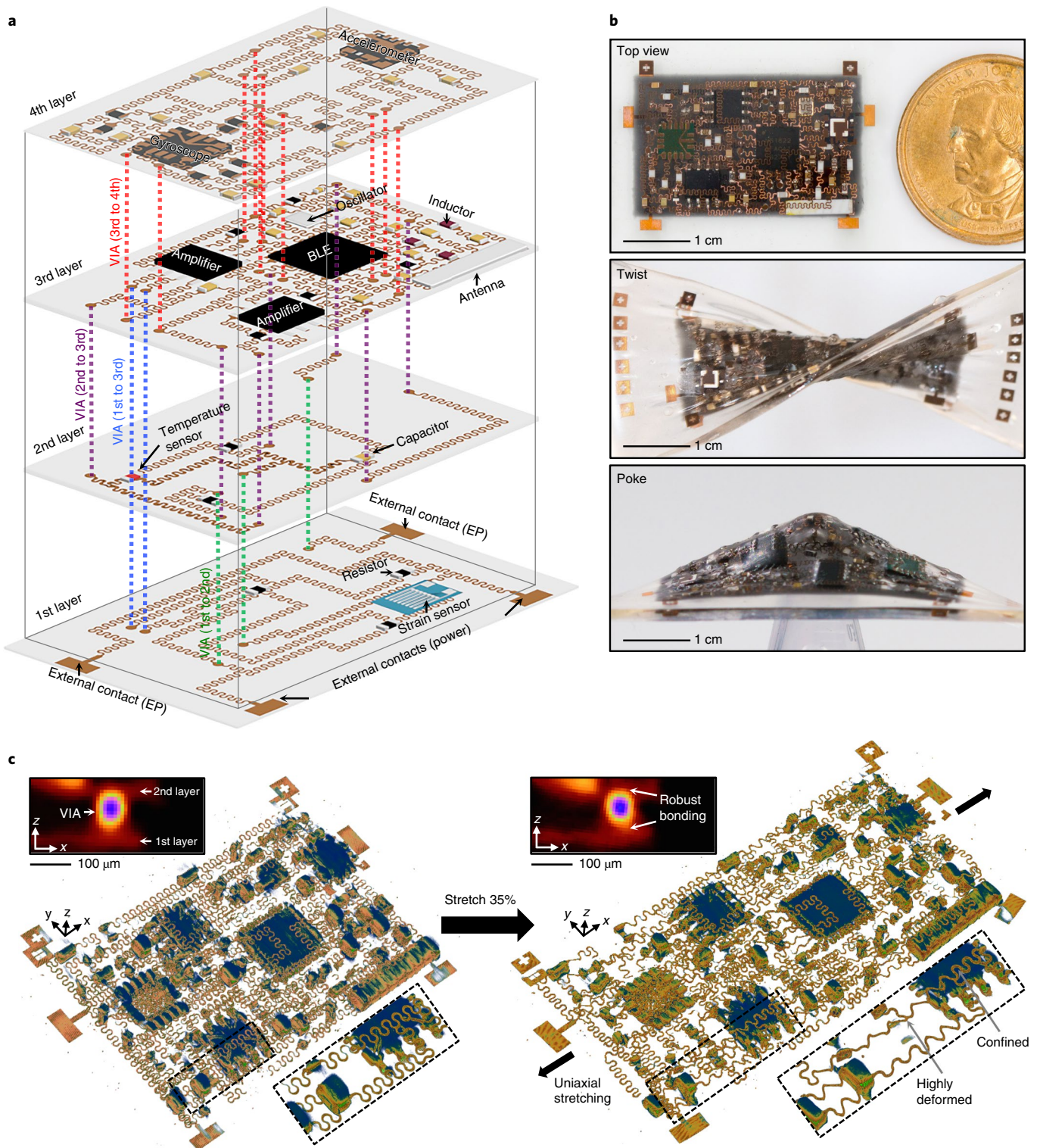


Fig. 1 | Design and characterizations of a four-layer stretchable system. **a**, Exploded schematics of the system that is fabricated layer by layer. VIAs are used for interlayer electrical connections. Key components in each layer are labelled. BLE, Bluetooth; EP, electrophysiological potential. **b**, Optical micrographs of the system when freestanding (top), twisted at 90° (middle) and poked with a dome height of ~8 mm (bottom), highlighting its superb mechanical compliance and robustness. **c**, XCT images of the system at 0 (left) and 35% (right) uniaxial tensile strain. Insets at the top show the zoomed-in cross-sectional views of a VIA between two adjacent layers. The VIA connection remains intact under stretching. The inset at the bottom right highlights the interlayer mechanical coupling that leads to non-uniform deformation in the Cu interconnects. The XCT imaging resolution is 9 μm .

To visualize the mechanical behaviour of the multilayer system, we imaged the 3D configuration of the device at 0 and 35% strain with micro X-ray computed tomography (micro-XCT) (Fig. 1c).

A major difference from the single-layer configuration is the mechanical coupling between layers in the 3D integrated device. The chips/interconnects can add mechanical loading to the local

elastomer matrix and result in non-uniform strain in nearby layers. Strain is concentrated in areas between the rigid components, reaching its minimum in areas directly above or below the rigid components. Therefore, the embedded serpentine interconnects are not deformed uniformly across the entire device area. The size of the non-uniformly strained area is dependent on two factors: the size of the rigid component and the vertical separation between the rigid component and the stretchable interconnect. Detailed experimental and finite-element analysis (FEA) results show that the non-uniformly strained magnitude increases with increasing the component size and decreasing the separation (Supplementary Fig. 6). To mitigate the constraints among the layers, as presented in Supplementary Note 1, potential solutions include reducing the dimensions of the rigid chips by using unpackaged bare dies (Supplementary Fig. 7) and adding a strain isolation layer with an ultralow Young's modulus (for example, liquid) between the adjacent layers²⁰, as verified by the FEA results (Supplementary Fig. 8).

Under stretching, the silicone shows sufficient adhesion to the silicone layer that has already been cured. When the strain reached 400% in the debonding test, there was no deviation of the strain-load density curve²¹, which meant the pre-designed delamination did not propagate (Supplementary Note 2 and Supplementary Figs. 9,10). The silicone also shows strong adhesion to the buried chips. Delamination appears first on connecting pins at around 40% tensile strain. Ultraviolet ozone treatment of the chips helps enhance the bonding between the chips and the silicone (Supplementary Fig. 11). Cross-sectional XCT images of the device (Fig. 1c top-left insets) depict the VIA behaviour. Under 0 and 35% strain, the VIAs show no delamination or noticeable deformation. A complete cross-sectional view shows the four-layer Cu interconnect layout, the active and passive components and the interlayer VIAs (Supplementary Fig. 12).

Selective laser ablation for VIA formation

To form the VIAs, the elastomer matrix needs to be selectively removed with micrometre-scale precision before a conductive filling is deposited. The VIA size needs to be small to minimize stress localization. Moreover, the VIAs are built in a complex material system—silicone and PI on top of Cu pads in our case (Supplementary Fig. 1e). Since silicones are notoriously difficult to etch, we employ laser ablation, a direct-write mass removal method²², as a fast, precise and scalable VIA formation strategy. With a beam waist of 25 μm and a depth of focus of 600 μm , the laser can etch a VIA in silicone with a depth of 100 μm and a diameter as small as 45 μm (Supplementary Figs. 13,14). The laser ablation process is also used to pattern the Cu serpentine interconnects with a line width of 25 μm , streamlining the fabrication process (Supplementary Fig. 15).

The selective mass removal required for VIA formation is achieved by combining three strategies. First, the laser wavelength is selected to have a low impact on the structural integrity of Cu. The laser absorption by Cu at 1,064 nm is about eight times weaker than at 532 nm (ref. ²³), as shown in Fig. 2a. Second, due to the low absorption in silicone with the visible–infrared range nanosecond laser, we incorporate dyes in the elastomer to enhance the absorption and therefore lower the ablation threshold. Silicone that incorporates black dye (3% wt, Silc Pig, Smooth-On, Supplementary Fig. 16) is found to have the highest absorption at 1,064 nm. Femtosecond lasers can also be used without dye due to the nonlinear absorption at high intensities^{24,25}. Third, the laser pulse fluence is optimized by tuning the optical attenuation (Supplementary Fig. 17) and its effect on different materials is studied (Supplementary Fig. 18). Below a threshold fluence value, laser excitation will not provide sufficient thermal energy for the material ablation. The threshold fluence values for different materials are summarized in Fig. 2b (1,064 nm) and Supplementary Fig. 19 (532 nm). The ablation threshold for Cu varies from 0.34 mJ with a 1,064 nm laser to 0.02 mJ with a 532 nm

laser, corresponding to the Cu absorption at these wavelengths discussed above. The thresholds for black silicone and polyimide with a 1,064 nm laser are 0.1 mJ and 0.05 mJ, respectively. Therefore, pulse fluence values in the range 0.1–0.34 mJ allow selective removal of the PI and black silicone in the presence of Cu (Supplementary Figs. 14,20).

We demonstrate three types of VIAs with 1,064 nm nanosecond pulsed laser ablation: through VIA (open on both sides), buried VIA (open on neither side) and blind VIA (open only on one side of the stretchable circuit). Fabrication is carried out on a soft multilayered silicone–Cu structure (Supplementary Fig. 21). The VIA width and depth are controlled by the laser writing pattern and the number of ablation pulses. Increasing the number of pulses increases the ablation of all materials. With well-designed process parameters (Supplementary Fig. 22), sophisticated VIA structures are demonstrated (Supplementary Fig. 23). The inset of Fig. 2c shows the tilted view of the through VIA with an increasing diameter from 300 μm at the first layer to 600 μm at the fourth layer, ensuring a sufficient contact area between the Cu pad and the conductive fillings ($\text{Sn}_{42}\text{Bi}_{57.6}\text{Ag}_{0.4}$ solder paste in this case). Flux solution is used to remove the Cu oxide layer generated by laser heating (Supplementary Figs. 24,25), which would otherwise weaken the solder bonding. The solder paste is dispensed into the VIAs by screen-printing (Supplementary Fig. 26). An appropriate reflow temperature allows complete melting of the solder paste to form robust bonding between the rigid chips and the interconnects, yet without melting or affecting the existing VIAs in previous layers (Supplementary Fig. 27). The bonding between the chip and interconnect pad is so strong that it shows no evidence of failure before the serpentine interconnect itself breaks at a tensile strain of 138% (Supplementary Note 3 and Supplementary Figs. 28,29). The low thermal expansion coefficient of the Ecoflex ($284.2 \pm 1.8 \text{ ppm}^\circ\text{C}^{-1}$)²⁶ at the reflow temperature (150 $^\circ\text{C}$ in this study) leads to thermal expansion of only 3.69% (volume) and 1.2% (linear) in the substrate. In the vertical direction, due to the thinness of the Ecoflex films (200 μm), the thermal expansion will yield only to 2.4 μm , which can be accommodated by the elastomer itself. In the lateral directions, since the Ecoflex layers are bonded covalently to the existing layers, the in-plane expansion can be safely ignored. Furthermore, as the expansion is isotropic it will not shift the chips along any specific direction. This ensures that the thermal expansion will not damage the already-soldered parts (Supplementary Fig. 27). Figure 2c–e shows electron-dispersive spectroscopy mappings of the three types of VIAs. The Cu layers are separated by dielectric silicone elastomers and connected only at the VIAs by the solder–Cu alloy. Due to high conductivity of the solder and low contact resistance between the solder and Cu interconnects, the VIA shows an ultralow resistance (68.7 m Ω) that is strain-invariant, which represent clear advantages over VIAs formed by other approaches^{27,28} (Supplementary Note 4 and Supplementary Fig. 30).

A 10-layer stretchable heater is fabricated to demonstrate the scalability of this process. Figure 2f shows the top view of the 10-layer device (see Supplementary Fig. 31 for a detailed schematic illustration of the device structure). The device is designed to have a decagram layout: each layer has a heater at the midpoint of the connection line and a VIA at the vertex. The thermal image of the decagram heater in operation is captured in Fig. 2g and Supplementary Fig. 32. The temperature difference at each heater location originates from the different layer depths from the top surface of the device. A heat sink underneath the device effectively reduces heat accumulation around every heater and thus manifests their temperature differences. Figure 2h shows a thermal image of the device under 30% uniaxial strain; the temperature difference becomes insignificant due to the decreased depth variations of each heater and also reduced thermal coupling to the bottom heat sink.

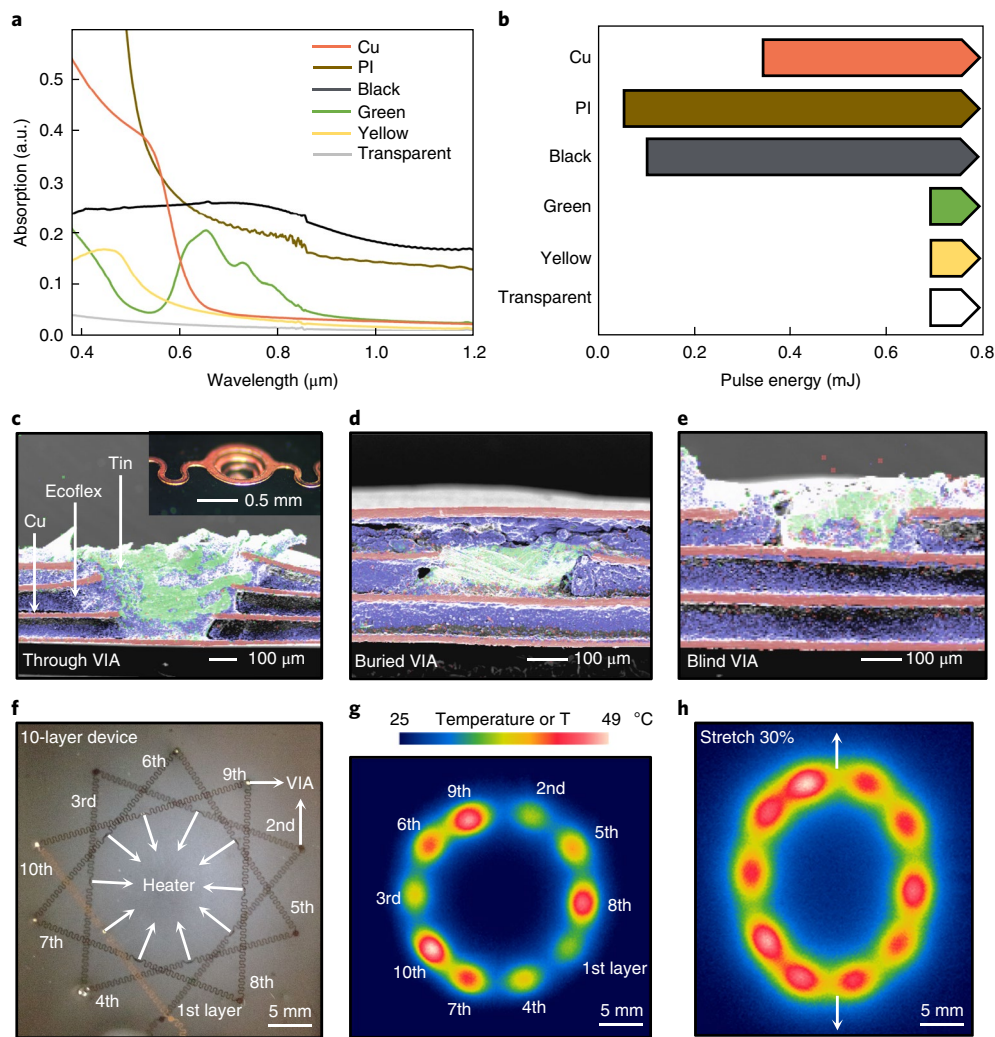


Fig. 2 | VIA fabrication and a 10-layer decagram stretchable heater demonstration. **a**, Absorption spectrum of Cu²³, PI and silicone modified with different dyes, which serves as the foundation for selective laser ablation. **b**, Laser ablation thresholds for Cu, PI and silicone with different dyes. **c–e**, Cross-sectional electron dispersive spectroscopy mapping graphs of through (**c**), buried (**d**) and blind (**e**) VIAs fabricated in silicone elastomers. Silicone elastomer (blue) provides insulation between Cu (pink) in each layer and VIAs form electrical connections through the conductive filling (green). The non-uniform shapes of the VIAs are caused by the cross-sectional sample preparation processes. The inset in **c** shows a tilted view of the through VIA. **f**, Optical image of the 10-layer decagram stretchable heater. All layers are connected in series, with a total thickness of 1.1 mm. Each layer has a heater in the middle of the Cu interconnection and a VIA at the vertex of the decagram. **g**, The thermal image of the decagram device with 59.3 mW power for each heater. The depth of the heater embedded in the elastomer decreases from the first layer to the tenth layer. Therefore, the observed temperature increases in sequence. **h**, Thermal image of the decagram device under 30% uniaxial stretching. The observed temperature differences become insignificant due to reduced depth variations and thermal coupling to the bottom heat sink.

Multi-channel data acquisition for vital sign monitoring

The 3D integration enables not only high component densities in stretchable electronics, but also new functions that are challenging to implement with conventional single-layer designs of a reasonable footprint size. An example of such new functions is an eight-channel sensing system with Bluetooth for wireless communication, which involves a large number of COTS components and complex wiring. In the device tested as designed in Fig. 1a, we have incorporated a strain sensor in a Wheatstone bridge scheme and releasable contact pads for power and local field potentials (first layer), a temperature sensor with a low-pass filter (second layer), a system-on-chip Bluetooth integrated circuit with a 2.4 GHz antenna, an impedance matching circuit and a local field potential amplifier (third layer), and a gyroscope and an accelerometer (fourth layer). Passive components such as resistors, capacitors and inductors are strategically distributed among the four layers to minimize the strain

localization and series resistance in the stretchable interconnects. The four-layer device was fabricated layer by layer through transfer printing (Supplementary Fig. 33). The VIA diameter is 500 μm to accommodate the maximum interconnection distortion of $\sim 150 \mu\text{m}$ (Supplementary Fig. 34) and maximum alignment error of $\sim 120 \mu\text{m}$ (Supplementary Figs. 35,36) during transfer printing.

The device is designed to record electrophysiological signals from the human body when attached to the skin by van der Waals forces. Intimate contact with the skin is key to acquiring a high signal-to-noise-ratio due to its low interfacial parasitic capacitance. The device is connected with two $8 \times 8 \text{ mm}^2$ soft electrodes, as shown in Fig. 3a. Each electrode is made from a multiwall carbon nanotube (CNT)/silicone (Silbione, Elkem Silicones) composite. Because of its low Young's modulus (40 kPa, Supplementary Fig. 37) relative to that of human epidermis (140 to 600 kPa)¹, the CNT/silicone composite conforms to the skin without causing much

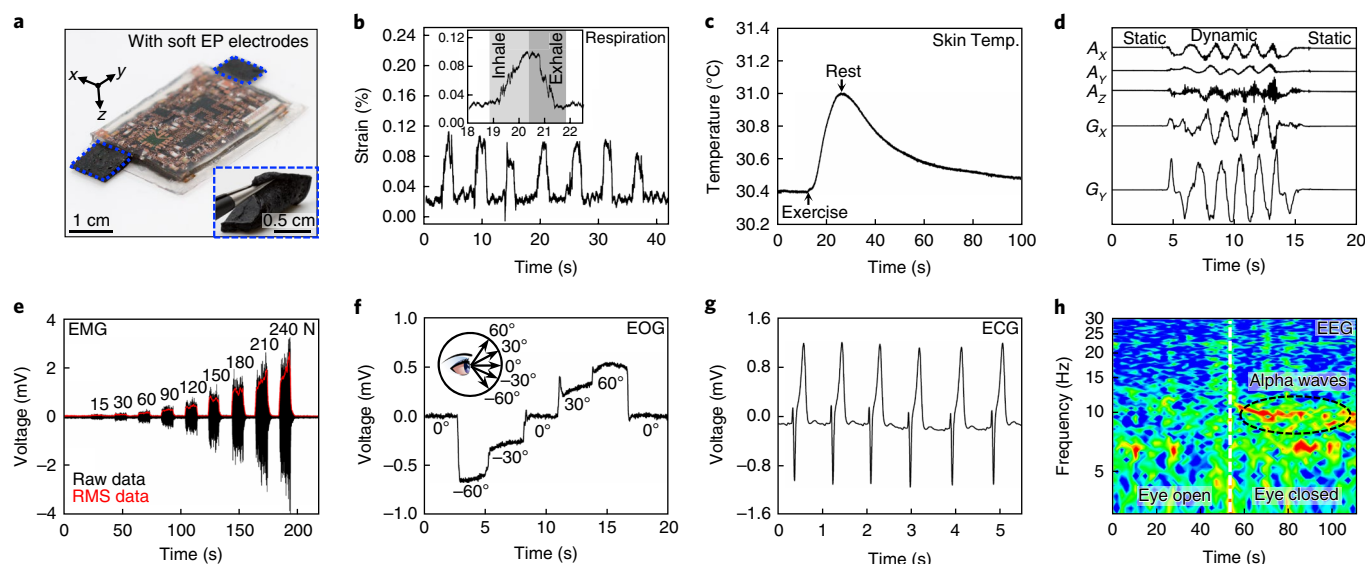


Fig. 3 | Optical images and operational data from the four-layer stretchable device. **a**, An optical image of the system integrated with CNT/silicone electrodes for EP measurements. The inset shows an optical image of a deformed electrode. The sensors are soft and sticky, and can achieve conformal contact to the skin without any gels. **b–d**, Signal measurements with the device mounted on the chest. **b**, Measured bending strain corresponding to repeated inhalation and exhalation. An expanded view of one cycle is given in the inset. **c**, Measured skin temperature change corresponding to exercise and rest. **d**, Measured acceleration (A_x , A_y and A_z) and angular velocity (G_x and G_y) corresponding to walking. **e**, EMG signals acquired from the forearm with different grasping forces. The root mean square (RMS) was calculated to quantify the response amplitude. **f**, EOG signals acquired from the side of the head with different gazing angles. **g**, ECG signals acquired from the chest. **h**, EEG signals acquired from the forehead with the eyes open and closed. The strong alpha waves between 8–13 Hz indicate that the brain is in an idling state when the eyes are closed.

discomfort, thus removing the requirement for conductive gels as a contact promoter. Its high electrical conductivity, low piezoresistance (Supplementary Fig. 38) and long-term stability ensure a high signal-to-noise ratio (Supplementary Fig. 39) and a lifetime of more than half a year (Supplementary Fig. 40). Skin fibroblast cell viability experiments have confirmed biocompatibility of the CNT/silicone composite electrode to the skin (Supplementary Note 5). The CNTs are strongly attached to the tacky Silbione matrix, thus removing the risk of inhalation.

Powered by a 3 V pouch cell, the multi-functional soft system can be used to simultaneously record human respiration, skin temperature and body motion when mounted on the chest. The chest movement when breathing is detected by the strain sensor (Fig. 3b). The skin surface temperature is recorded by the temperature sensor, showing a rapid increase with physical exercise and slow recovery with rest (Fig. 3c). Signals from the accelerometer along the x , y and z axes (A_x , A_y and A_z) and the gyroscope along the x and y axes (G_x and G_y) are recorded during walking (Fig. 3d). The device can communicate wirelessly via Bluetooth Low Energy 4.0 technology with a smartphone or a laptop at distances of up to 10 m. The received signal strength indicator varies from -55 dBm at 0.5 m to -80 dBm at 10 m (Supplementary Fig. 41). The total power budget of the four-layer system is around 35.6 mW (Supplementary Figs. 42,43). The gyroscope chip consumes 20.4 mW and generates the greatest amount of heat when in operation (Supplementary Figs. 44,45). Even without special heat management measures, the gyroscope reaches a local temperature only 2.3°C higher than in the resting state, making it compatible with the human skin (Supplementary Note 6).

The local field potential amplifier can be applied to record various electrophysiological signals. When mounted on the forearm, an electromyograph (EMG) is recorded with different grasping forces, calibrated with a commercial hand dynamometer (Fig. 3e). The root mean square value is calculated to quantify the increasing EMG signal intensity. When mounted on the side of the head, an

electrooculograph (EOG) is acquired with gazing angles from -60° to $+60^\circ$ (Fig. 3f). When mounted on the chest or abdominal area, an electrocardiograph (ECG) is recorded with the P, Q, R, S and T waveforms clearly identified (Fig. 3g and Supplementary Fig. 46). When mounted on the forehead, an electroencephalograph (EEG) is recorded, with distinguishable signals during mental exercise with open eyes and relaxation with closed eyes (Fig. 3h). Alpha rhythms with frequencies from 8 to 13 Hz in the EEG during the closed-eye state clearly indicate the activity of the visual cortex in an idle state^{29,30}. Additional experimental details about the electrophysiological sensing procedure and data processing are given in the Supplementary Information (Supplementary Figs. 47–51). The system exhibits a stable working state under stretching. Quantitative evaluation of the interconnects and the multilayered system shows that the strain has minimal impact on the device performance (Supplementary Note 7 and Supplementary Figs. 52–57). The circuit design, device workflow and components used in the system are summarized in the Supplementary Information (Supplementary Figs. 58–60).

The capability of building multilayered stretchable electronic systems opens up the possibility of implementing functions with chips that were previously impossible using single-layer designs. For example, ball-grid array (BGA) chips, which are essential for higher-speed data communications in microprocessors and random access memories, have such a high pin density that are challenging to realize with a single-layer electronic design. Multilayered stretchable circuits and systems may offer a potential solution in this regard. Relevant work is being carried out and will be reported in separate follow-up studies.

Wireless high-degree robotic arm control

An exemplary application of the 3D integrated stretchable system is a non-invasive multifunctional human–machine interface. The rich variety of signals obtained from the human body can be used as a source of commands for controlling robotics and prosthetics^{13,31,32}.

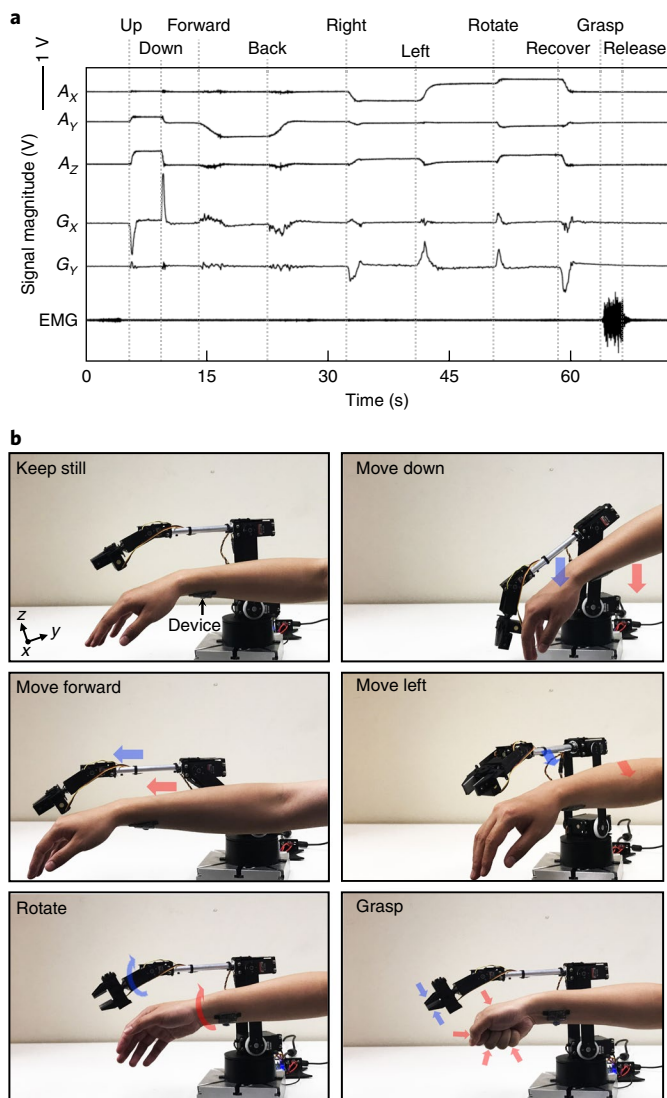


Fig. 4 | Wireless robotic arm control. **a**, Acceleration (A_x , A_y and A_z), angular velocity (G_x and G_y) and EMG data acquired from a variety of arm motions with the device mounted on the forearm. The acceleration is used to control the translational movement, the angular velocity is used to control the rotational movement and the EMG signals are used to control the grasping of the robotic arm with six degrees of freedom, as shown in Fig. 4. With real-time wireless data communication and algorithmic analysis, the robotic arm can quickly identify and imitate the gestures of the human arm.

In the test, the stretchable four-layer device is secured on a human forearm through van der Waals forces, and used to wirelessly control a robotic arm (Lynxmotion AL5D arm with upgraded wrist rotation and SSC-32U USB board communications, Supplementary Fig. 61). Six different channels of signals acquired on the forearm, including three-channel acceleration, two-channel angular velocity and EMG signals, are used to control the robotic arm with six degrees of freedom, as shown in Fig. 4. With real-time wireless data communication and algorithmic analysis, the robotic arm can quickly identify and imitate the gestures of the human arm.

Conclusions

We have reported system design and fabrication methods that provide a framework for building 3D integrated stretchable electronics. This framework enables a high level of device integration and

creates the opportunity to build devices for use in applications that require more complex interconnect layouts than those currently achievable in single-layer designs. These principles could also be applied to stretchable systems built with other material ensembles and more sophisticated chips and components. Using our framework, we have developed stretchable, compact multi-channel sensors that can be used to extract an array of signals from the human body in wireless operation mode. The sensing system could be of value in the development of smart connected healthcare, wireless control schemes for human-machine interfaces and, more broadly, the Internet of Things.

Methods

Design rationale for the multifunctional circuit. A Bluetooth chip (chip 22, Supplementary Fig. 60) collected eight channels of signals simultaneously from the accelerometer (along the x , y and z directions), gyroscope (along the x and y directions), strain sensor, temperature sensor and electrophysiological module. A 10-bit analog digital converter (ADC) then converted the analogue signals of each channel to digital signals. Capacitors of $0.1\ \mu\text{F}$ (chip 15) were used to decouple the power supply. All clocks in the Bluetooth chip were derived from the 16 MHz oscillator (chip 23). The Bluetooth chip transmitted the signals via a 2.4 GHz antenna (chip 6). The signals could be received at a distance of 10 m by a separate Bluetooth chip.

The strain sensor (chip 1) was embedded in a Wheatstone bridge that was specially designed with a resistance of approximately $350\ \Omega$. The bridge output signals to the amplifier (chip 17, upper). After amplification by a factor of 820, the signal for zero-strain was $1.97\ \text{V}$; this was then transmitted to the Bluetooth chip.

The electrophysiological module acquired signals from the Cu pads in the first layer through a filter comprised of chips 15, 20 and 21 at the top-right corner of the third layer in Supplementary Fig. 60. The signal was amplified (chip 17, lower) and then collected by the Bluetooth chip. Using this amplifier and the 10-bit ADC of the Bluetooth chip, the voltage resolution of the device is $\sim 3.6\ \mu\text{V}$. Typical signal amplitudes were $\sim 1\ \text{mV}$ for ECG, $\sim 1\ \text{mV}$ for EMG and $\sim 50\ \mu\text{V}$ for extracranial EEG, which are all much larger than the voltage resolution of the device and confirm the high signal-to-noise ratio of the measurements.

The temperature sensor was a negative temperature coefficient thermistor. The signal was passed through a filter comprised of chips 4 and 5, and then transmitted to the Bluetooth chip.

The accelerometer (chip 30) could generate three channels of acceleration data along three orthogonal axes. All channels were filtered through a bypass capacitor (chip 15) before being fed into the Bluetooth chip.

The gyroscope was decoupled by chips 15 and 21 at the bottom-left corner of the fourth layer in Supplementary Fig. 60. Two channels of angular velocity data were filtered by a bandpass filter that was connected to the gyroscope in series.

The topological structure design of the device aims to minimize the interconnect complexity in each layer and the number of VIAs between the layers. The strain sensor and temperature sensor were placed in the first two layers, which were close to the skin to minimize any possible signal attenuation. To reduce the surface roughness of the first and second layers of the device, due to the height variation of the chips, the chips in these two layers were chosen to have a thickness less than the encapsulating Ecoflex. Specifically, chips with a 01005 packaging that had a thickness of $0.13\ \text{mm}$ were selected. For the third and fourth layers, we chose chips with a 0603 packaging, $0.8\ \text{mm}$ in width and $1.6\ \text{mm}$ in length, to simplify the bonding process.

Mechanical pattern design of the serpentine electrodes. A horseshoe serpentine design was employed as the interconnect between the components, with an external diameter (D) of $0.6\ \text{mm}$, an internal diameter (d) of $0.3\ \text{mm}$, a curvature (θ) of 220° , a ribbon length (L) of $0.12\ \text{mm}$ and a ribbon width (W) of $0.15\ \text{mm}$, as shown in Supplementary Fig. 62. The total height (h) of each horseshoe was $0.867\ \text{mm}$.

There were three criteria for choosing these parameters. First, the width and the narrowest part in the serpentine should be wider than the resolution of the laser ablation ($25\ \mu\text{m}$). Second, the total height of the horseshoe interconnect should be suitable for the density of chip pins. The space between adjacent pins of the chips should be sufficient to accommodate the interconnects. Third, the values of d/W , L and θ should be as large as possible to maximize the device's stretchability^{35,34}. The detailed quantitative electrical evaluations of the interconnect under strain are shown in Supplementary Note 7 and Supplementary Figs. 52–54.

Fabrication of the interconnect network. A layer of poly(methyl methacrylate) (PMMA) (495K, A6) was coated on the glass at a spin speed of $1,500\ \text{r.p.m.}$ for $30\ \text{s}$, then cured by soft baking on a hotplate at 150°C for $1\ \text{min}$. Next, spin-coating formed a $100\text{-}\mu\text{m}$ -thick layer of Ecoflex (Smooth-On, 1:1) over the PMMA. The Ecoflex was cured at room temperature for two hours. A layer of polydimethylsiloxane (PDMS, Sylgard 184 silicone elastomer, 20:1) was coated on a separate clean glass slide at $3,000\ \text{r.p.m.}$ for $30\ \text{s}$, followed by curing in an oven at 110°C for $30\ \text{min}$. A Cu sheet ($20\text{-}\mu\text{m}$ -thick, Oak-Mitsui Inc.) was coated with

PI (from poly(pyromellitic dianhydride-co-4,40-oxydianiline) amic acid solution, PI2545 precursor; HD Microsystems) at 4,000 r.p.m. for 60 s, soft baked on a hotplate at 110 °C for 3 min, 150 °C for 1 min and then fully cured in a nitrogen oven at 300 °C for 1 h sequentially, and then transferred onto the surface of the prepared PDMS/glass substrate. The interconnect layout was designed using the AutoCAD software and input into the laser system for the Cu patterning. Next, a laser (wavelength 1,064 nm, pulse energy 0.42 mJ, pulse width 1 μ s, frequency 35 KHz and mark speed 500 mm s⁻¹) was used to ablate the Cu film into the designed pattern. Compared with traditional photolithography-based chemical etching methods, laser ablation is time efficient, chemical-free, and avoids the need for masks and a cleanroom environment (Supplementary Note 8). After removing the residual material, the Cu pattern was picked up by means of a water soluble tape (3M Inc.) for transfer printing onto a prepared Ecoflex/PMMA/glass substrate or the existing matrix of the device.

Assembly of the chip components. Both the Ecoflex substrate and interconnections on the water-soluble tape (exposing the PI side of the Cu electrode) were activated by ultraviolet ozone for 3 min. For the first layer, the interconnection was directly laminated on the Ecoflex substrate and heated in an oven at 80 °C for 15 min to enhance the bonding between the PI layer and the Ecoflex. Then the water-soluble tape was removed by room-temperature tap water. After drying with an air gun, the Cu interconnection was cleaned by flux (WOR331928, Worthington Inc.) to remove the surface oxide layer and assist the formation of Cu/Sn alloy for enhanced electrical bonding. The Sn₄₂Bi_{57.6}Ag_{0.4} alloy paste (Chip Quick Inc., SMDLTLP-ND, low melting point of 138 °C) was screen-printed onto Cu pads with a shadow mask (thickness 75 μ m). Polished chips with reduced dimensions were aligned carefully on the Cu pads, reflowed by baking on a hotplate at ~150 °C for 5 min, and then cooled down to room temperature to attain good wetting properties.

VIA formation and aligned transfer printing. Concentrated colour pigments (Silc Pig, Smooth On, Inc.) were used to modify the absorptivity of silicone to allow selective etching of silicone versus Cu. Ecoflex part A was first mixed with the pigments (1.5% wt of the part A), followed by the addition of Ecoflex part B (A:B = 1:1 by weight). By spin coating, the existing circuit layer was fully encapsulated with a 100- μ m-thick layer of coloured silicone. A thin-film shadow mask was used to separate the external Cu pads (for EP and power contacts) from the silicone encapsulation. After removing the mask, the device was put in the oven at 80 °C for 30 minutes to fully cure the silicone.

Laser ablation was then used to create VIAs through the silicone. Laser ablation, a mass removal method that relies on coupling photon energy to materials, is highly suited to processing silicone elastomers. In comparison with lithography-based processes, it offers quick, precise and scalable direct-write capabilities (Supplementary Note 8). There are two things to be noted: first, the designed CAD VIA pattern should be aligned with the device; second, VIAs are formed by selectively removing the silicone without damaging the bottom Cu pad.

Strategies for laser alignment. Laser alignment was used to match the existing pattern in the sample to the pattern on the CAD design file that was processed by the laser. At least two alignment markers were added in each pattern. These markers indicated the x , y and theta positions of patterns in the camera of the laser cutting equipment. There were two ways to align both patterns, either by moving the sample using the mechanical stage or by changing the pattern location and orientation in the CAD design. In our study, we used the latter method because it was more accurate and convenient. Detailed procedures are listed below:

1. Each sample needed at least two alignment markers to identify its location coordinates (x , y and theta). These were added at point A (X_A , Y_A) and point B (X_B , Y_B) in both the sample pattern and the CAD design file.
2. Calibrate the laser ablation location in the camera. Once a laser ablation marker had been made on a dummy sample, we could see the actual ablation locations on the sample of points A and B from the CAD design. We then recorded the locations of the markers in the camera sight, which would be used as the reference positions.
3. To check the alignment discrepancy between the sample and the CAD design the sample with location points A and B was placed on the stage. By comparing these points with the reference positions, we could see the location difference between the position in the camera sight and the one on the CAD design file, (ΔX_A , ΔY_A) and (ΔX_B , ΔY_B).
4. Match the pattern location in the CAD file to the actual sample location, by shifting and rotating the pattern location on the CAD file to cancel the discrepancies (ΔX_A , ΔY_A) and (ΔX_B , ΔY_B).
5. Start laser ablation.

After the eliminating the location discrepancy between the patterns in the CAD design and the actual sample, we started laser cutting using the parameters discussed in the text above.

Strategies for selectively etching silicone. Selective etching by controlling the laser process parameters allowed ablation of the silicone without damaging the Cu underneath. To achieve this, the silicone was first modified with black pigments to

increase its laser absorption. Second, a suitable laser wavelength was chosen. Cu has much lower absorption in the near-infrared region than at the other common laser wavelengths, such as green or ultraviolet, as shown in Fig. 2a. Therefore, a laser with a wavelength of 1,064 nm was chosen to reduce potential ablation of Cu. Finally, the laser ablation parameters were systematically studied, as shown in Fig. 2b and Supplementary Fig. 18. The optimum laser parameters to selectively etch black silicone were determined to be pulse energy 0.14 mJ, pulse width 1 μ s, frequency 35 KHz and mark speed 500 mm s⁻¹. With well-designed laser writing patterns (Supplementary Fig. 22), the etched silicone VIA diameter can be as small as ~45 μ m, with an aspect ratio of ~2 and a silicone etching rate of ~1 μ m per etching cycle.

After 100 cycles of laser etching, VIAs were drilled through the silicone to expose the Cu pad underneath. During the high-temperature laser ablation process, oxide formed on the Cu pad surface and must be removed by flux to avoid it retarding the formation of alloy between the solder paste and the Cu pad that could weaken the bonding strength at the interface. For VIAs with small diameters (45–500 μ m), because of the hydrophobicity of the elastomeric surface, isopropanol alcohol (IPA) was mixed with the flux to improve the wetting and cleaning outcomes, as shown in Supplementary Figs. 24,25. By screen printing, the VIAs were fully filled with Sn₄₂Bi_{57.6}Ag_{0.4} solder paste. With mild heating on the hotplate at 150 °C for 5 minutes, the paste in the VIAs was transferred into tin pillars, which were bonded to the bottom Cu pads with good wetting properties.

The alignment of the subsequent layer of VIA patterns with the existing island-bridge matrix was achieved by transfer printing under a microscope with an integrated positioning system, as shown in Supplementary Fig. 35. After being picked up by the water-soluble tape, the new layer was attached to a PDMS/glass substrate to prevent it from curling. The existing matrix was placed on a thick Ecoflex substrate (thickness 5 mm) to achieve a soft contact and avoid any potential damage to the device. Ultraviolet ozone was used to activate both the new layer and the existing matrix for 3 min. Using the alignment markers and the positioning system, the new layer was aligned with the existing matrix. As Ecoflex was stickier than PDMS, the new layer can be transferred from the PDMS substrate to the Ecoflex matrix, which was then heated in an oven at 80 °C for 30 min before dissolving the water-soluble tape. The VIA structure, as shown in Supplementary Fig. 1e, has a circular Cu pad in the bottom layer, a tin pillar through the silicone, an open circular Cu pad in the top layer, and a tin cap. The tin cap is formed by screen printing the tin paste followed by heating on the hotplate to bond the tin pillar to the top Cu pad.

Device overall structure design. Mechanical coupling between the layers, which is important in determining the mechanical performance of the 3D stretchable electronics, was studied by combined experimental and theoretical methods. Two factors were studied: the separation between the interconnect and an adjacent overlying chip, and the non-constrained length of an interconnect between the chips (Supplementary Fig. 6). With increasing separation, the system-level stretchability first increases due to the decreased coupling effect, and then plateaus at a value that is intrinsic to the single-layer device (Supplementary Fig. 6c). The dependence on the non-constrained interconnect length follows a similar trend (Supplementary Fig. 6e). For the multilayer design, a balance was achieved between stretchability and the physical dimensions of the device.

For the four-layer stretchable system, the first two layers were fully encapsulated with silicone (Ecoflex, Smooth-On, Young's modulus E = 60 kPa) that helped the Cu interconnects recover after stretching. The third and fourth layers, which had a number of thicker chips, were integrated in such a way that the thick chips were positioned to avoid them stacking directly on top of each other to attain the minimum overall device thickness. These two layers were encapsulated with a solid silicone elastomer with an ultralow modulus (Silbione RT, Gel 4717 A/B, Bluestar Silicone, E = 5 kPa) with a core/shell structure to minimize interfacial strain and improve the overall stretchability at the system level³⁵.

For the ten-layer stretchable system the device had one heater in each layer and one VIA at each corner. The heaters in the layers were connected by the VIAs in series and powered by a d.c. supply.

Silbione/multiwalled carbon nanotubes (CNTs) composites for EP sensing.

As a first step, CNTs (1% wt of the Silbione part A) were mixed with Silbione part A (Silbione RT, Gel 4717 A/B, Bluestar Silicone). After stirring for two hours, Part B was added (A:B = 1:1 by weight). Glass with a layer of deposited polytetrafluoroethylene (PTFE) was used as the substrate to fabricate the composites. The thickness of the composites was controlled to be ~1 mm. After one day at room temperature, the fabricated electrode was fully cured and could be slowly removed from the substrate. The fresh electrodes were sticky enough to be directly attached on the skin for the EP sensing. Due to the high conductivity and stability of the CNTs³⁶, the electrodes can achieve high-quality signals for long-term EP monitoring. After several measurements, the electrodes could be recycled by cleaning with IPA to remove any dirt or dead skin cells.

Robot arm control system. The transmitting Bluetooth in the device collected signals from the accelerometer, gyroscope, strain, temperature and EP modules, and then packaged and sent these data to the receiving Bluetooth wirelessly

by protocol S130. The receiving Bluetooth was connected to a development board (BLE400), so that these packages could be delivered to a laptop through COM ports. Both Bluetooth chips were programmed by Keil μ Vision V5.14 to configure the resolution of the ADC and packaging logics. The resolution of the gyroscope was around $0.014^\circ \text{ s}^{-1}$ and the resolution of the accelerometer was around $300 \mu\text{g}$, which allowed the stretchable system to capture small movements of the human arm with high fidelity. The control software (FlowBotics Studio, RobotShop Inc.) in the laptop disassembled the package from the COM ports, calculated the sensing data and output the motion values through the SSC-32U USB board for each servo of the robot arm (Lynxmotion AL5D arm with upgraded wrist rotate). The set-up for the robot control system is shown in Supplementary Fig. 61. The latency of the multilayered system, including the sensing and wireless data transfer, was controlled to be less than 2 ms (Supplementary Note 9). The latency of the robotic arm, due to the commercial hardware (Lynxmotion AL5D) and accompanying control software (FlowBotics Studio), was around 273 ms (Supplementary Fig. 63). Therefore, the response time for the entire robotic arm control system was around 275 ms, which included the latency from sensing, Bluetooth transfer and the robot arm hardware and software.

Data availability. The data that support the plots within this paper and other findings of this study are available from the corresponding authors upon reasonable request.

Code availability. The code that supports the Bluetooth within this paper and other findings of this study are available from the corresponding authors upon reasonable request.

Received: 17 March 2018; Accepted: 13 July 2018;

Published online: 13 August 2018

References

- Kim, D.-H. et al. Epidermal electronics. *Science* **333**, 838–843 (2011).
- Lee, H. et al. A graphene-based electrochemical device with thermoresponsive microneedles for diabetes monitoring and therapy. *Nat. Nanotech.* **11**, 566–572 (2016).
- Miyamoto, A. et al. Inflammation-free, gas-permeable, lightweight, stretchable on-skin electronics with nanomeshes. *Nat. Nanotech.* **12**, 907–913 (2017).
- Wirthl, D. et al. Instant tough bonding of hydrogels for soft machines and electronics. *Sci. Adv.* **3**, e1700053 (2017).
- Keplinger, C. et al. Stretchable, transparent, ionic conductors. *Science* **341**, 984–987 (2013).
- Oh, J. Y. et al. Intrinsically stretchable and healable semiconducting polymer for organic transistors. *Nature* **539**, 411–415 (2016).
- Ota, H. et al. Highly deformable liquid-state heterojunction sensors. *Nat. Commun.* **5**, 5032 (2014).
- Kim, C.-C., Lee, H.-H., Oh, K. H. & Sun, J.-Y. Highly stretchable, transparent ionic touch panel. *Science* **353**, 682–687 (2016).
- White, M. S. et al. Ultrathin, highly flexible and stretchable PLEDs. *Nat. Photon.* **7**, 811–816 (2013).
- Jung, Y. H. et al. Stretchable twisted-pair transmission lines for microwave frequency wearable electronics. *Adv. Funct. Mater.* **26**, 4635–4642 (2016).
- Liu, Y. et al. Epidermal mechano-acoustic sensing electronics for cardiovascular diagnostics and human–machine interfaces. *Sci. Adv.* **2**, e1601185 (2016).
- Jeong, J.-W. et al. Materials and optimized designs for human–machine interfaces via epidermal electronics. *Adv. Mater.* **25**, 6839–6846 (2013).
- Lim, S. et al. Transparent and stretchable interactive human machine interface based on patterned graphene heterostructures. *Adv. Funct. Mater.* **25**, 375–383 (2015).
- Rogers, J. A., Someya, T. & Huang, Y. Materials and mechanics for stretchable electronics. *Science* **327**, 1603–1607 (2010).
- Choi, S., Lee, H., Ghaffari, R., Hyeon, T. & Kim, D. H. Recent advances in flexible and stretchable bio-electronic devices integrated with nanomaterials. *Adv. Mater.* **28**, 4203–4218 (2016).
- Xu, S. et al. Soft microfluidic assemblies of sensors, circuits, and radios for the skin. *Science* **344**, 70–74 (2014).
- Zhang, Y. et al. A hierarchical computational model for stretchable interconnects with fractal-inspired designs. *J. Mech. Phys. Solids* **72**, 115–130 (2014).
- Gonzalez, M. et al. Design of metal interconnects for stretchable electronic circuits. *Microelectron. Reliab.* **48**, 825–832 (2008).
- Fan, Z. et al. A finite deformation model of planar serpentine interconnects for stretchable electronics. *Int. J. Solids Struct.* **91**, 46–54 (2016).
- Ma, Y. et al. Soft elastomers with ionic liquid-filled cavities as strain isolating substrates for wearable electronics. *Small* **13**, 1602954 (2017).
- Li, J. et al. Tough adhesives for diverse wet surfaces. *Science* **357**, 378–381 (2017).
- Itzkan, I. et al. The thermoelastic basis of short pulsed laser ablation of biological tissue. *Proc. Natl Acad. Sci. USA* **92**, 1960–1964 (1995).
- Haynes, W. M. (ed.) *CRC Handbook of Physics and Chemistry* (CRC Press, Boca Raton, 2014).
- Gattass, R. R. & Mazur, E. Femtosecond laser micromachining in transparent materials. *Nat. Photon.* **2**, 219–225 (2008).
- Kim, T. N., Campbell, K., Groisman, A., Kleinfeld, D. & Schaffer, C. B. Femtosecond laser-drilled capillary integrated into a microfluidic device. *Appl. Phys. Lett.* **86**, 201106 (2005).
- Lee, T.-I., Kim, M. S. & Kim, T.-S. Contact-free thermal expansion measurement of very soft elastomers using digital image correlation. *Polym. Test.* **51**, 181–189 (2016).
- Xu, S. et al. Stretchable batteries with self-similar serpentine interconnects and integrated wireless recharging systems. *Nat. Commun.* **4**, 1543 (2013).
- Byun, J. et al. A single droplet-printed double-side universal soft electronic platform for highly integrated stretchable hybrid electronics. *Adv. Funct. Mater.* **27**, 1701912, (2017).
- Pfurtscheller, G. Event-related synchronization (ERS): an electrophysiological correlate of cortical areas at rest. *Electroencephalogr. Clin. Neurophysiol.* **83**, 62–69 (1992).
- Garcia-Rill, E. et al. The 10 Hz frequency: A fulcrum for transitional brain states. *Transl. Brain Rhythmicity* **1**, 7–13 (2016).
- Ramos, J., Wang, A., Ubellacker, W., Mayo, J. & Kim, S. A balance feedback interface for whole-body teleoperation of a humanoid robot and implementation in the HERMES system. *2015 IEEE-RAS 15th Int. Conf. Humanoid Robots (Humanoids)* <https://doi.org/10.1109/HUMANOID.2015.7363460> (2015).
- Ma, J., Zhang, Y., Cichocki, A. & Matsuno, F. A novel EOG/EEG hybrid human–machine interface adopting eye movements and ERPs: application to robot control. *IEEE T. Bio-med. Eng.* **62**, 876–889 (2015).
- Brosteaux, D., Axisa, F., Gonzalez, M. & Vanfleteren, J. Design and fabrication of elastic interconnections for stretchable electronic circuits. *IEEE Electron Device Lett.* **28**, 552–554 (2007).
- Yang, S., Ng, E. & Lu, N. Indium tin oxide (ITO) serpentine ribbons on soft substrates stretched beyond 100%. *Extreme Mech. Lett.* **2**, 37–45 (2015).
- Lee, C. H. et al. Soft core/shell packages for stretchable electronics. *Adv. Funct. Mater.* **25**, 3698–3704 (2015).
- Lee, T. et al. Fabrication of flexible, transparent and conductive films from single-walled carbon nanotubes with high aspect ratio using poly((furfuryl methacrylate)-co-(2-(dimethylamino)ethyl methacrylate)) as a new polymeric dispersant. *Nanoscale* **7**, 6745–6753 (2015).

Acknowledgements

The project described was partially supported by the UC San Diego Center for Wearable Sensors, Center for Healthy Aging, Contextual Robotics Institute, and the National Institutes of Health Grant UL1TR001442 of CTSA funding. The content is solely the responsibility of the authors and does not necessarily represent the official views of the NIH. We thank R. L. Sah's group for assistance with the XCT measurements, M. Tolley for discussions on robot control, Z. Zhang for his contribution on data analysis, M. Li for discussions on Bluetooth, M. Makihata for discussions on the antenna test and S. Xiang for her constructive feedback on manuscript preparation.

Author Contributions

Z.H. and S.X. designed the experiments. Z.H., Y.H. and Y.Li carried out experiments. All authors contributed to analysing the data. Z.H. and S.X. wrote the paper, on which all authors provided valuable feedback.

Competing interests

The authors declare no competing interests.

Additional information

Supplementary information is available for this paper at <https://doi.org/10.1038/s41928-018-0116-y>.

Reprints and permissions information is available at www.nature.com/reprints.

Correspondence and requests for materials should be addressed to S.X.

Publisher's note: Springer Nature remains neutral with regard to jurisdictional claims in published maps and institutional affiliations.

Reporting Summary

Nature Research wishes to improve the reproducibility of the work that we publish. This form provides structure for consistency and transparency in reporting. For further information on Nature Research policies, see [Authors & Referees](#) and the [Editorial Policy Checklist](#).

Statistical parameters

When statistical analyses are reported, confirm that the following items are present in the relevant location (e.g. figure legend, table legend, main text, or Methods section).

n/a Confirmed

- ☐ ☒ The exact sample size (n) for each experimental group/condition, given as a discrete number and unit of measurement
- ☐ ☒ An indication of whether measurements were taken from distinct samples or whether the same sample was measured repeatedly
- ☒ ☐ The statistical test(s) used AND whether they are one- or two-sided
Only common tests should be described solely by name; describe more complex techniques in the Methods section.
- ☒ ☐ A description of all covariates tested
- ☒ ☐ A description of any assumptions or corrections, such as tests of normality and adjustment for multiple comparisons
- ☒ ☐ A full description of the statistics including central tendency (e.g. means) or other basic estimates (e.g. regression coefficient) AND variation (e.g. standard deviation) or associated estimates of uncertainty (e.g. confidence intervals)
- ☒ ☐ For null hypothesis testing, the test statistic (e.g. F , t , r) with confidence intervals, effect sizes, degrees of freedom and P value noted
Give P values as exact values whenever suitable.
- ☒ ☐ For Bayesian analysis, information on the choice of priors and Markov chain Monte Carlo settings
- ☐ ☒ For hierarchical and complex designs, identification of the appropriate level for tests and full reporting of outcomes
- ☒ ☐ Estimates of effect sizes (e.g. Cohen's d , Pearson's r), indicating how they were calculated
- ☒ ☐ Clearly defined error bars
State explicitly what error bars represent (e.g. SD, SE, CI)

Our web collection on [statistics for biologists](#) may be useful.

Software and code

Policy information about [availability of computer code](#)

Data collection

Bluetooth chips were programmed by Keil μ Vision V5.14 to configure the resolution of ADC and packaging logics. The software for the robot arm control was built on FlowBotics Studio (RobotShop Inc.). LabVIEW 2015 was used for Bluetooth signal acquisition.

Data analysis

Origin 2017.

For manuscripts utilizing custom algorithms or software that are central to the research but not yet described in published literature, software must be made available to editors/reviewers upon request. We strongly encourage code deposition in a community repository (e.g. GitHub). See the Nature Research [guidelines for submitting code & software](#) for further information.

Data

Policy information about [availability of data](#)

All manuscripts must include a [data availability statement](#). This statement should provide the following information, where applicable:

- Accession codes, unique identifiers, or web links for publicly available datasets
- A list of figures that have associated raw data
- A description of any restrictions on data availability

The data that support the plots within this paper and other findings of this study are available from the corresponding authors upon reasonable request.

Field-specific reporting

Please select the best fit for your research. If you are not sure, read the appropriate sections before making your selection.

☒ Life sciences ☐ Behavioural & social sciences ☐ Ecological, evolutionary & environmental sciences

For a reference copy of the document with all sections, see [nature.com/authors/policies/ReportingSummary-flat.pdf](https://www.nature.com/authors/policies/ReportingSummary-flat.pdf)

Life sciences study design

All studies must disclose on these points even when the disclosure is negative.

Sample size	No statistical methods used in this case; A healthy male of age 22 without cardiac anomaly was chosen to collect all the data. All of the vital signs involved can be tested from one single healthy person, and characteristics of these parameters on healthy people show a small deviation.
Data exclusions	No data was excluded from analysis.
Replication	All of the vital signal measurements were taken on the same subject for multiple times (with the stable physiological condition) within 3 months. Each type of the signal was taken on the same sampling position, and continuous measured for the same duration of time. Each type of data was sampled for multiple times (more than 5 times) and compared during the measurements. From the measured results, the data showed high similarity within the same testing group, and the reproducibility of all kinds of measurements were good in this case.
Randomization	None. One device type was tested in same participant. Randomization is not relevant to the research.
Blinding	None. The blinding process won't influence sampling result.

Reporting for specific materials, systems and methods

Materials & experimental systems

n/a	Involved in the study
<input checked="" type="checkbox"/>	<input type="checkbox"/> Unique biological materials
<input checked="" type="checkbox"/>	<input type="checkbox"/> Antibodies
<input checked="" type="checkbox"/>	<input type="checkbox"/> Eukaryotic cell lines
<input checked="" type="checkbox"/>	<input type="checkbox"/> Palaeontology
<input checked="" type="checkbox"/>	<input type="checkbox"/> Animals and other organisms
<input type="checkbox"/>	<input checked="" type="checkbox"/> Human research participants

Methods

n/a	Involved in the study
<input checked="" type="checkbox"/>	<input type="checkbox"/> ChIP-seq
<input checked="" type="checkbox"/>	<input type="checkbox"/> Flow cytometry
<input checked="" type="checkbox"/>	<input type="checkbox"/> MRI-based neuroimaging

Human research participants

Policy information about [studies involving human research participants](#)

Population characteristics	The human participant is a healthy male of age 22, with no cardiac anomaly.
Recruitment	Volunteered; No potential bias in this case.

In the format provided by the authors and unedited.

Three-dimensional integrated stretchable electronics

Zhenlong Huang^{1,2,9}, Yifei Hao^{1,3,9}, Yang Li^{1,9}, Hongjie Hu⁴, Chonghe Wang¹, Akihiro Nomoto¹, Taisong Pan², Yue Gu⁴, Yimu Chen¹, Tianjiao Zhang⁴, Weixin Li^{1,3}, Yusheng Lei¹, NamHeon Kim¹, Chunfeng Wang^{1,5}, Lin Zhang¹, Jeremy W. Ward⁶, Ayden Maralani⁷, Xiaoshi Li¹, Michael F. Durstock⁶, Albert Pisano^{1,4,7}, Yuan Lin² and Sheng Xu^{1,4,7,8*}

¹Department of Nanoengineering, University of California San Diego, La Jolla, CA, USA. ²State Key Laboratory of Electronic Thin films and Integrated Devices, University of Electronic Science and Technology of China, Chengdu, China. ³Biomedical Engineering, School of Precision Instrument and Opto-electronics Engineering, Tianjin University, Tianjin, China. ⁴Materials Science and Engineering Program, University of California San Diego, La Jolla, CA, USA. ⁵The Key Laboratory of Materials Processing and Mold of Ministry of Education, School of Materials Science and Engineering, School of Physics & Engineering, Zhengzhou University, Zhengzhou, China. ⁶Soft Matter Materials Branch, Materials and Manufacturing Directorate, The Air Force Research Laboratory, Wright-Patterson Air Force Base, OH, USA. ⁷Department of Electrical and Computer Engineering, University of California San Diego, La Jolla, CA, USA. ⁸Department of Bioengineering, University of California San Diego, La Jolla, CA, USA. ⁹These authors contributed equally: Zhenlong Huang, Yifei Hao, Yang Li. *e-mail: shengxu@ucsd.edu

This file includes Supplementary Notes 1-9 and Supplementary Figures 1-63

Supplementary Note 1. The mechanical coupling between different layers in the 3D integrated device and potential solutions to mitigate the constraints

The chips/interconnects can add mechanical loading to the local elastomer matrix and result in strain non-uniformity in the vicinity areas. Compared with a single layer, such constraints from a multilayered device will be more prominent and thus influence the overall stretchability of the device, as shown in Fig. 1c and Supplementary Fig. 6. There are two potential solutions to solve this problem.

Solution 1: One approach is to reduce the dimensions of the rigid chips, by using the unpackaged bare dies. As shown in Supplementary Fig. 7, the XCT images of a typical functional chip (e.g., the amplifier) highlight the dimensions of the packaged chip, polished chip, and bare die. It can be seen that the width of the chip decreases from 6.2 mm (packed chip) to 2.3 mm (bare die) and the thickness decrease from 2.3 mm (packed chip) to 0.3 mm (bare die). The strain at the interface between the rigid and soft components decreases dramatically with reducing the rigid component size. Therefore, the constraints from the rigid components can be effectively reduced by moving from bulky packaged chips to small bare dies. In addition, bare dies can also improve the areal density of functional chips.

Solution 2: A strain isolation layer can be added between the adjacent layers. The strain isolation layer is usually an elastomer with ultra-low Young modulus or even liquid¹, which can effectively decouple the rigid and soft components. To study the strain isolation effect, an elastomer/solution layer with different Young modulus was added between two adjacent layers, as illustrated in Supplementary Fig. 8a. To control the thickness of the device, the strain isolation layer was limited to a thickness $D = 0.15$ mm with $D/C = 0.06$. And the interconnect length/chip width ratio L/C was controlled to be 1.06. The interconnect geometry and strain distribution were calculated by FEA under 20% stretching, as shown in the insets of Supplementary Fig. 8b-8e. With the Young modulus of the strain isolation layer decreased from 1000 kPa (PDMS) to 0.06 kPa (solution), the interconnect geometry becomes more uniform (Supplementary Fig. 8b-8e) and the maximum principal strain of the interconnect becomes smaller (Supplementary Fig. 8f). The Silbione elastomer with an ultra-low Young modulus of 3 kPa can achieve similar results as the solution based strain isolation layer. From these studies, it can be seen that low Young modulus (less than 3 kPa) elastomer/solution can be used as an ideal strain isolation mechanism to decrease the constraint between layers.

Supplementary Note 2. Adhesion between the Ecoflex in different layers

To assess the adhesion between the Ecoflex in different layers, the debonding energy was measured based on the strain-stress curves of three samples: a single substrate, a bilayer sample, and a debonding sample, as shown by the schematics in Supplementary Fig. 9.

A: Sample fabrication

(1) Single substrate

The process began with a coating of polymethyl methacrylate (PMMA) (5 μm thick) on two pieces of glass slides. Then the PMMA/glass slides were cured on a hotplate at 180 °C for 1 min. Two spacers with 1.00 mm thickness were placed between the two glass slides, and Ecoflex 0030 (1:1) was poured into the cavity between the two glass slides. The cured Ecoflex sample was then peeled from the glass slides and cut into several slices (length: 63.5 mm; width: 10.9 mm).

(2) Bilayer sample

The bilayer sample consisted of the single substrate and a second layer of Ecoflex. The single substrate was prepared first. Then two spacers with 2.00 mm thickness were placed on the top of the single substrate, and one piece of glass slide coated with cured PMMA was laminated on the spacers. Ecoflex-0030 (1:1) was poured and cured in the cavity between the single substrate and the glass slide. Removing the glass slide completed the fabrication process. Finally, the sample was cut into several slices with a length of 69.5 mm and a width of 11.2 mm.

(3) Debonding sample

The debonding sample consisted of two layers of Ecoflex, with a small region left unbonded in between. The fabrication approach was same as the bilayer sample, except that there was an unbonded region on one side of the bilayer interface. The unbonded region had an area of 10.92 mm \times 3 mm and was created by inserting a thin plastic film before curing the second layer of Ecoflex. After the second layer of Ecoflex was cured, the plastic film was extracted out of the bilayer interface.

B: Testing method and principle

Before doing the tensile testing, each sample was glued and fixed on acrylic boards. Then, the samples were clamped and stretched by the tensile testing machine (Instron 5965). The testing rate was 1.25% per second, and the load cell was 1 kN. When measuring the debonding sample, a single lens reflex camera (Canon EOS70D) was used to take a video and record the entire process so that the time of delamination between two layers can be captured. The stress-strain curves of those three samples were obtained.

Based on the strain-stress curves of single substrate and bilayer sample, the elastic energy stored in the substrate and bilayer sample could be calculated by equations²:

$$U_s(\lambda) = \int_1^\lambda P_s(\lambda) d\lambda \quad (1)$$

$$U_b(\lambda) = \int_1^\lambda P_b(\lambda) d\lambda \quad (2)$$

where U_s , U_b , P , and λ are the elastic energy of the single substrate, the elastic energy of the bilayer sample, force, and strain, respectively. When doing the debonding test, the sample was subjected to a constant force P at a steady state. The strain of the detached substrate and bonded bilayer were assumed to be λ' and λ'' , respectively, at the point of delamination between the two layers, which could be obtained by multiplying the testing rate and the time of delamination. The elastic energy of the single substrate and bilayer sample were $U_s(\lambda')$ and $U_b(\lambda'')$. Therefore, the debonding energy Γ can be calculated by the equation:

$$\Gamma = U_b(\lambda'') - U_s(\lambda') + P * (\lambda' - \lambda'') \quad (3)$$

For our samples, when the strain reached 400% in the debonding test, there was no deviation of strain-stress curve³, which meant the delamination did not propagate. The sudden drops in the strain-stress curves in Supplementary Fig. 10 were the failure points when samples were broken due to the limited stretchability rather than the debonding. If the sudden drop at around 400% were to be used as the delamination point, the calculated debonding energy was around 424.26 J*m⁻². As the delamination point appeared beyond the 400% strain, the real debonding energy between the Ecoflex layers should be larger than 424.26 J*m⁻². For the wearable electronic device, 400% covers all practical use cases. Therefore, the Ecoflex layers won't delaminate in the multilayered device.

Supplementary Note 3. Bonding strength test between the chip and the interconnect pads

The most vulnerable part of the integrated electronic system is the contacts between solder pads in soft interconnection and rigid electronic chips due to their large mechanical mismatch. In our study, two critical parameters are the flux cleaning and the heating temperature, which are controlled to achieve high-quality bonding. And the details are shown below.

We used tin-based solder paste to bond the chip pins and copper interconnects. Specifically, after transfer printed on the elastomeric substrate, the copper interconnects were cleaned by Flux (WOR331928, Worthington, Inc.) to remove the surface oxides on the copper. Then, the Sn₄₂Bi_{57.6}Ag_{0.4} alloy paste (Chip Quick Inc. SMDLTLFP-ND, with a low melting point of 138 °C) was screen-printed onto the copper pads. Polished chips with reduced thickness and footprint were well aligned on the copper pads, reflowed by baking on a hotplate at ~150 °C for five minutes, and then cooled down to room temperature to form solid alloys between the tin-based solder and interconnect copper pad. The as-formed tin-copper alloy between the chip pins and the solder, and the solder and the interconnects would yield a strong and robust bonding.

In this process, the flux would help remove the copper surface oxide, which would otherwise prevent the formation of solid alloys at the interface and thus lead to large contact resistance and weak bonding. Temperature had to be controlled carefully to melt the Sn₄₂Bi_{57.6}Ag_{0.4} paste. If it was too high, it would melt the solidified alloys in previous layers. If it was too low, the solder paste would not melt thoroughly. Three groups of experiments were carried out to illustrate the effect of these two parameters, as shown in Supplementary Fig. 28.

Group 1: High heating temperature (150 °C) with flux treatment for copper interconnect (Supplementary Fig. 28a).

Group 2: High heating temperature (150 °C) without flux treatment for copper interconnect (Supplementary Fig. 28b).

Group 3: Low heating temperature (140 °C) with flux treatment for copper interconnect (Supplementary Fig. 28c).

For the group 1 (Supplementary Fig. 28a), the solder paste had good wetting behavior and formed a good contact angle between the solder and copper contact pad. For the group 2 (Supplementary Fig. 28b), the contact angle of the solder on untreated copper pads became much larger. The tin solder balls beaded-up, which forced the resistor to move away from the copper pads by surface tension. For the group 3 (Supplementary Fig. 28c), the reflow temperature was a little higher than the solder paste melting point (138 °C). However, the low thermal conductivity of the silicone led to incomplete solder paste melting around the chip, which might most likely cause open circuit and weak bonding.

To characterize the robustness of the bonding between the rigid chips and interconnect, the sample bonded with high heating temperature and flux treatment was used to test its stretchability, as shown in Supplementary Fig. 29. During the tensile test, the resistance of the device was continuously monitored. When the strain was 0%, the total resistance was 4.67 kΩ (Supplementary Fig. 29a). The results shown in Supplementary Fig. 29b indicated that the device had a stretchability of more than 120%. During the entire stretching process, the interface bonding between the rigid chip and interconnect pads was very stable and did not show any evidence of delamination. The serpentine interconnect was broken before the bonding between the rigid chip and interconnect pads failed, when it was stretched to 138% (Supplementary Fig. 29c), clearly proving the robustness of the bonding between the chips and the interconnect pads.

Supplementary Note 4. Comparison of different approaches for VIAs

The VIA formed by laser cutting has much higher complexity, better robustness, and lower resistance compared with other approaches reported in the literature. We discuss three typical VIA formation methods in the following.

The lithography-based method for copper VIAs used oxygen plasma etching (300 mT, 20 sccm O₂, 200 W for 10 min) to form a crater in the polyimide (PI) layer through a mask defined by high-resolution photolithography. Then, a thin layer of copper (600 nm) covering the internal surface of the crater was deposited through electron beam evaporation. For this method, **first**, the “VIA” presented was not the VIA in the conventional sense which should connect *different* layers of circuits for the electrical communication. The “VIA” in that work was used to connect the copper wires in the *same* layer. The insulator between the two connected copper wires was PI, which was only flexible but not stretchable and could not be used as the matrix material for the entire stretchable system. **Second**, the PI layer was very thin (1.2 μm), because oxygen plasma had limited etching capabilities. This approach could not be used to form high-aspect

ratio VIAs that were needed to connect non-adjacent circuit layers. **Third**, the electron beam evaporation deposited copper thin film could barely and weakly bond to the surface of the VIA sidewalls. When bent or twisted, the VIA shape would be changed and the copper film on the sidewalls might crack, which meant the VIA fabricated with this method was not stable.

The printing-based method exploited the mixture of Ni microparticles/PDMS(5:1)/silicone resin (OE6630, Dow Corning) with a mixing weight ratio of 5:2:3 as the VIA. For this kind of metal/polymer composites, **first**, the resistance was very large. As the authors described in the article “the range of initial resistance of core-shell VIAs was around 10-20 Ω ”, in comparison to the resistance of 0.068 ohms to 0.070 ohms in our case. With such a high resistance, the printed VIAs had little value for electrical communication in real circuits. The high resistance of interconnects will appreciably change electrical parameters and performance of the designed circuit. For amplifier chips (e.g., AD627), the gain was highly based on the external resistance input. For resonators, the resistance was critical for its quality factor. Besides, the high parasitic resistance would largely increase the power dissipation of the entire circuit. **Second**, the composite VIA formed by this method was not stable upon strain, as presented in Figure 4e of the paper, “the resistance versus applied tensile strain profile suggests that the resistance slightly increased in the low strain regime ($\epsilon_{\text{appl}} < 20\%$), started to decrease, and was finally sustained in the high strain regime ($\epsilon_{\text{appl}} < 100\%$)”. The VIA resistance in the paper increased up to around 1.7 times of the initial resistance when 20% strain was applied. The unstable electrical properties of the VIAs would certainly undermine the performance and mechanical reliability of the stretchable system.

Our laser ablation and solder paste injection methods formed the VIAs through thick (100 μm) and stretchable silicone. The as-formed VIAs were used to connect circuits in different layers, adjacent and non-adjacent. Besides, the VIA material was $\text{Sn}_{42}\text{Bi}_{57.6}\text{Ag}_{0.4}$ metal alloy, which had very high conductivity. Furthermore, when heated, a layer of Cu-Sn alloy would form between the VIA and the copper interconnects (for both top and bottom copper wires), which built strong bonding between the VIAs and the interconnects in different layers and made the VIAs very stable.

To prove the high performance of the VIAs formed by the laser ablation and solder paste injection method, a VIA was bonded with two interconnects on the top and bottom layers, respectively, as shown in the schematics of Supplementary Fig. 1e. First, the I-V curves of the VIA under 0% and 100% strains were measured (Supplementary Fig. 30a). The straight line meant it was an ohmic contact between the VIA and copper interconnects. The overlapped two lines indicated the resistance didn't change noticeably with the strain from 0% to 100%. To check the VIA performance under high frequency, impedance spectroscopy data of the VIA was collected (Supplementary Fig. 30b). The impedance increased with the frequency, because of the skin effect for r.f. transmission wires⁴ and increased inductive reactance value at higher frequencies (inductive reactance $X_L = 2\pi fL$, where f is the frequency and L is the wire inductance). The high frequency electric current flowed mainly at the "skin"--a surface layer of the conductor. The conductive skin depth was proportional to the square root of the frequency⁴. As such, with increasing frequency, the effective cross-sectional area of the conductor decreased and hence impedance increased. For our VIA, the impedance slightly increased when the

frequency was higher than 1 MHz, and dramatically increased when the frequency was above 50 MHz.

Supplementary Note 5. CNT-Silbione composite electrode biocompatibility

Carbon nanotubes (CNTs) have been used in a variety of biological and biomedical studies serving as biosensors, drug and vaccine delivery vehicles, and biomaterials⁵. With decades of research on bio-applications of the CNT, its toxicity and biocompatibility have been well studied on both cellular and tissue/organ levels. Researchers have demonstrated that on the cellular level, the purified CNT without chemical modification possessed no evidence of cytotoxicity^{6,7}. On the tissue/organ level, the CNT performed no or very weak eye irritation and skin sensitization⁸. Results from a study based on human skin equivalent model and a Draize skin irritation test also revealed that the CNT did not induce any acute cutaneous irritation⁷.

The CNT could be used as nano-fillers in existing polymeric materials to create electrically conductive nanocomposites. Devices incorporating CNT-polymer based electrodes have been reported⁹⁻¹¹. The biocompatibility of CNT-polymer composite electrodes has also been verified. Jung *et al.* reported a CNT/PDMS composite flexible dry electrodes for ECG sensing¹². They cultured skin fibroblast cells on the surface of the electrodes for seven days and the cell viability exceeded 95%, indicating that the CNT/PDMS composite did not affect the cell growth. Ten subjects continuously wore the electrodes on their forearms to reveal the skin compatibility. No irritation/side effects were observed over the seven-day continuous wearing.

Finally, reported evidence of the biological risk of CNT-related materials were mainly focused on lung toxicity, including lung inflammation and granuloma formation¹³⁻¹⁶. Significant evidence of pulmonary toxicity of unrefined CNTs was observed¹⁵. However, in our case, CNTs strongly adhered to the silbione matrix, and the application was for electrophysiological potential sensing on the skin surface, resulting in no risk of inhalation.

Supplementary Note 6. The local heating behavior of the 3D integrated stretchable system

To assess the local heating behavior of the system, a thermographic camera (Therm-App® TH, 384*288 pixels resolution, Sensitivity < 70 mK) was used to capture thermal images of a working device.

First, the system was placed on the bench at room temperature (24 °C). After the system was powered on, thermal images of the system were recorded continuously, as shown in Supplementary Fig. 44. It could be seen that the temperature of the device increased as long as the device was powered, and then tended to be stable in around 10 mins. The highest temperature, automatically identified by the thermal camera, was located on the gyro chip, which had the biggest power dissipation as shown in Supplementary Fig. 42. The temperature of the gyro chip increased 2.7 °C in the first 10 mins and was stable at 27.2 °C. And the lowest temperature, automatically identified by the thermal camera, was located on the corner of the device, where no chip was located. Detailed information for the temperature variation is shown

in Supplementary Fig. 44b. When the system was shut down, the device temperature recovered to the room temperature in ~10 mins.

Second, to evaluate the real working environment, the system was attached to the human skin to assess the temperature distribution of the system in operation, as shown in Supplementary Fig. 45. The highest temperature of the system increased to 33.6 °C in 5 mins, only 2.3 °C higher than the resting state (31.3 °C), which was acceptable for the human skin.

As shown in Supplementary Figs. 44 and 45, the temperature variation is within 2.7 °C working at room temperature (24 °C) and within 2.3 °C working on the human skin. After the device was turned off, the temperature dropped very fast. Thus, the natural passive heat dissipation was sufficient to manage the device temperature and thus no further specific measures were needed in this case.

Supplementary Note 7. Quantitative electrical measurements of the soft system under strain

This includes two parts: quantitative evaluation of the interconnect under strain, and quantitative electrical measurements of the multilayered system under strain.

Part 1: Quantitative evaluation of the interconnect under strain

A typical serpentine interconnect used in the multilayered system was designed and fabricated to quantify the electrical properties under strain. The I-V curve of the copper interconnect (width: 0.15 mm; pad-to-pad length: 5.68 mm; thickness: 0.02 mm) was tested under 0% and 100% strains, as shown in Supplementary Fig. 52. From the slope of the straight line, the resistance of the copper interconnect could be calculated to be 0.34 Ω (0%) and 0.35 Ω (100%). Furthermore, with the strain from 0% to 100% (increment 10%), the interconnect resistance was measured, as shown in Supplementary Fig. 52b. The resistance varied in a narrow band from 0.33 Ω to 0.36 Ω , which indicated stable electrical properties of the interconnects.

To evaluate the serpentine interconnect performance at high frequencies, the interconnect impedance spectroscopy under 0% and 100% strain states was measured from 6 KHz to 100 MHz, as shown in Supplementary Fig. 53. Two conclusions could be drawn from the data. First, the interconnect impedance increased with increasing frequency, especially when the frequency was higher than 10 MHz due to the skin effect and increased inductive reactance at higher frequencies. Second, with interconnect strain increased from 0% to 100%, the impedance increased 7% when the frequency was lower than 1 MHz and up to around 34% when the frequency was larger than 10 MHz, which owned to the larger wire inductance of the deformed interconnects.

Furthermore, as the ceramic antenna chip was connected with the Bluetooth chip through a 5.75 mm long serpentine (width: 0.15 mm; thickness: 0.02 mm), the S_{11} parameter of the antenna connected with the same length serpentine interconnect (fully encapsulation with Ecoflex as in the multilayered soft system) was tested under strains from 0% to 80%, as shown in

Supplementary Fig. 54. It could be seen that the resonance frequency shifted slightly from 2.475 GHz (0% strain) to 2.461 GHz (80% strain) due to the serpentine interconnect deformation¹⁷, and the corresponding S_{11} amplitude decreased from -16.79 dB to -46.59 dB, which meant less reflection loss when the interconnect was deformed from serpentine geometry (0% strain) to buckled geometry (80% strain).

Part 2: Quantitative electrical measurements of the multilayered system under strain

First, as discussed in part 1, the serpentine was very stable at low frequencies and was more sensitive to the strain when the frequency was higher than 10 MHz. For the Bluetooth communication, we connected a 16 MHz oscillator to the Bluetooth chip and a 2.4 GHz antenna was used for the wireless communication, which meant the Bluetooth module might be the most vulnerable part in the design. The received-signal-strength-indicator (RSSI) of the Bluetooth signal from the multilayered system was measured under different strain levels, with the receiver at a distance of several meters. The collected results are shown in Supplementary Fig. 55. It could be seen that the RSSI varied randomly from -75 dBm to -90 dBm with strains from 0% to 44% of the entire system, which means the Bluetooth module worked well with strain values up to 44%, beyond which, the device was broken and no Bluetooth signal could be detected probably due to the interconnect failure.

Second, it is also very valuable to evaluate the accuracy and quality of the signals acquired by the sensors and processed by the chips under strain. As the four-layer stretchable system was fully packaged by the silicone elastomer. It was challenging to probe the signal quality at defined locations inside the packaged system. So, we redesigned the four-layer system with probing sites embedded, as shown in Supplementary Fig. 56. A few probing sites were added to corresponding interconnects and chip pads. These probing sites allowed us to record the signals after relevant steps, e.g., picked up by the sensor and processed by the pre-amplifier and filters.

In our study, we used the electrocardiogram channel as a representative example. We plotted the original ground truth signal from a functional generator, together with the signals after being picked up by the CNT/Silbione composite electrode, and processed by the amplifier and filters. The signals were compared when the full system was freestanding and under various levels of applied strain (Supplementary Fig. 57). Supplementary Fig. 57a shows the original signal, signals collected by the CNT/Silbione electrode, and signals magnified for 508 times and filtered by the chips under different levels of strain from 0% to 35% in the system. The zoom-in view of the original signal and sensor signal is shown in Supplementary Fig. 57b. Due to different magnitudes of the signals, we normalized them for a side-by-side comparison as shown in Supplementary Figs. 57c and d. The results show that the signals after being captured by the sensor and processed by the chips were very close to the original signal. Also, the different levels of strain applied to the system in this study had nearly no influence on the chip data processing and device performance.

Supplementary Note 8. Laser ablation as a viable tool for manufacturing stretchable electronic systems

In this study, we use the laser ablation to fabricate both the VIA and the interconnects.

For VIAs, it needs to ablate the silicone to generate craters with high aspect ratio. Yet, silicone elastomers are notoriously difficult to be etched due to their chemical inertness. With inorganic -Si-O-Si- backbones and hydrocarbon side chains, silicone elastomers cross the boundary between organic and inorganic materials: the inorganic backbone makes them highly resistant to reactive ion etching, and the organic side chains protect them from fluorine chemistry that is commonly used to break the Si-O bonds. So, for traditional etching methods, it can only generate silicone craters with low aspect ratio, which are not suitable for the VIAs in this case.

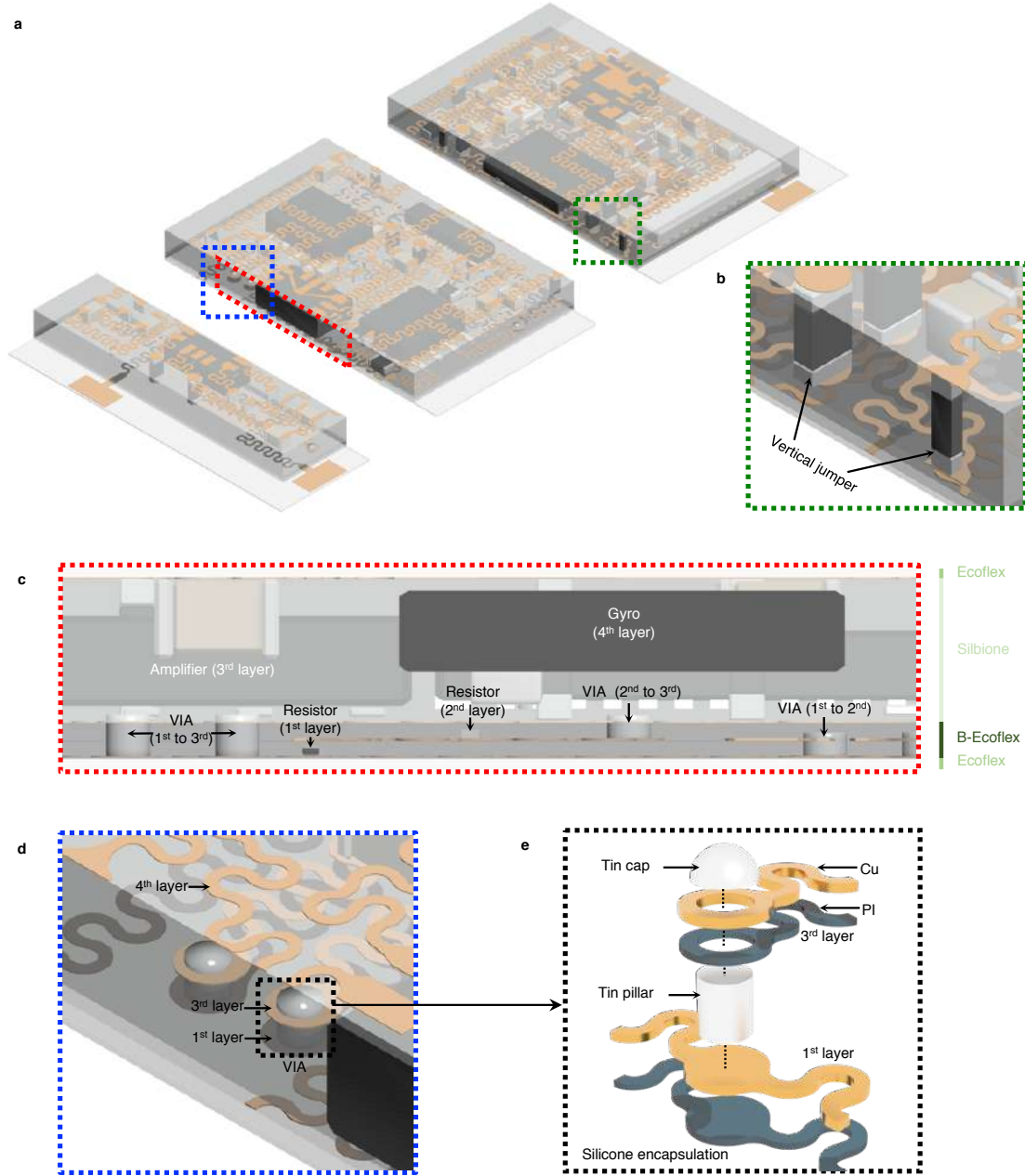
Laser ablation, a mass removal method by coupling photon energy to materials¹⁸⁻²¹, is uniquely suitable to process silicone elastomers. In comparison with lithography-based processes, it offers quick, precise, and scalable direct-write capabilities²². Due to the low absorption of silicone elastomers in the visible and IR ranges, we mixed dyes in the translucent elastomer to enhance the absorption and therefore lower the ablation threshold, which made it possible for nanosecond laser for the VIA formation.

For interconnects, compared with traditional photolithography based etching methods, the laser ablation is more time and cost efficient. Additionally, it is chemical-free.

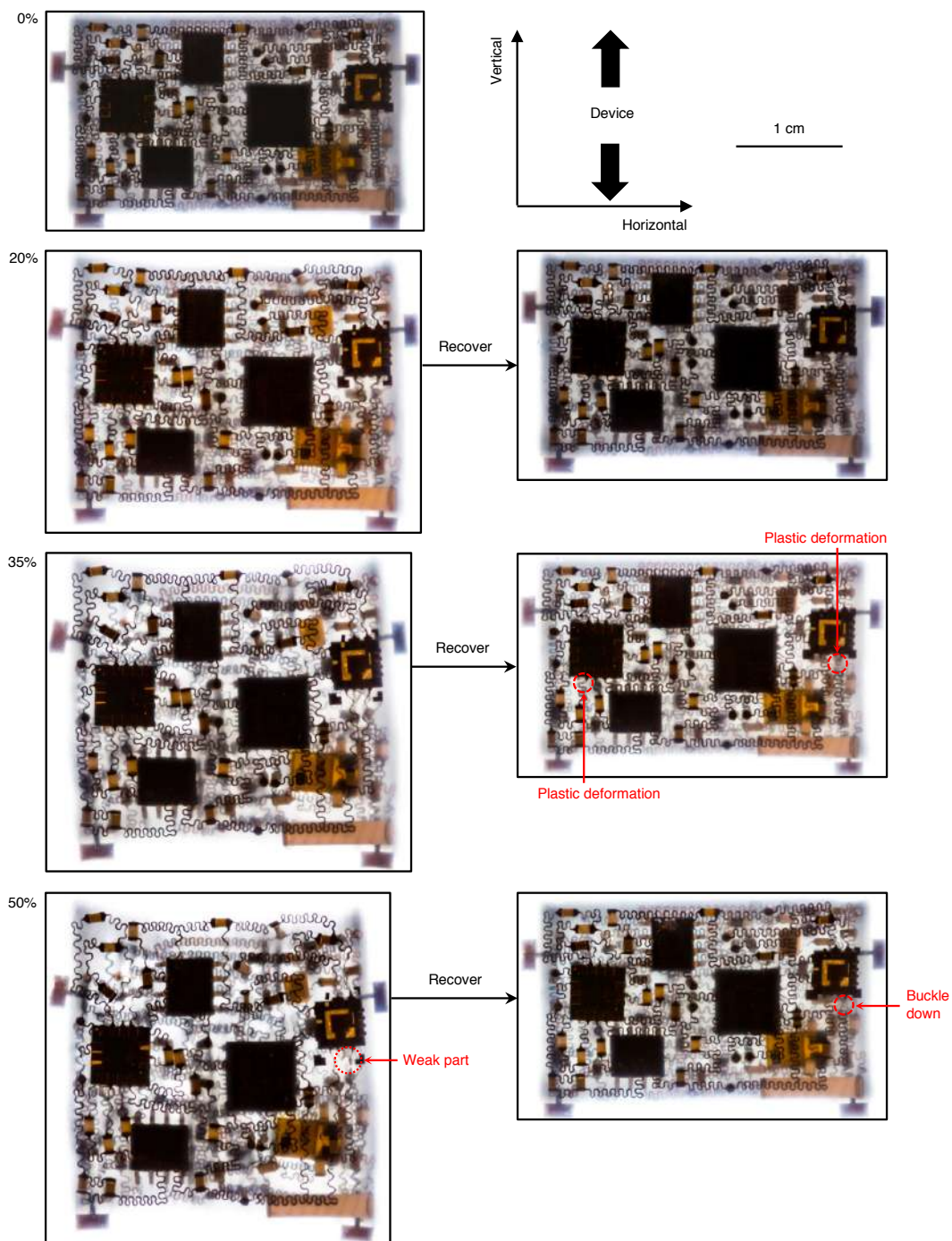
Yet, there are also some limitations of the laser ablation. For example, the heat generated from the laser could oxidize the copper interconnects. To solve this problem, the copper ablation might need to take place in an inert environment, e.g., in nitrogen or argon. Or after the laser processing, the flux solution might need to be applied to remove the surface oxide layer before the subsequent bonding steps.

Supplementary Note 9. The latency of the 3D integrated stretchable system

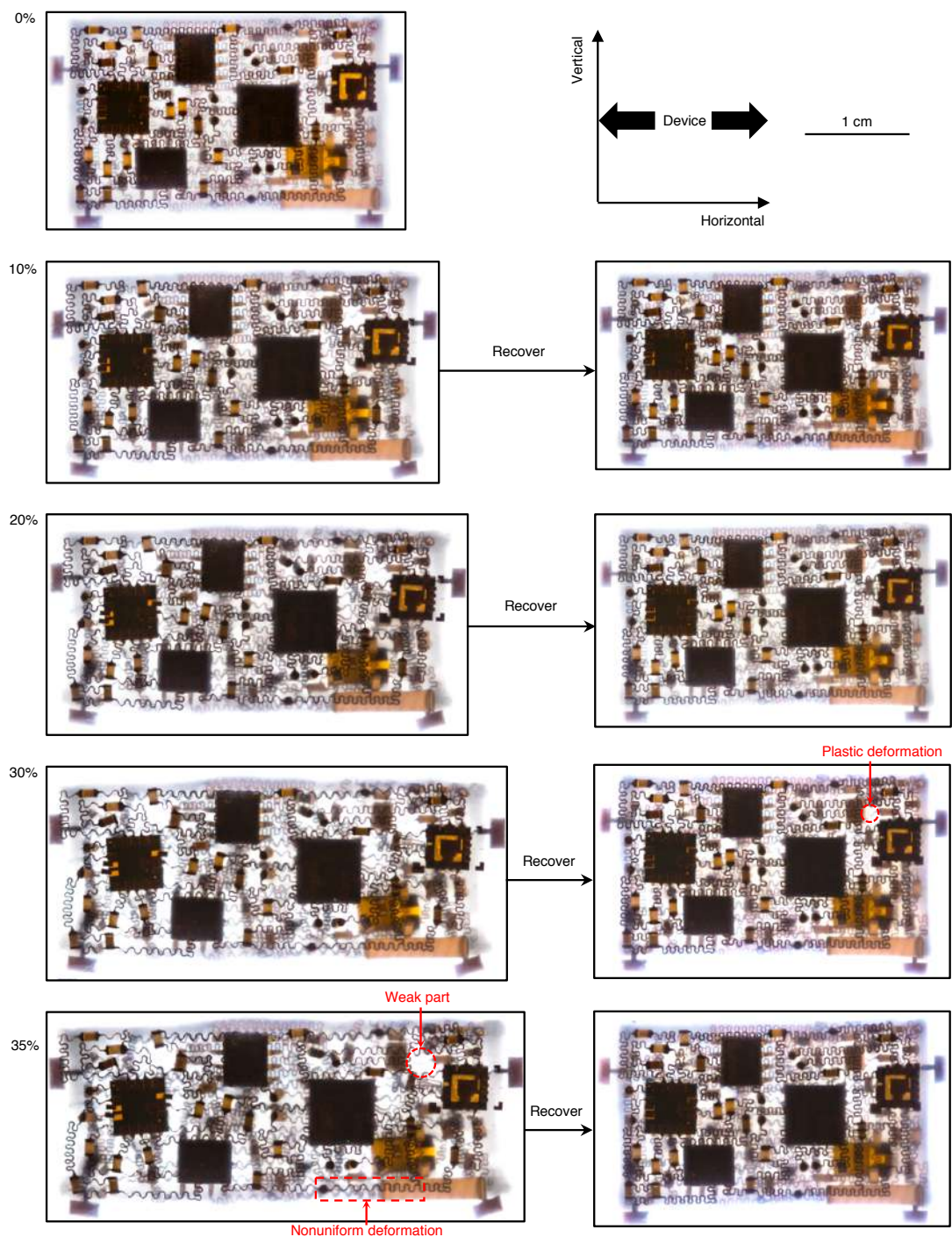
For the 3D integrated stretchable system, we used the commercial-off-the-shelf sensors, such as Accelerometer (ADXL335BCPZ), whose turn-on time was only 1 ms (Datasheet of ADXL335. *Analog Devices P3*, (2009-2010)). And for the wireless data communication, we used the standard Bluetooth protocol. According to the latency analysis of the Bluetooth network²³, it took 100 ms-200 ms to discover a device. Once connected, however, the communication time between two paired devices was less than 1 ms²³. Therefore, for our multilayered system, the total time delay including the sensing and wireless data transfer was controlled to be less than 2 ms.



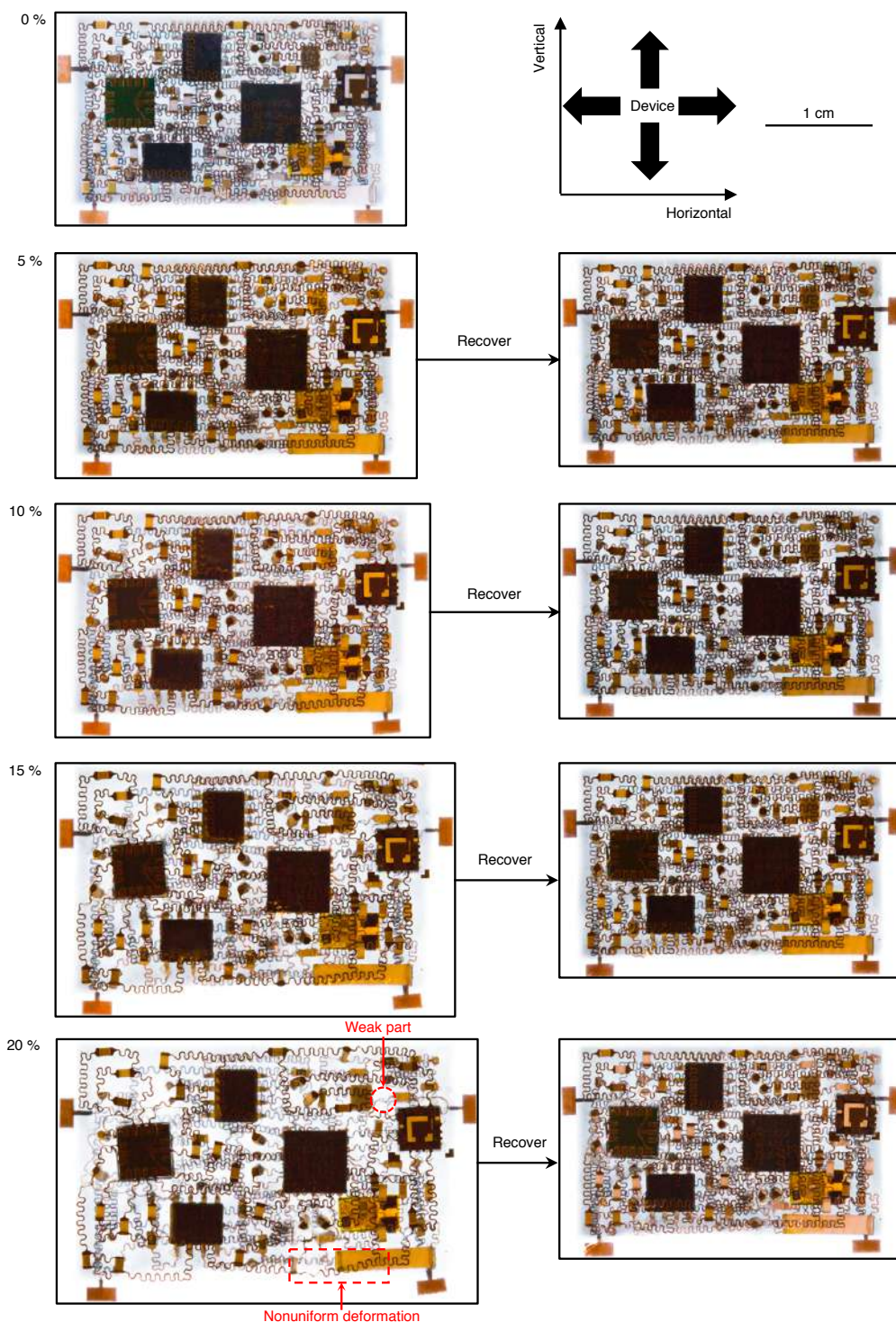
Supplementary Figure 1. Schematic illustration of the three-dimensional integrated stretchable system. **a**, Overview of a four-layer stretchable device with two cross-section cuts to highlight the design features. **b-d**, Zoomed-in views of the cuts. **b**, Vertical jumpers are used as the electrical connection between the 3rd layer and 4th layer, to accommodate some thick chips. The first three layers use tin based VIAs as the interlayer connection. **c**, The four-layer device has functional sensors and passive components in each layer with VIAs among these layers for interlayer electrical connections. The stretchable system is packed in core-shell structures, with Ecoflex as the shell and ultra-low Young's modulus Silbione as the core, to increase the stretchability of the overall system. B-Ecoflex indicated Ecoflex mixed with the black dye for laser ablation. **d-e**, The cross-section view and the exploded structure of a typical tin based VIA. The serpentine interconnect is composed of bilayers of Cu/PI. With screen-printing, the tin pillar and tin cap are fabricated to achieve solid electrical bonding.



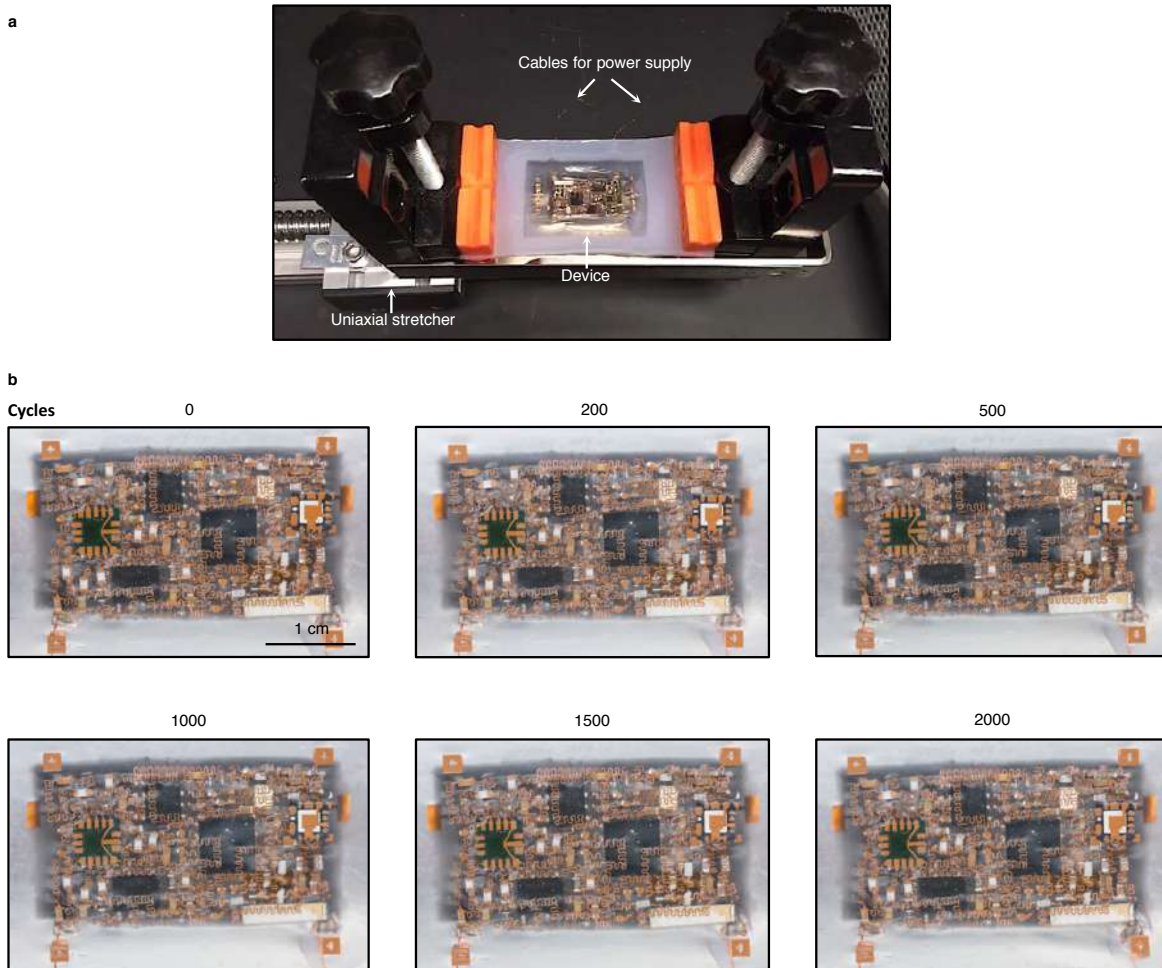
Supplementary Figure 2. Experimental studies of buckling deformations across the entire circuits under uniaxial stretching along the vertical direction. Failure strain in the vertical direction is $\sim 50\%$ with weak points at the interconnect between the accelerometer and capacitor. Plastic deformation begins at $\sim 35\%$ strain.



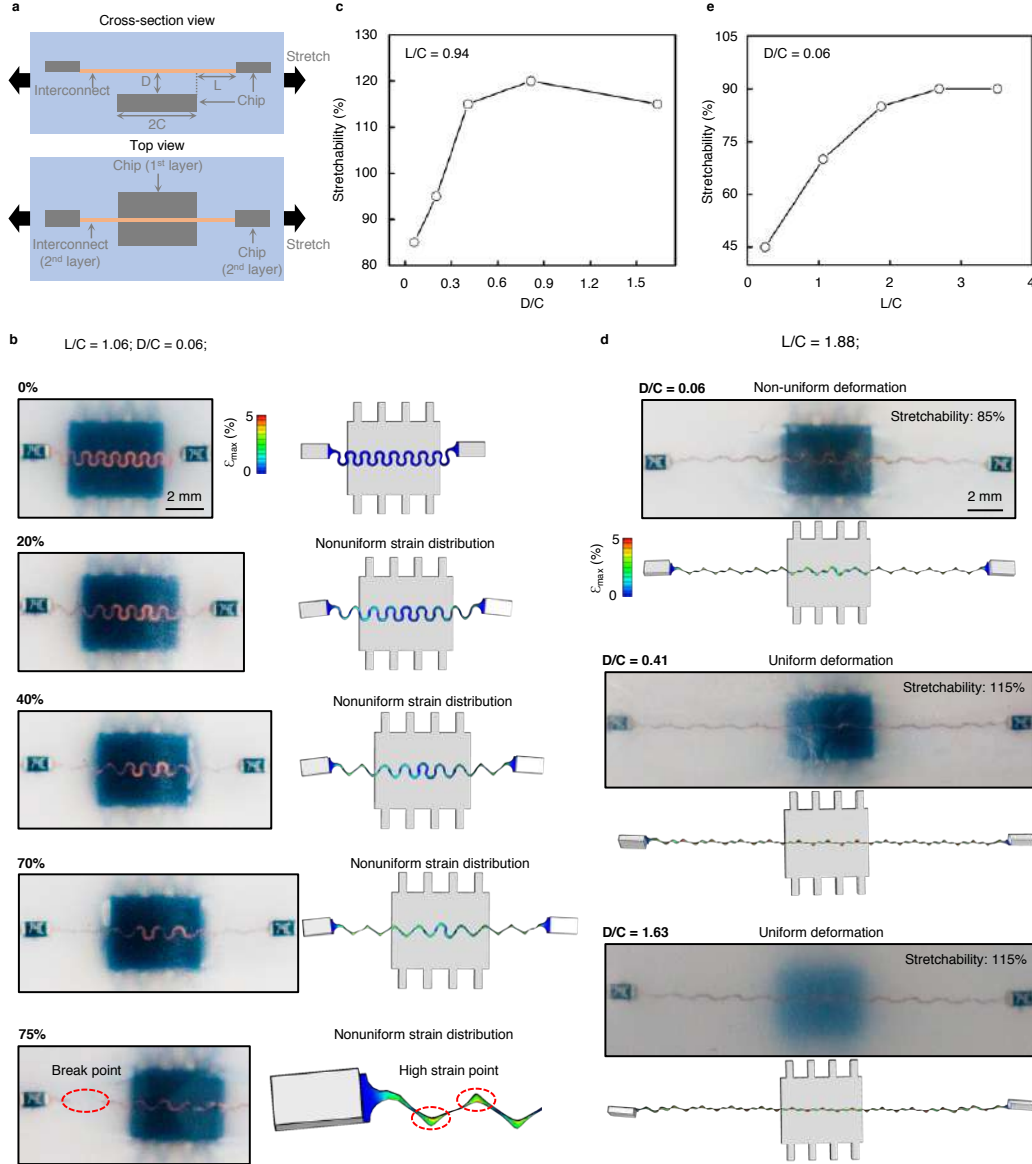
Supplementary Figure 3. Experimental studies of buckling deformations across the entire circuits under uniaxial stretching along the horizontal direction. Failure strain in the horizontal direction is $\sim 35\%$ with weak points at the interconnect between the crystal oscillator and capacitor. Plastic deformation begins at $\sim 30\%$ strain.



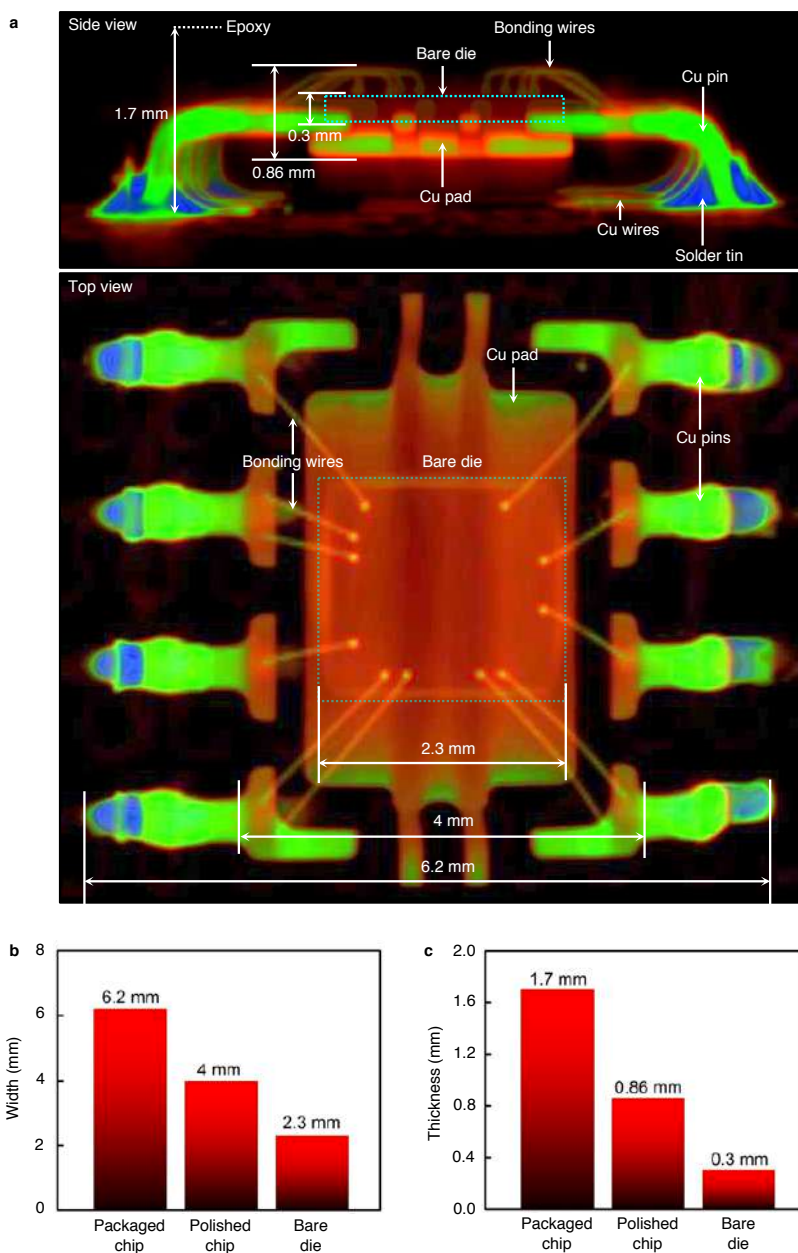
Supplementary Figure 4. Experimental studies of buckling deformations across the entire circuits under biaxial stretching. Failure strain for biaxial stretching is ~20% with weak points at the interconnect between the crystal oscillator and capacitor.



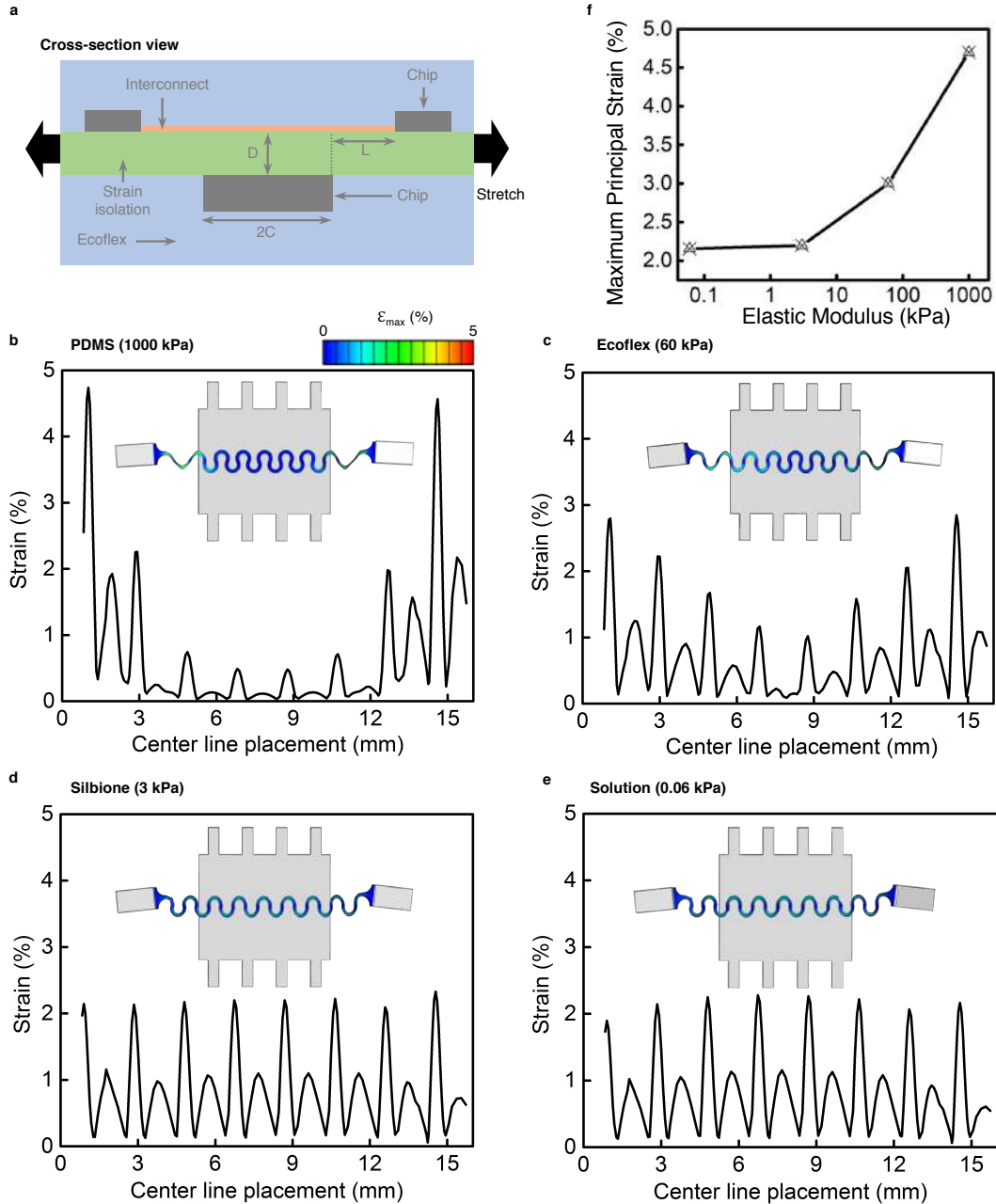
Supplementary Figure 5. Fatigue test of the three-dimensional integrated stretchable device with 10% uniaxial strain at a frequency of 0.5 Hz. **a**, Setup for the cycling test. A customized electrically controlled stretcher is used to apply 10% uniaxial strain at a frequency of 0.5 Hz to the device. Two cables with minimal mechanical footprint provide connection to an external power supply to the device. Bluetooth signals transmitted from the device are used as an indicator to identify whether the device is damaged during cycling test. **b**, Images of the device after different numbers of cycles. The device remains functional after being cycled for more than 2000 times. The failure mechanism can possibly be the debonding of the components from the Cu pads or the breakage of the interconnects in some strain concentrated areas, which is still under active investigation.



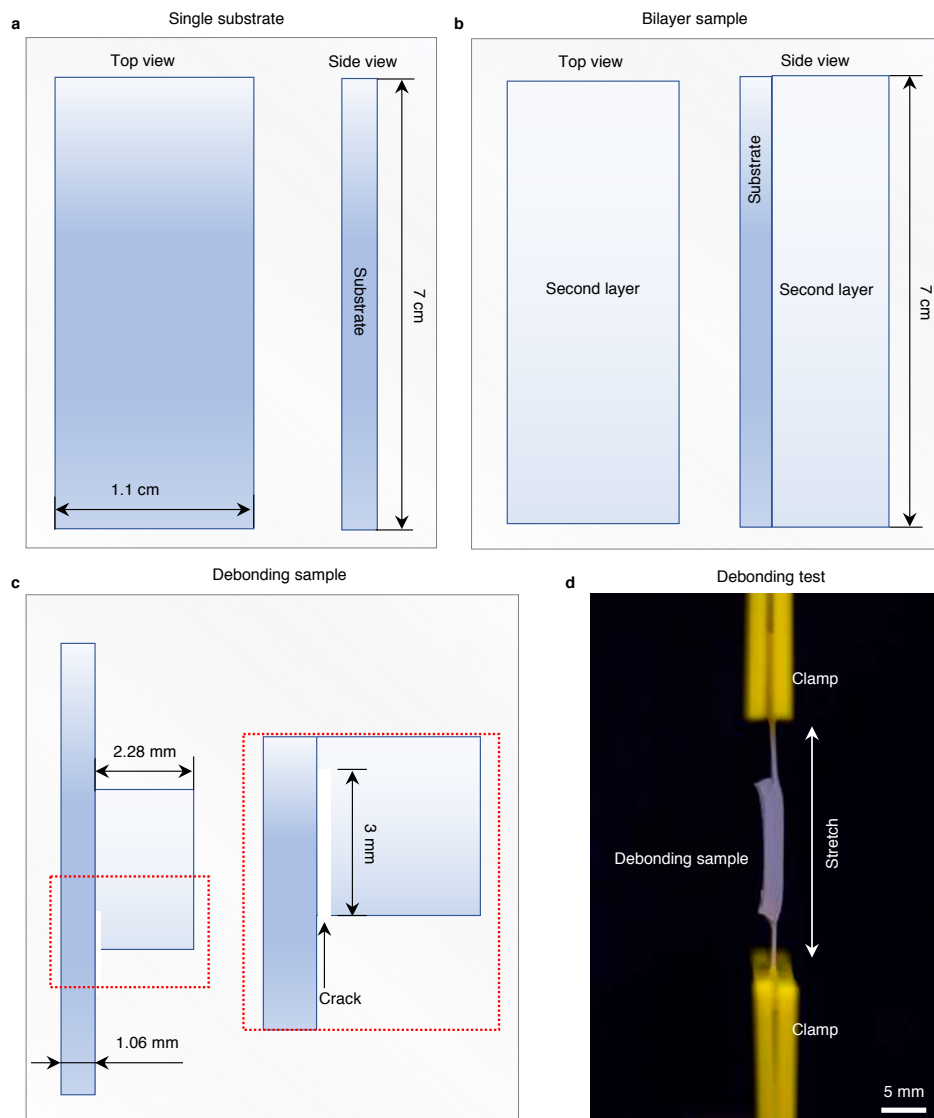
Supplementary Figure 6. Experimental and finite element analysis (FEA) studies of the mechanical coupling between layers of the multilayered device. **a**, Schematic cross-section and top view of a representative part of interest in the multilayered device. **b**, Experimental and FEA results with a uniaxial strain from 0% to 75%. Due to the constraint from the rigid chips, the strain distribution is nonuniform, as shown from the FEA strain distribution (ϵ_{max}) in the interconnect. With 75% strain, the serpentine interconnect was broken at the points of highly localized principal strain. **c**, The overall stretchability as a function of the normalized serpentine-chip separation distance D/C . Stretchability is enhanced by increasing the separation distance when $D/C < 0.4$ for the decreased mechanical coupling, and then tend to saturate when $D/C > 0.4$. **d**, Experimental and FEA results to show the decreased mechanical coupling between the layers by increasing the D/C . The interconnect strain distribution is nonuniform for low D/C (e.g., 0.06) and tend to be uniform for high D/C (> 0.4). **e**, The overall stretchability as a function of normalized non-constrained interconnect length L/C . Stretchability is enhanced by increasing the non-constrained interconnect length when $L/C < 2.7$, and then plateaus when $L/C > 2.7$.



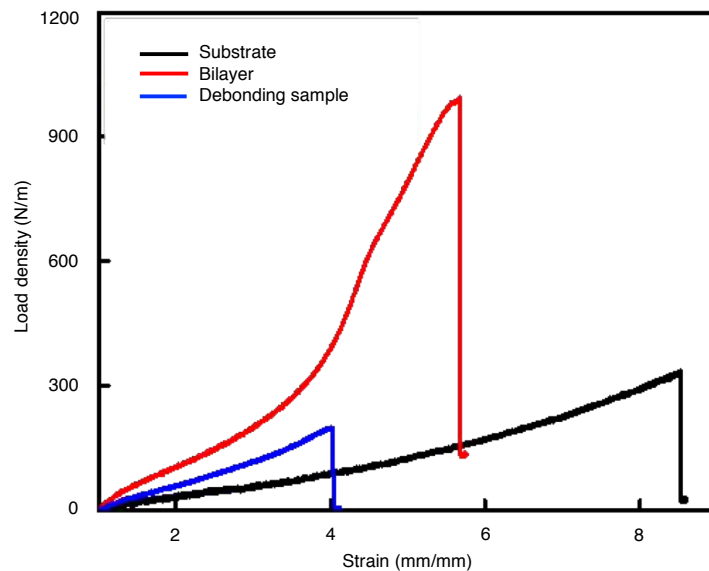
Supplementary Figure 7. XCT images of a typical functional chip (i.e., the amplifier) and summarized dimensions of the packaged chip, polished chip, and bare die. a, XCT images showing the amplifier structure in side and top views. It mainly contains the functional silicon bare die, Cu pins, bonding wires between the bare die and pins, and epoxy packaging (transparent in the XCT images). **b-c,** Summarized width and thickness of the chip with packaging, after polishing, or only bare die. This information can provide design guidelines for using different types of components to build stretchable electronics for different purposes, such as to decrease the device size or mitigate the constraints between layers.



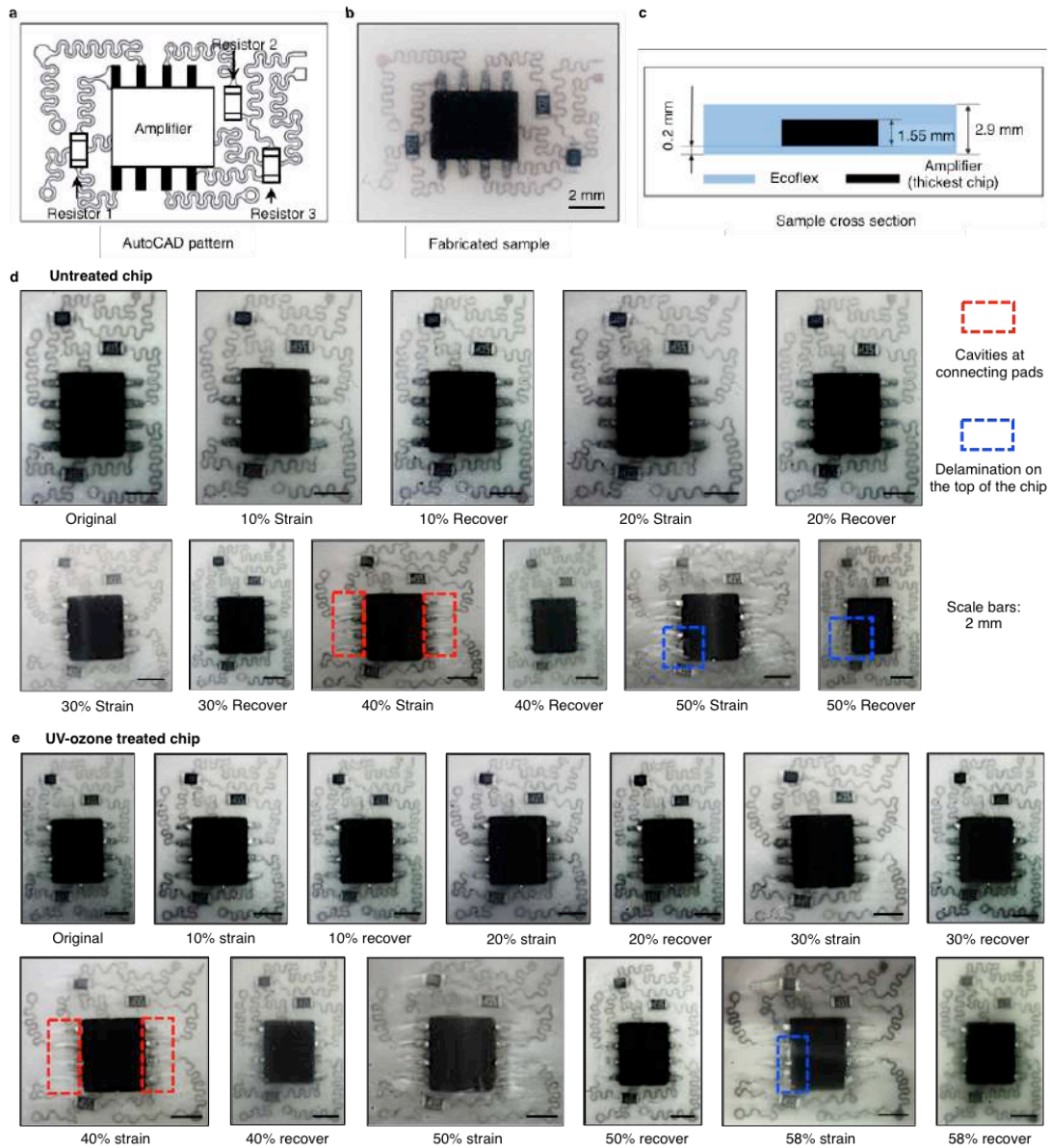
Supplementary Figure 8. Effect of strain isolation layer modulus on the overall stretchability. **a**, Cross-section view of the multi-layer device integrated with a strain isolation layer between adjacent layers. Key dimensions are labeled. To control the thickness of the device, the strain isolation layer was limited to thickness $D = 0.15$ mm with $D/C = 0.06$. And the interconnect length/chip width ratio L/C was controlled to be 1.06. **b-e**, FEA simulation results showing the interconnect center line strain distribution and the entire interconnects strain distribution (inset figure) when the device is under 20% stretching, with different strain isolation layer materials varied from PDMS to Ecoflex, Silbione, and liquid. **f**, The maximum principal strain of the interconnects with different isolation materials.



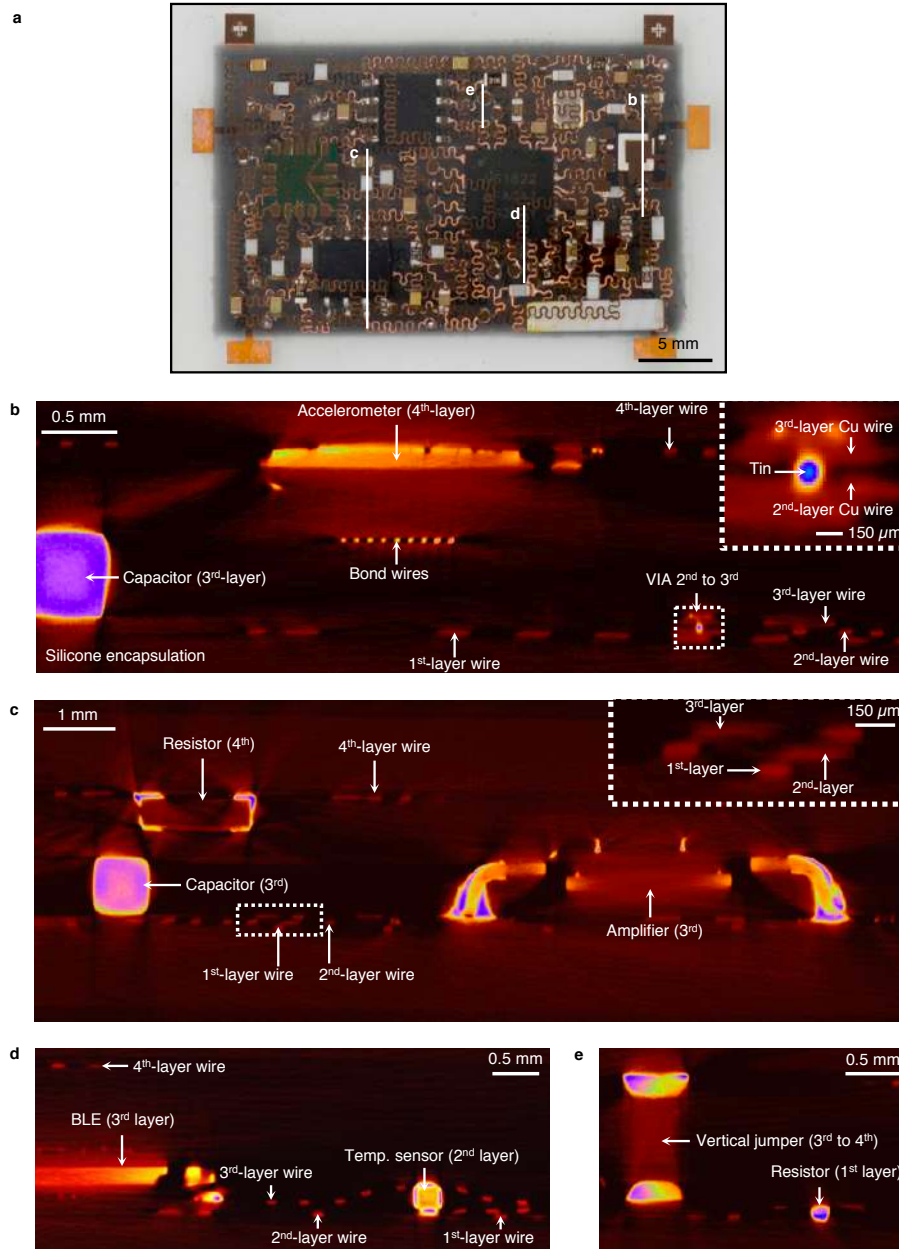
Supplementary Figure 9. Debonding test to show the adhesion between the Ecoflex layers in the 3D integrated stretchable system. **a**, Schematics of the top and side views of the single layer substrate. **b**, Schematics of the top and side views of the bilayer Ecoflex. **c**, Schematics of the side view of the debonding sample, with a pre-embedded crack (3 mm in depth). **d**, An image of the debonding experiment setup.



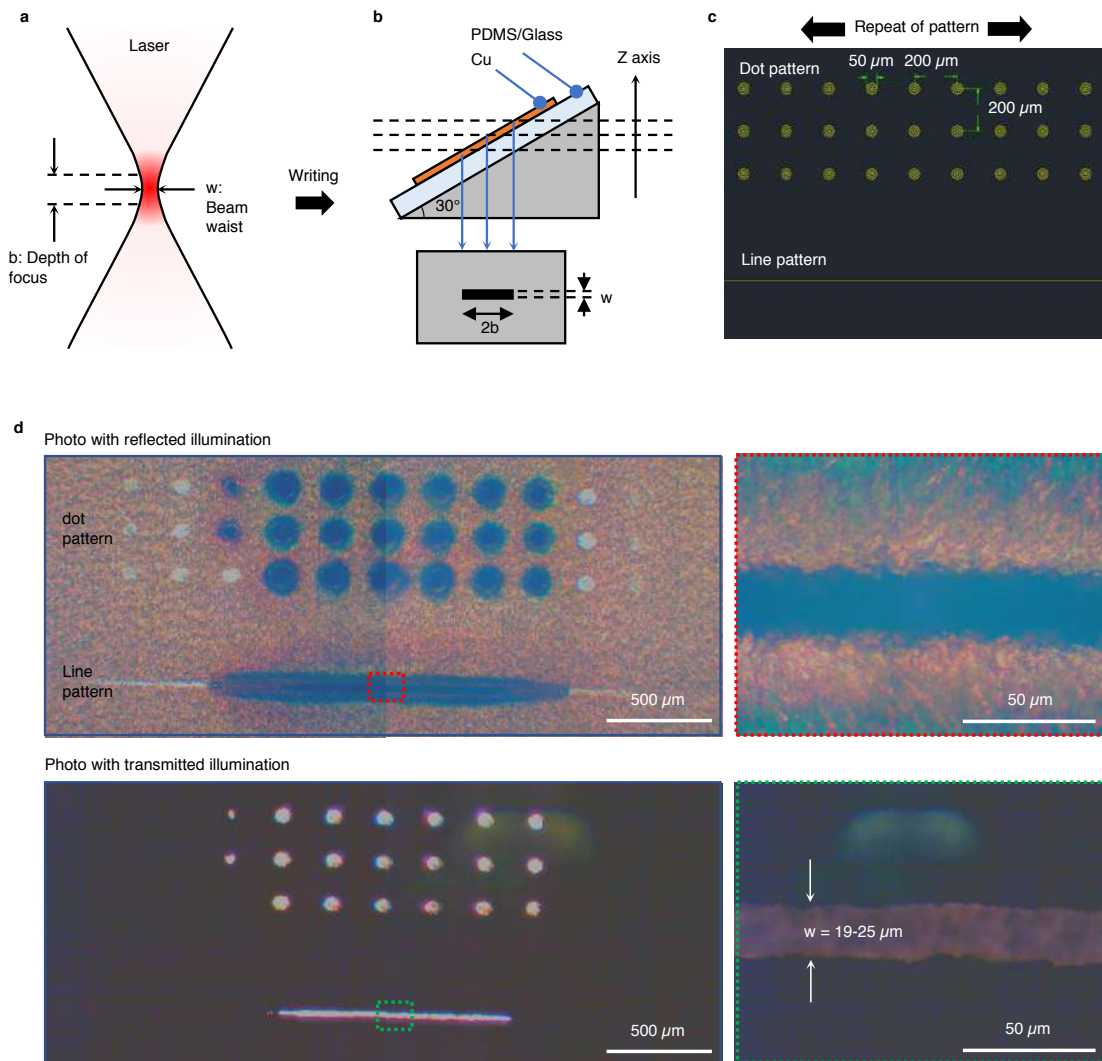
Supplementary Figure 10. Strain-Load density curve of the single Ecoflex substrate (black), bilayer sample (red), and debonding sample (blue) for debonding energy test between Ecoflex in different layers. For our samples, when the strain reached 400% in the debonding test, there was no deviation of the curve, which meant the delamination did not propagate. The sudden drops in the figure are the failure points when samples were broken due to the limited stretchability rather than the debonding.



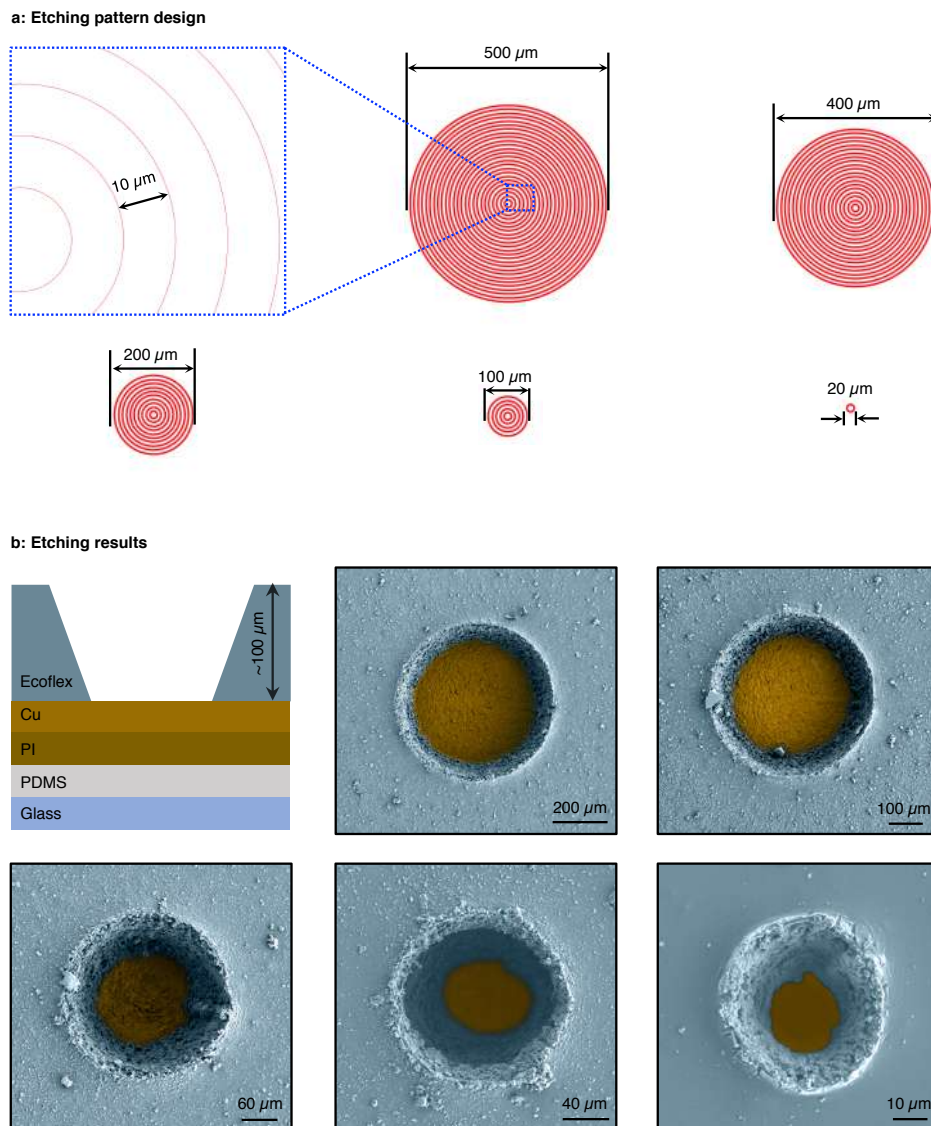
Supplementary Figure 11. Debonding test between the Ecoflex and chips. **a**, Layout design for a sub-unit of the circuit, which includes a main amplifier chip and several passive chips. **b**, The photograph of the corresponding fabricated sample. **c**, Sample cross section to illustrate the encapsulation scheme of the sample. **d**, Images to show the adhesion between the Ecoflex and untreated chips at different levels of strain. The delamination appears first on connecting pins at around 40% strain. Delamination from the epoxy material on the chip top surface starts at a strain of 50%. Additionally, the delamination on connecting pins can recover because of the smooth surfaces of both the pin and the as-mounded Ecoflex, but delamination on the epoxy still exist after releasing the strain because of the rough surfaces of the epoxy and as-mounded Ecoflex. **e**, Images to show the adhesion between the Ecoflex and UV-ozone treated chips at different levels of strain. With UV ozone treatment, there is no delamination on the epoxy until 58% strain, which is larger than the untreated chips, indicating the enhanced bonding with UV ozone processing.



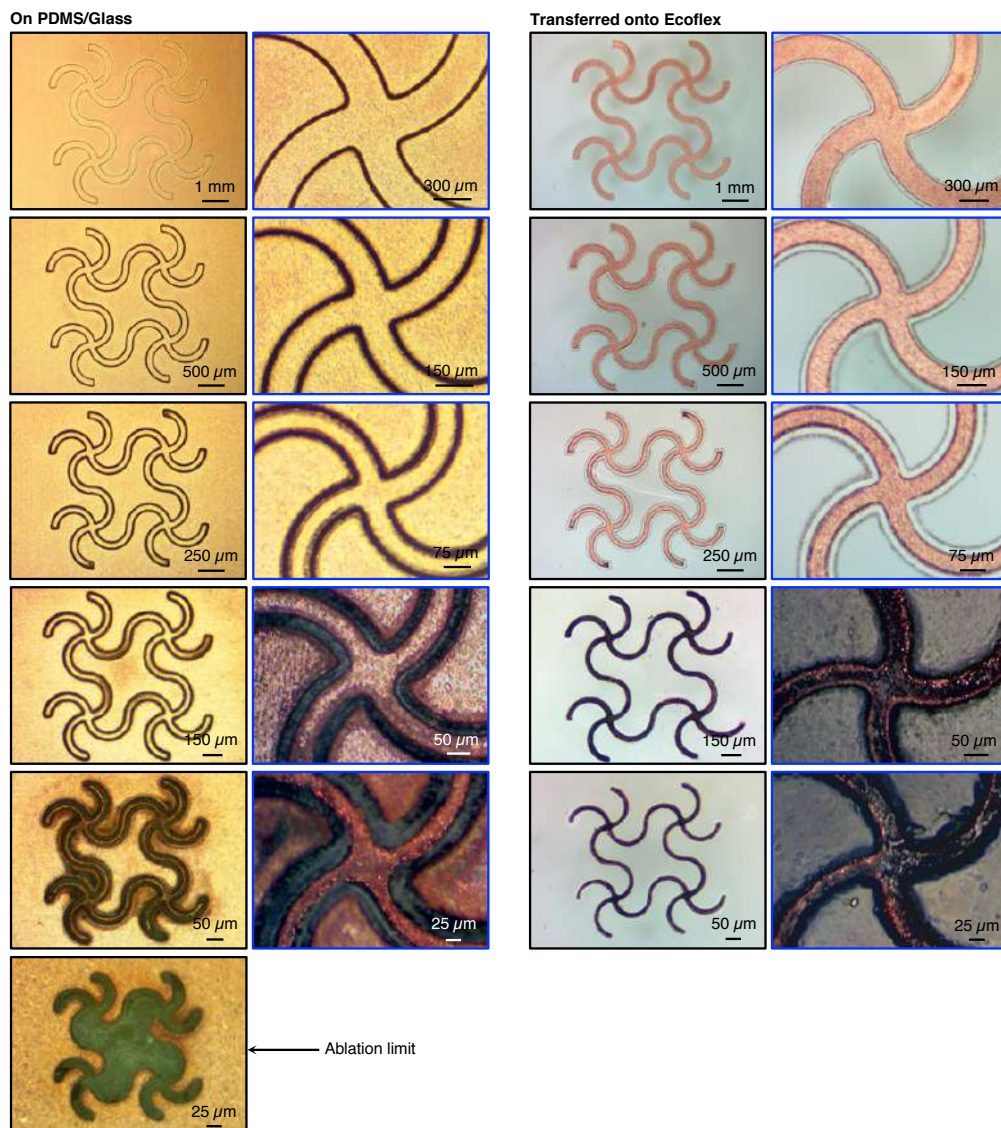
Supplementary Figure 12. X-ray computed tomography (XCT) images showing the cross-sectional structure of the three-dimensional integrated stretchable device. **a**, An optical image of the integrated device, with markers showing the cross-sectional positions corresponding to **(b)**, **(c)**, **(d)**, and **(e)**. The key components and structures are labeled.



Supplementary Figure 13. Evaluation of the effective laser beam size and depth of focus. **a**, Schematic illustration of the laser beam. There are two key parameters: beam waist (w) and depth of focus (b). **b**, A Cu foil on a 30° tilted surface to be processed using the laser with the pattern design shown in **(c)**. According to the ablation results, shown in **(d)**, and tilted angle degree, the laser beam waist and depth of focus can be calculated to be $\sim 25\ \mu\text{m}$ and $\sim 600\ \mu\text{m}$, respectively.

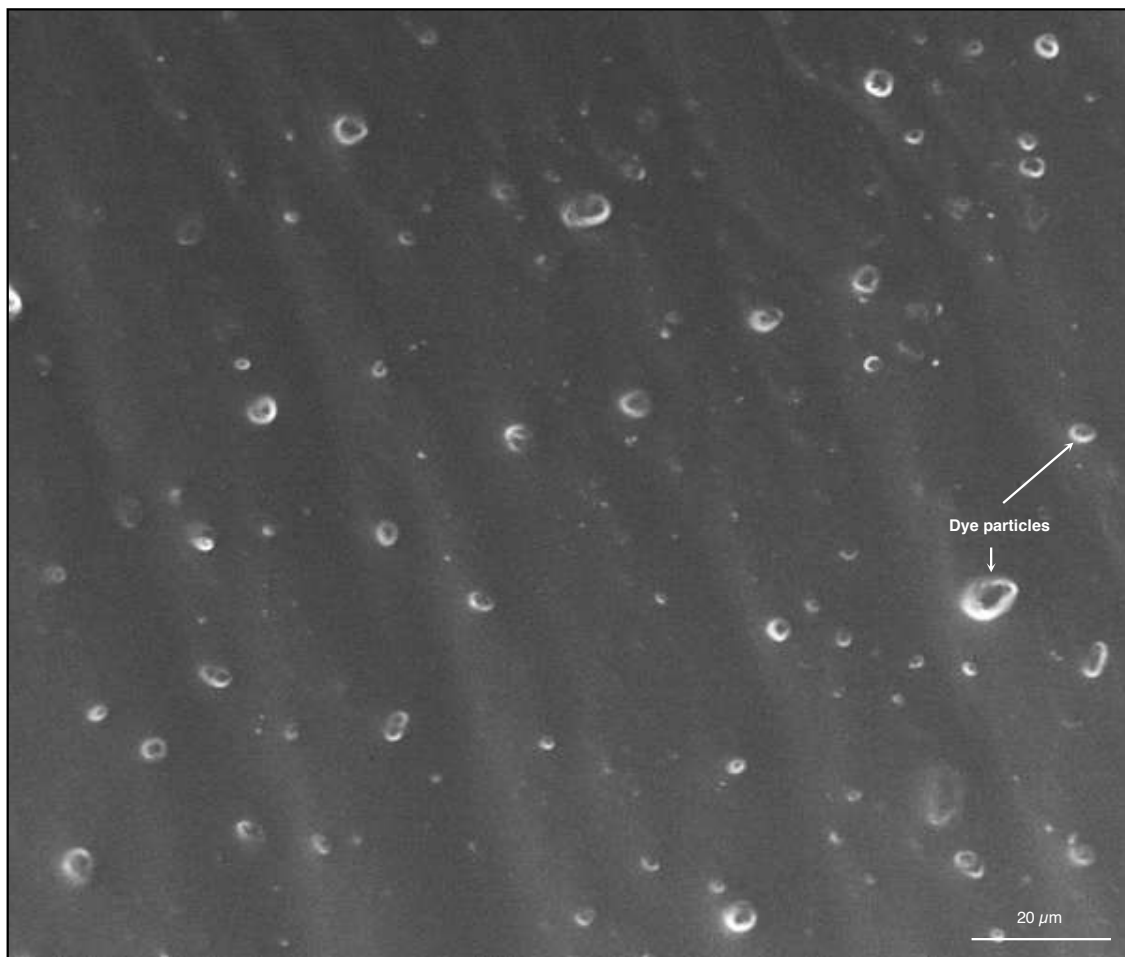


Supplementary Figure 14. Evaluation of the laser fabricated VIA resolution in silicone. a, Pattern design of laser ablation with diameters from 500 μm to 20 μm . **b,** Selective ablation of silicone on the top of the Cu with the corresponding laser pattern shown in (a). The smallest diameter of VIA that can be fabricated on 100 μm thick silicone is $\sim 45 \mu\text{m}$, as shown in the lower right image in (b).

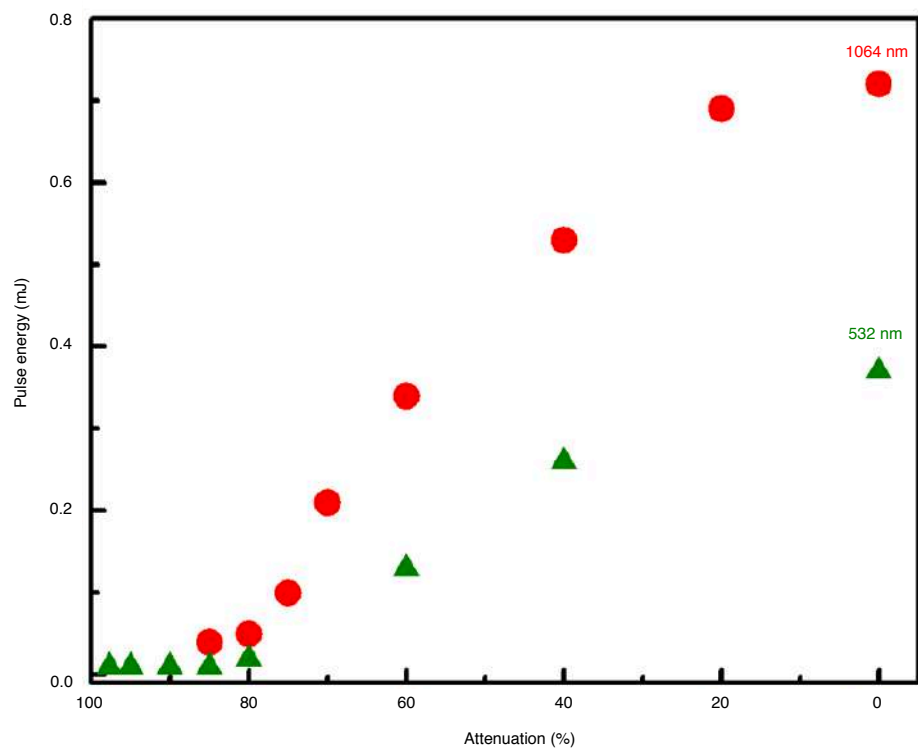


Supplementary Figure 15. Evaluation of pattern resolution of laser ablation in Cu/PI films.

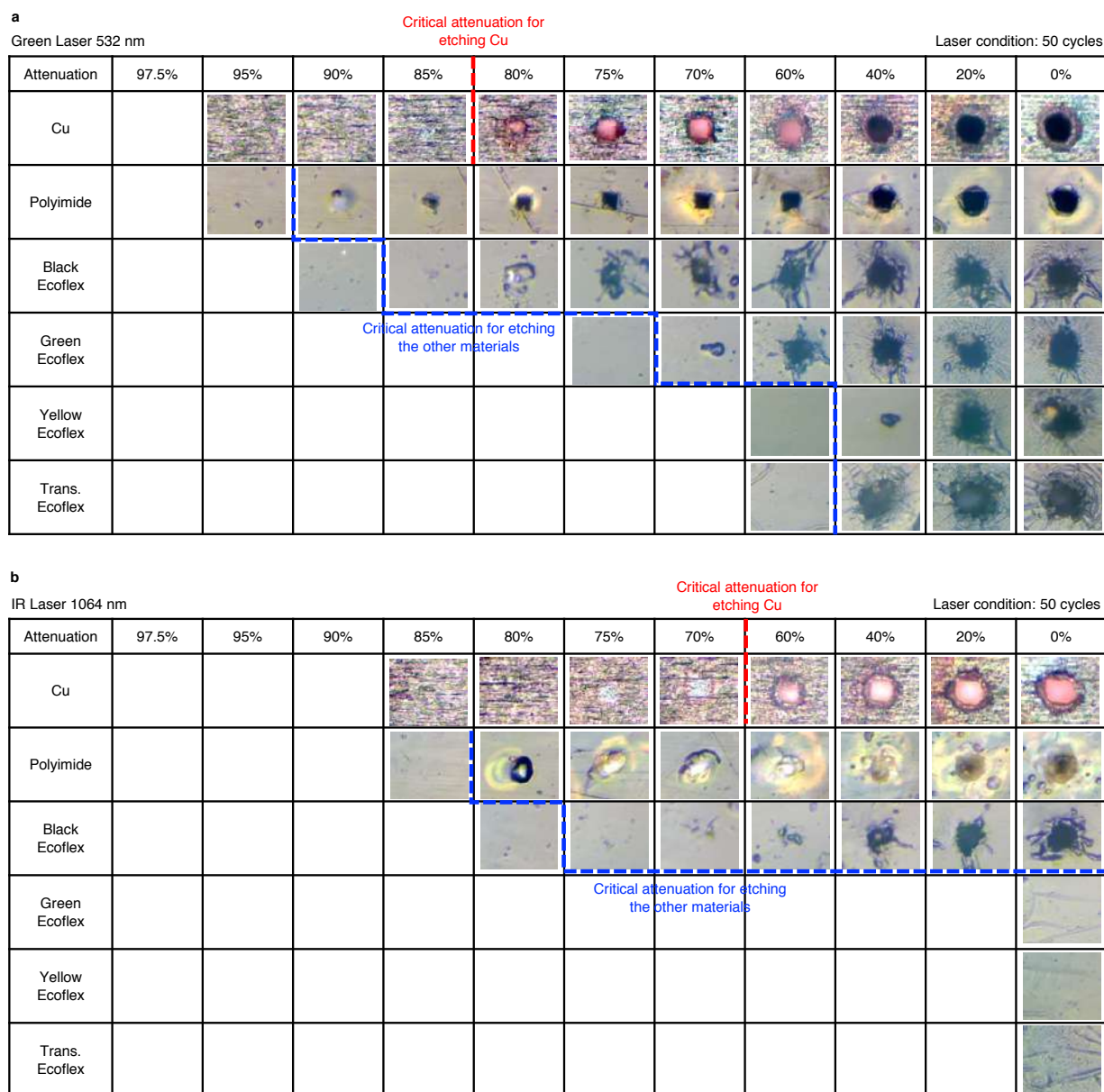
Parameters of wavelength 1064 nm, pulse energy 0.42 mJ, and 10 cycles are used to write the serpentine pattern in the Cu/PI on the PDMS/glass substrate. Then the patterned Cu/PI electrodes are transferred onto the Ecoflex substrate with a water-soluble tape. The patterned electrodes, before transfer (left two columns) and after transfer (right two columns), with the width ranging from 300 μm (first row) to 10 μm (second to the last row), are shown. For electrodes with the width less than 10 μm, as shown in the last row, the PDMS substrate is not sticky enough to hold very thin electrodes that would be delaminated by the pressure waves from the laser ablation. The black color on the electrode is due to the thermal oxide on the Cu surface.



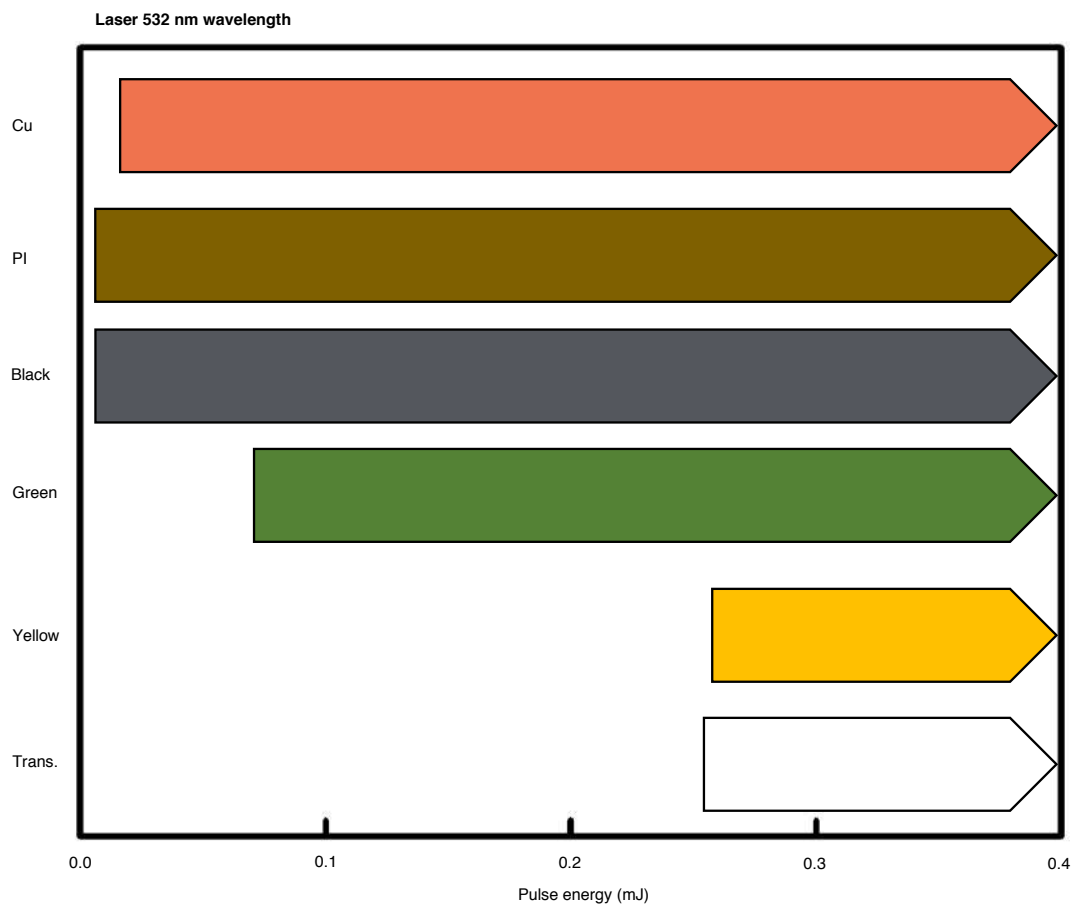
Supplementary Figure 16. An SEM image of the silicone modified with 3% wt black dye. The uniformly distributed small particles with diameters ranging from 2 to 5 μm can increase the light absorption of the silicone.



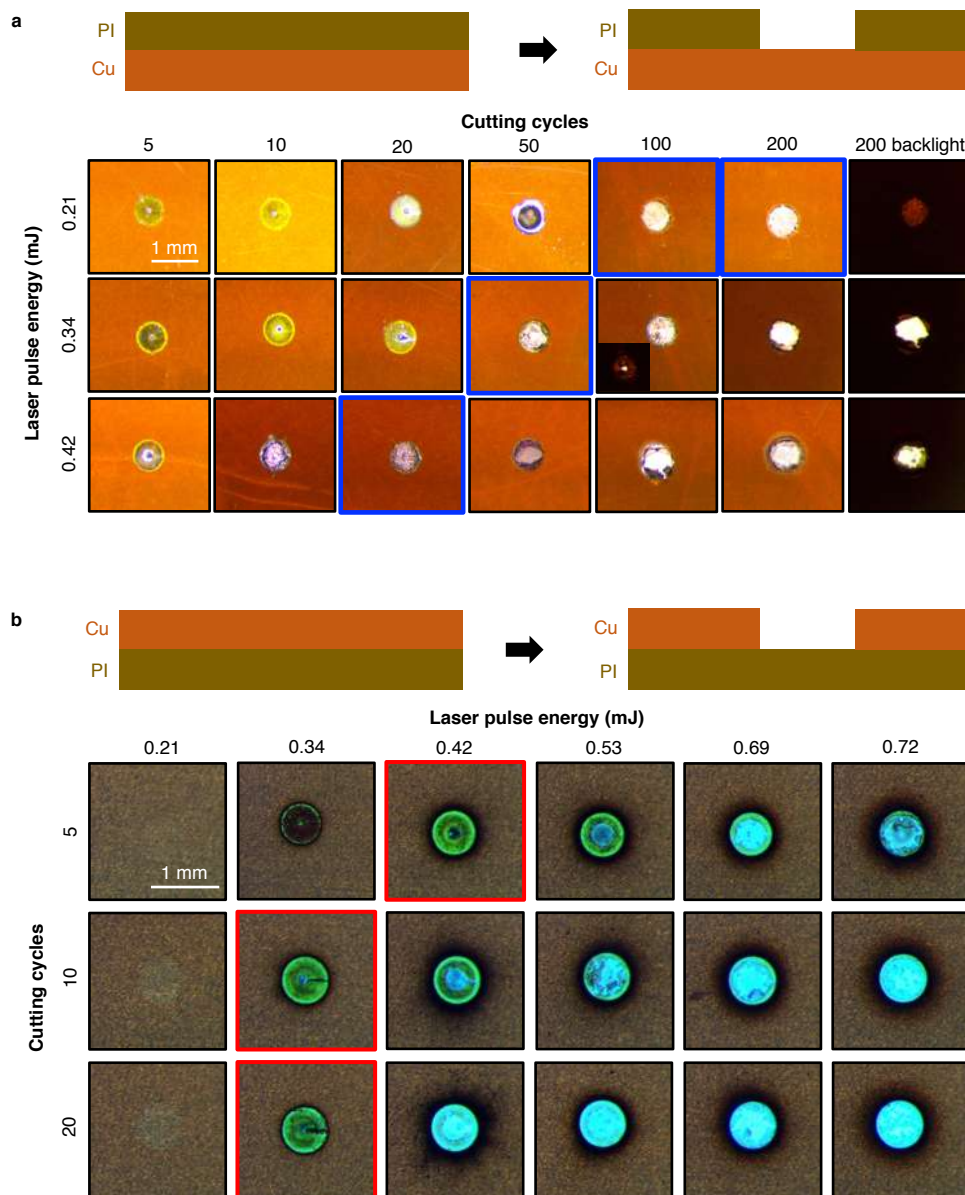
Supplementary Figure 17. Laser pulse energy controlled by the lens attenuation system. The Nd:YAG laser pulse energy is calibrated by an energy meter.



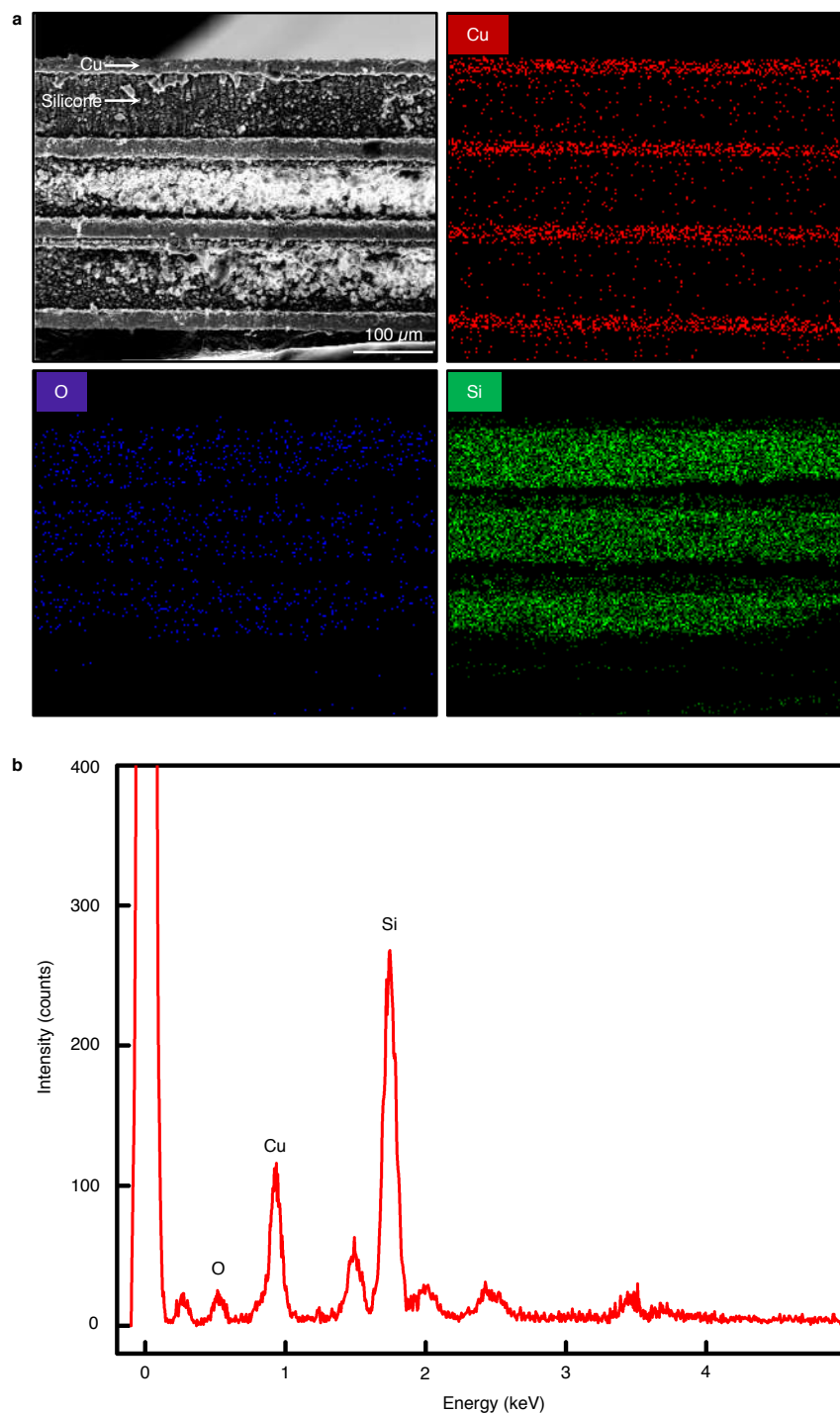
Supplementary Figure 18. Ablation of different materials with laser wavelengths of (a) 532 nm and (b) 1064 nm. The red lines are the critical attenuation that can ablate Cu. The blue lines are the critical attenuation for ablating other materials. For 532 nm, it can be used to etch Cu, PI, and silicone without and with dye modifications. For 1064 nm, it is suitable to etch Cu, PI, and the silicone modified with only the black dye. Materials, whose critical attenuation is larger than Cu, can be selectively ablated in the presence of Cu.



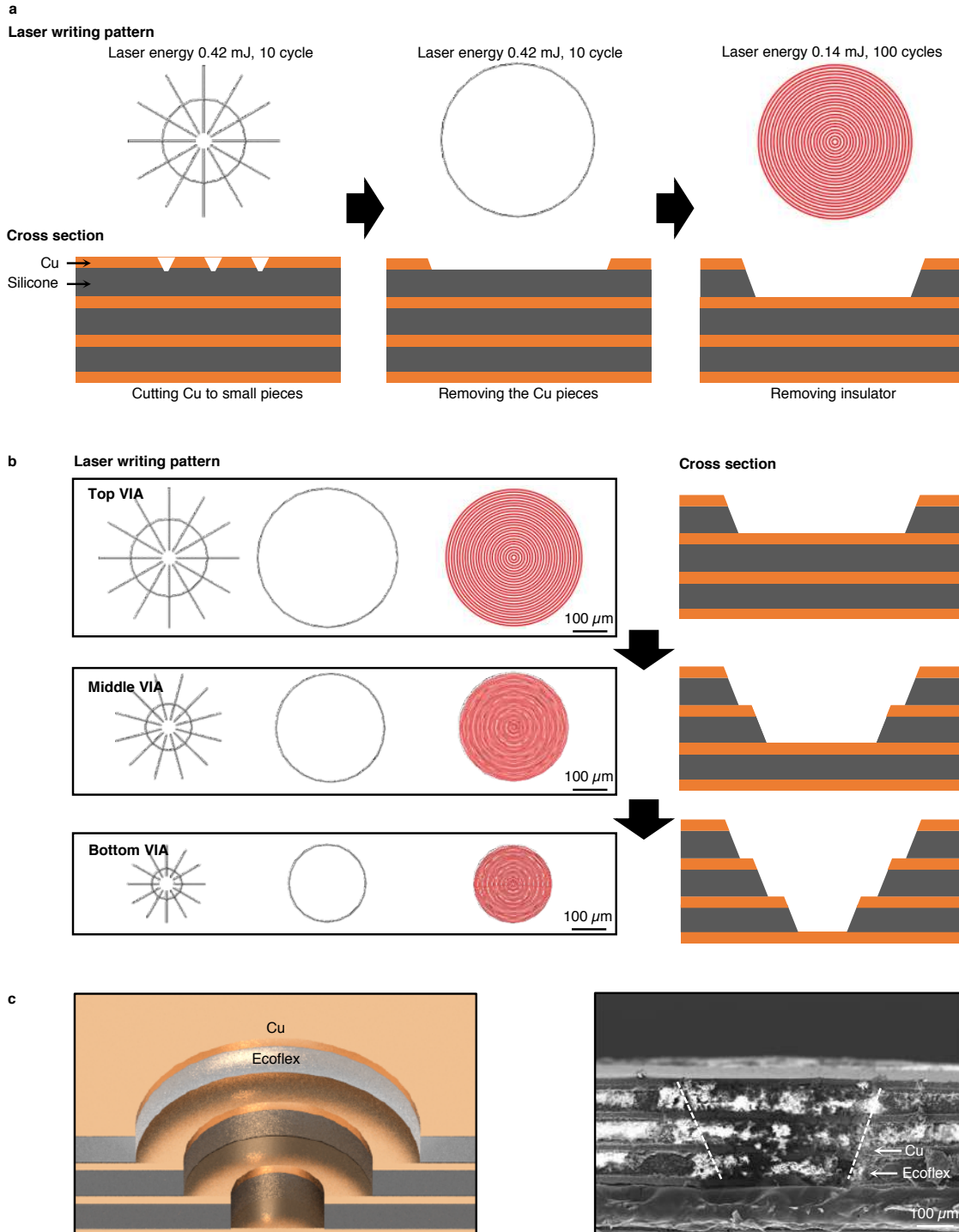
Supplementary Figure 19. Ablation pulse energy of the laser with 532 nm wavelength for Cu, PI, and silicone with different colors. The threshold pulse energies for Cu, PI, and black silicone are too close to allow selective ablation.



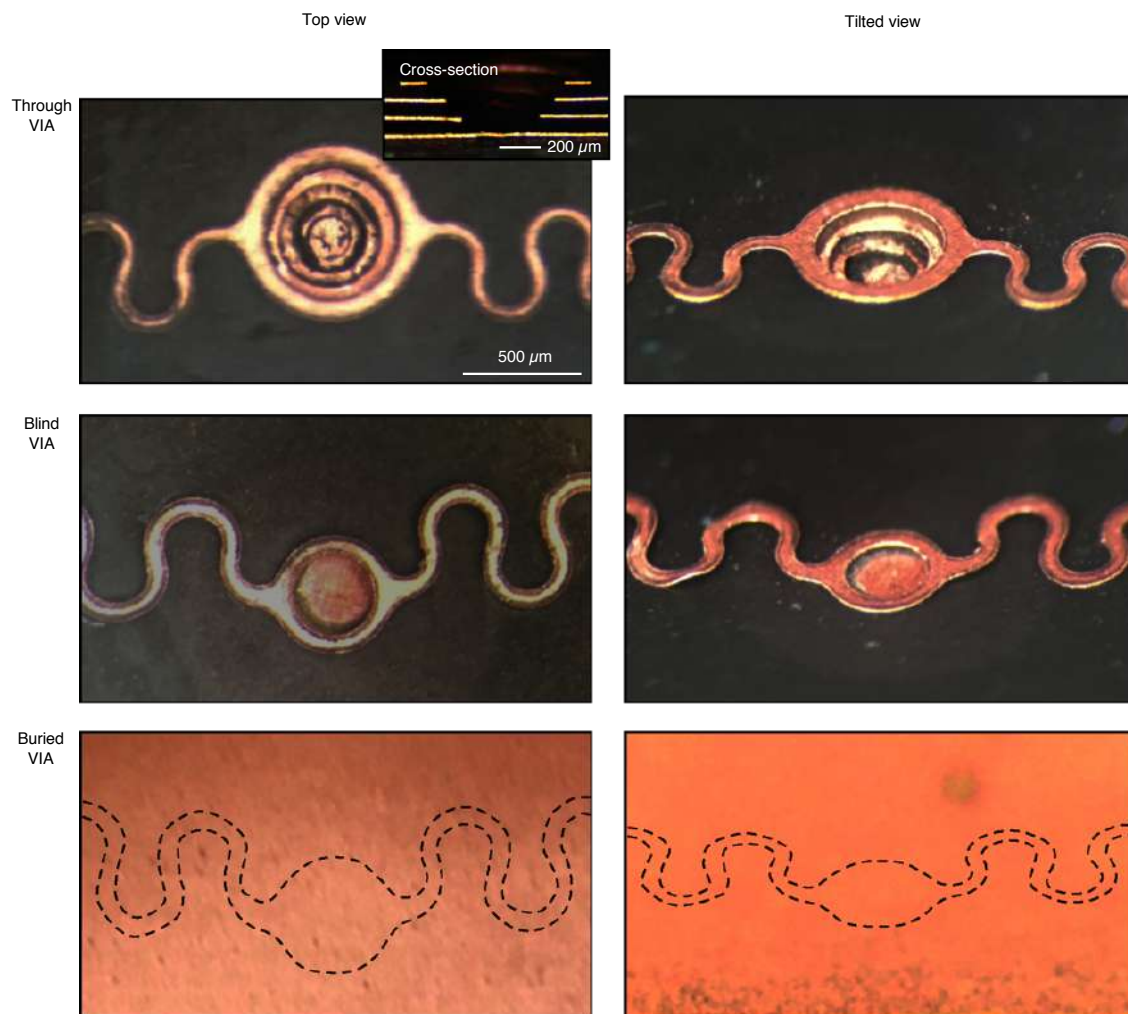
Supplementary Figure 20. Selective laser ablation of Cu (~20 μm) and PI (~14 μm). Laser (1064 nm) with different pulse energies or ablation cycles is used to selectively remove PI on Cu (**a**) or Cu on PI (**b**). As the critical pulse energy for PI (0.05 mJ) is lower than Cu (0.34 mJ), it's easy to selectively remove PI from the bottom Cu by controlling the laser pulse energy at 0.21 mJ. No matter how many processing cycles are used, the bottom Cu is still safe, as shown in the first row of (**a**). To remove Cu from PI is very tricky, but can be achieved by controlling the processing cycles. If more cycles are used, the bottom PI will also be ablated, as shown in (**b**).



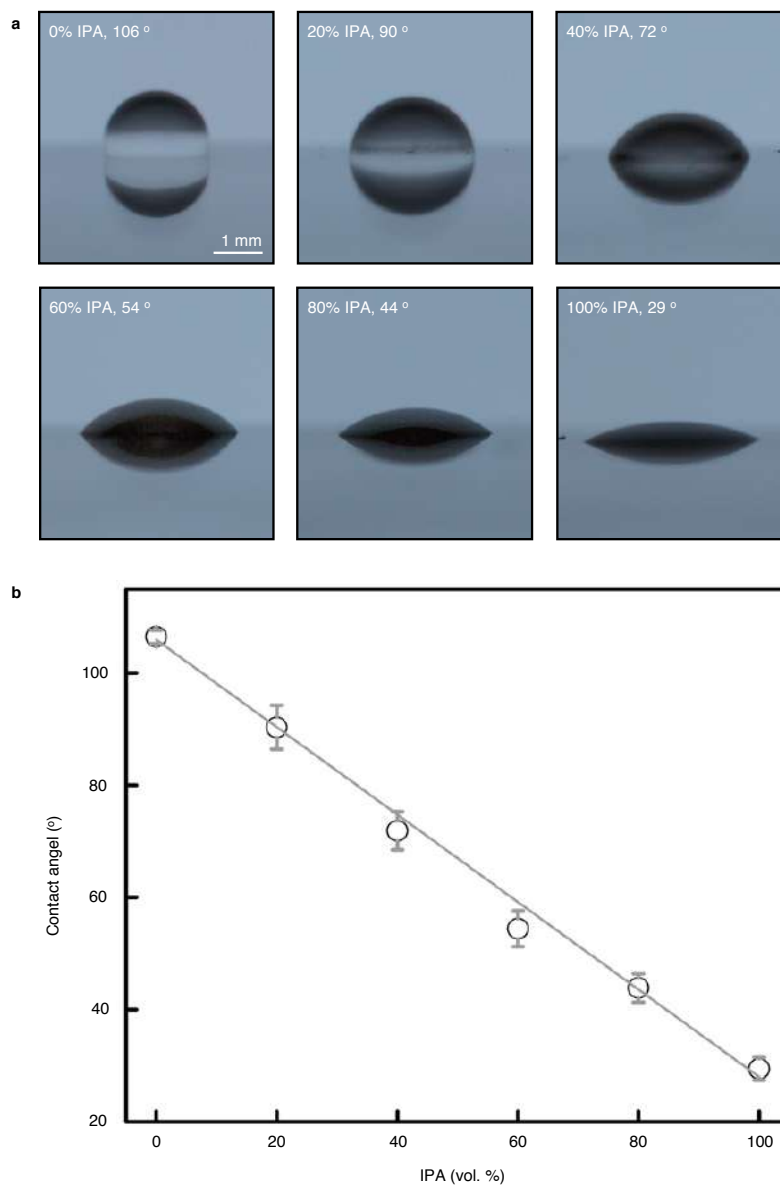
Supplementary Figure 21. Multilayer Cu insulated by soft silicone to fabricate the VIAs. a, A SEM image and corresponding EDS mapping graphs of the multilayer structure. **b,** EDS spectrum showing the elements included in the sample.



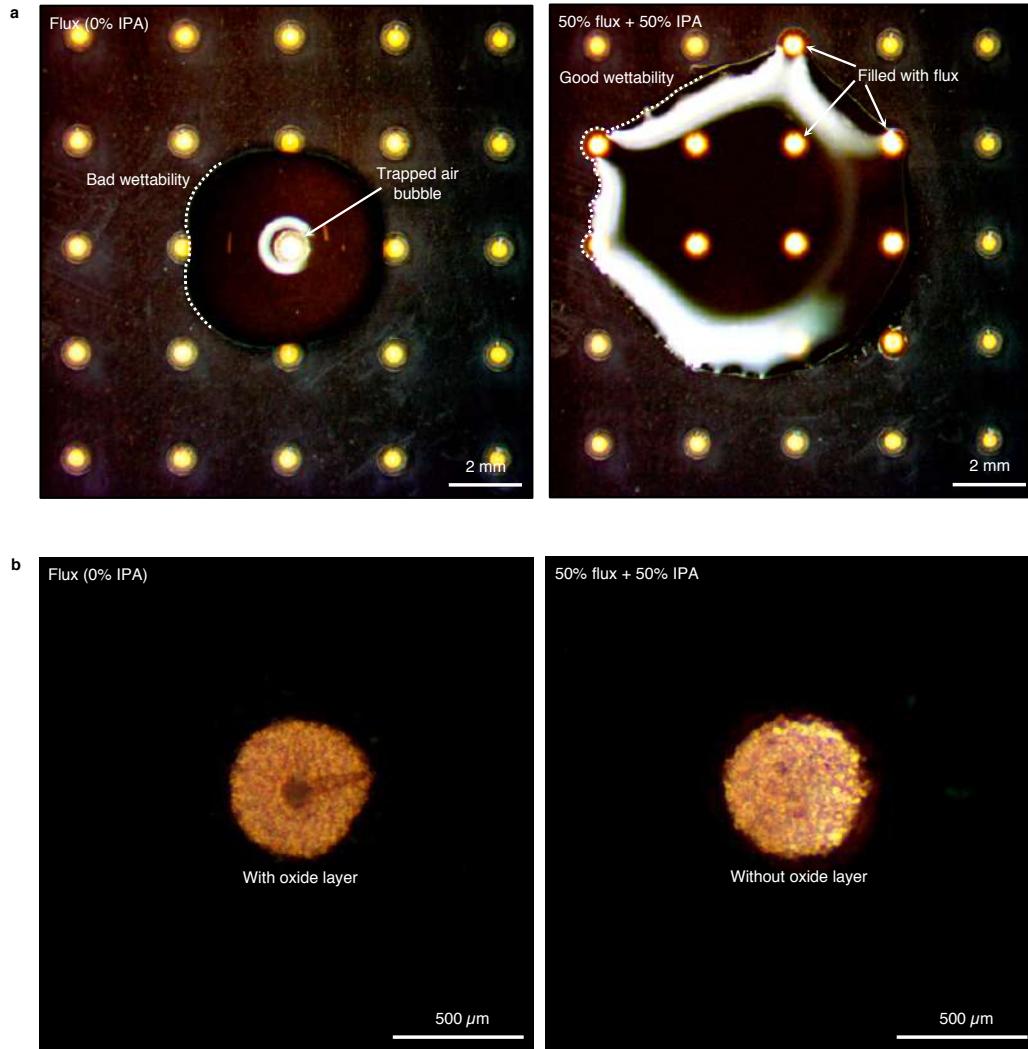
Supplementary Figure 22. Design of laser (1064 nm) ablation process for selectively ablating Cu and black silicone to build a through VIA. **a**, Laser cutting pattern design (top row) and corresponding schematics showing the ablation results (bottom row). With the first pattern, Cu will be cut into small pieces. With the second pattern, Cu will delaminate from the silicone substrate automatically, due to the residual thermal stress. **b**, Serial pattern designs to build the through VIA. **c**, Schematics (left) and an SEM image (right) of the through VIA.



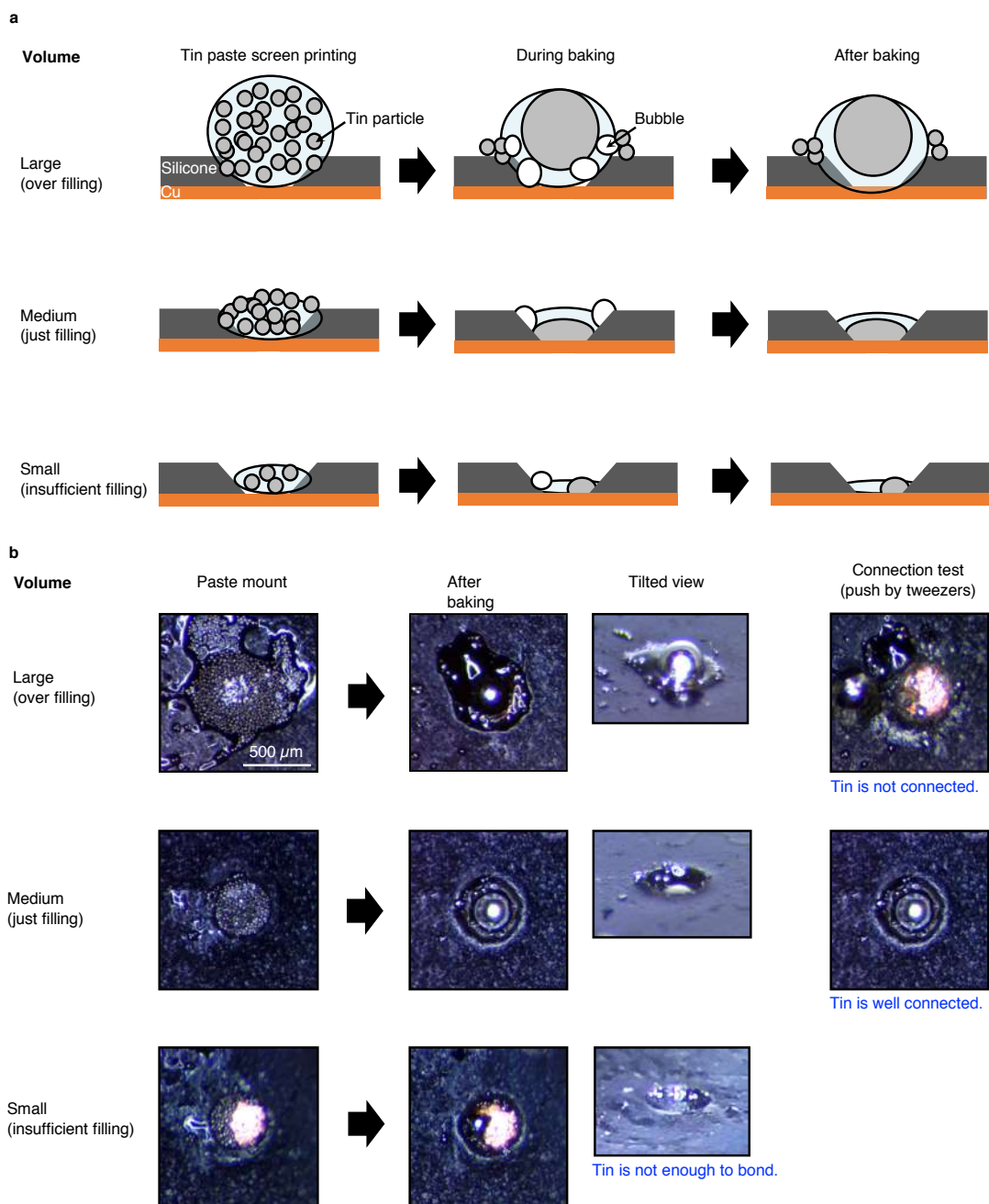
Supplementary Figure 23. Images of all three types of VIAs. Optical images show the top view and tilted view of the VIAs. All images share the same scale bar. The inset figure shows the cross-section of the through VIA.



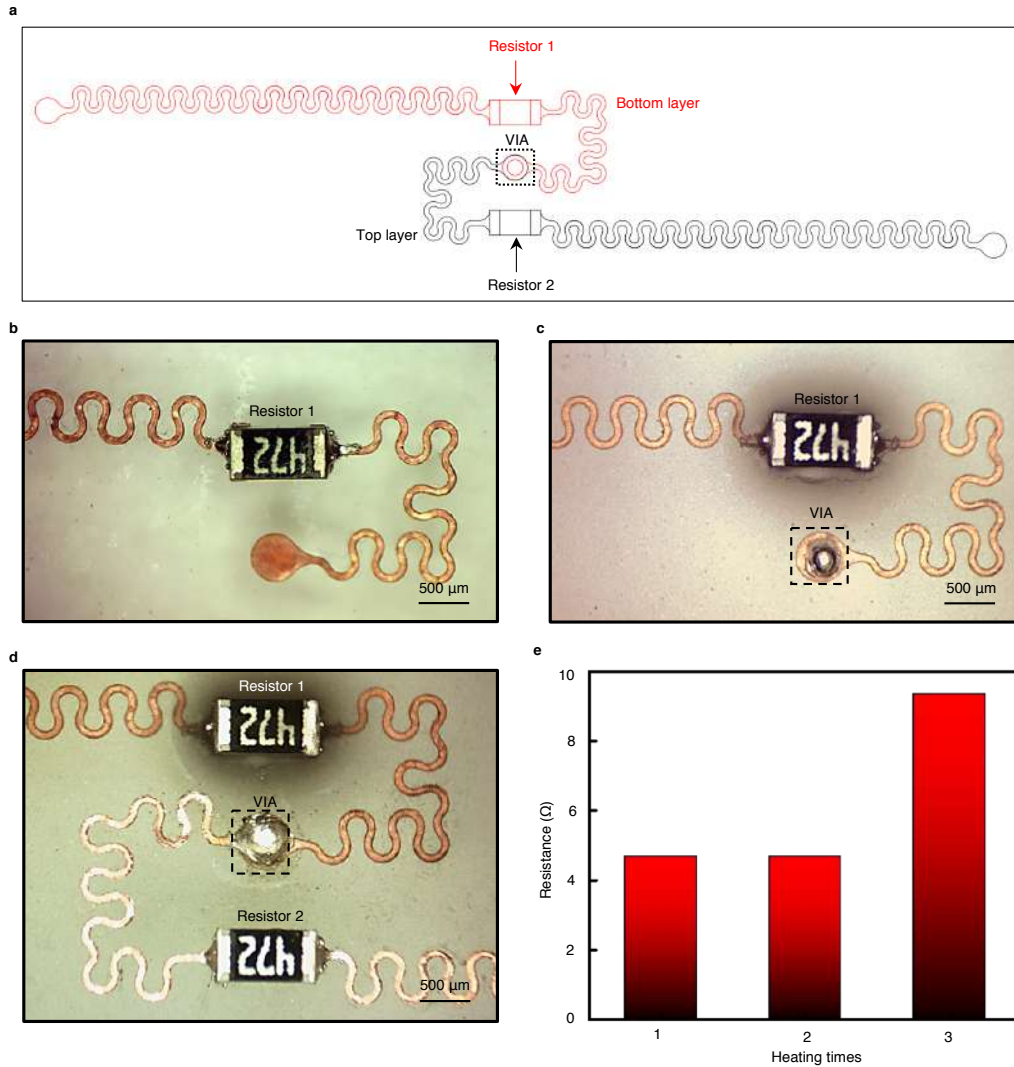
Supplementary Figure 24. Control of the contact angle of flux (aqueous solution) with silicone (black Ecoflex) by mixing with IPA. a, Images showing the contact angle of flux mixed with IPA of volume percentile from 0% to 100%. All images share the same scale bar. **b,** The linear relationship between the contact angle and the IPA volume percentile.



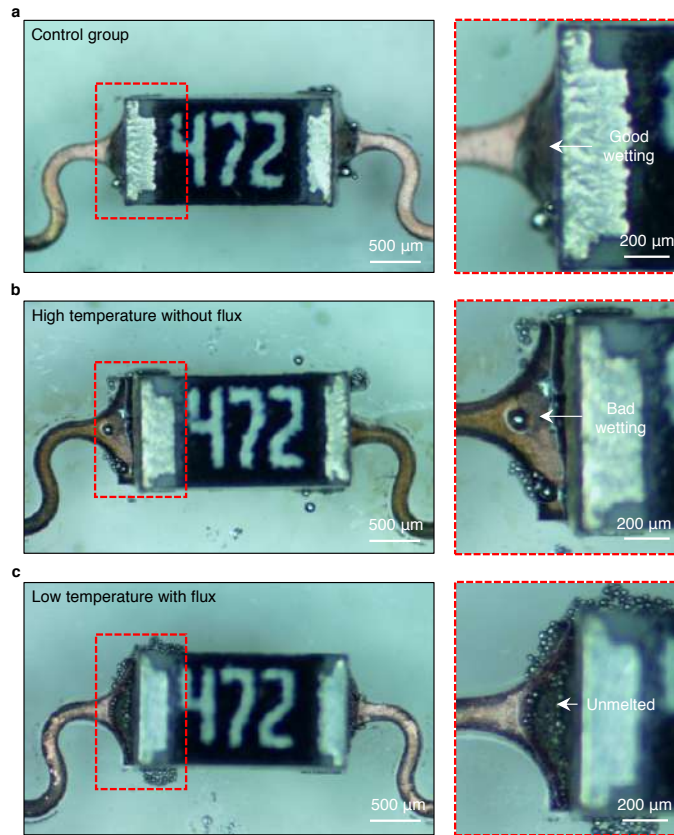
Supplementary Figure 25. Comparison of the VIA surface with and without Cu oxide by flux. a, Wettability of flux only (left) and 50% flux + 50% IPA (right). The flux cannot go into the VIAs due to its large contact angle with silicone. With 50% IPA, the contact angle decreases, which improves the wettability on silicone. Each droplet volume is $\sim 80 \mu\text{L}$. **b,** The comparison of cleaned Cu surfaces with flux only (left) and 50% flux + 50% IPA (right).



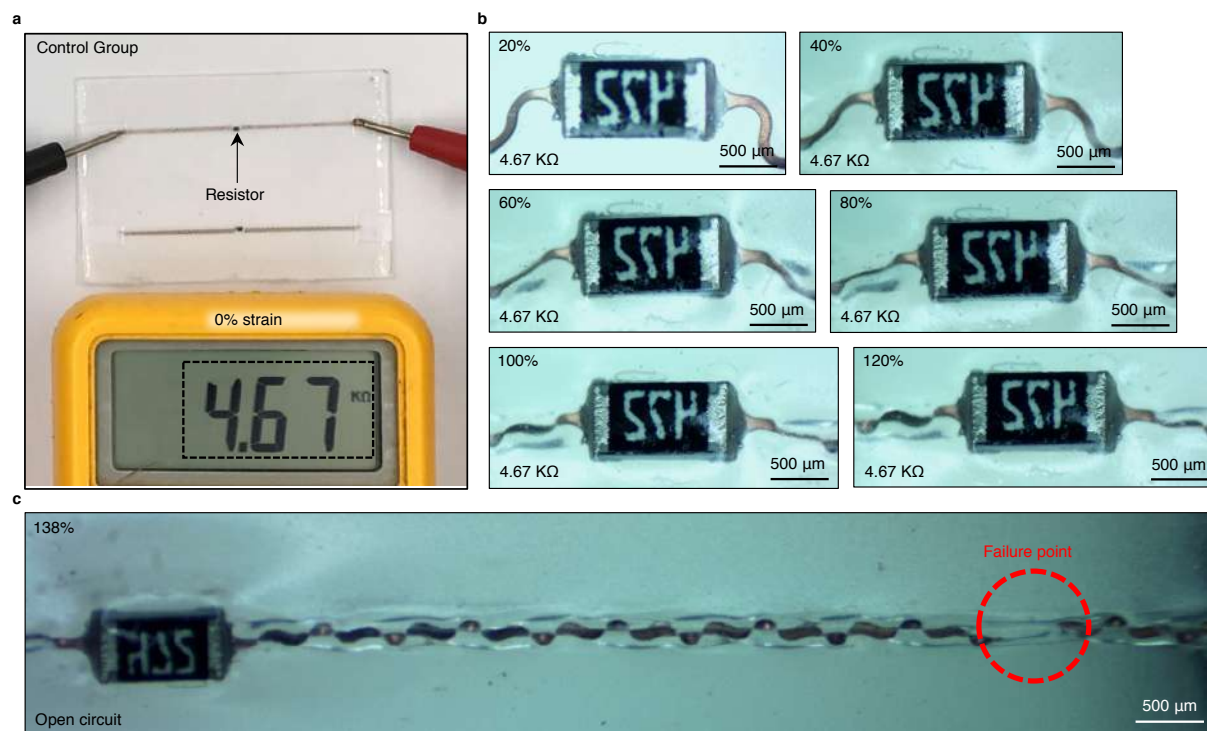
Supplementary Figure 26. Schematic illustration of curing the tin paste with different amounts by screen-printing. **a**, During baking, small tin particles will melt and merge to form big tin balls. At the same time, the flux will boil and generate some bubbles. If there is too much paste, the flux will generate too many bubbles that will push the tin ball to separate from the bottom Cu. On the other side, if the paste amount is not enough, it will not be able to cover the entire bottom Cu pad surface. Therefore, a suitable amount of paste is necessary to form robust and reliable bonding with the exposed Cu pads. **b**, Experimental results showing the bonding behavior. All images share the same scale bar.



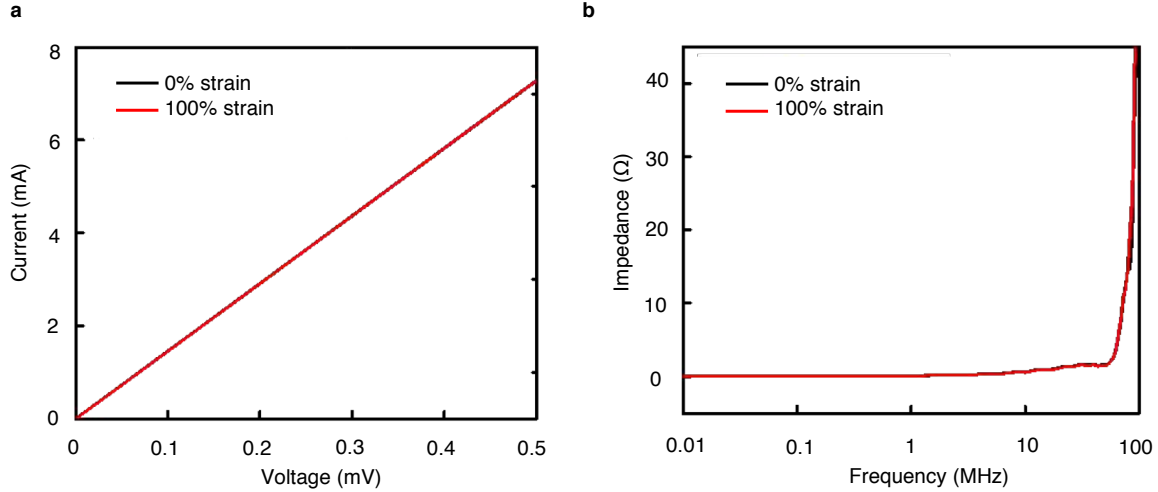
Supplementary Figure 27. Electrical performance testing after thermal expansion of the Ecoflex. We designed a simple experiment to test how the second heating impacts the previously soldered parts. Electrical characterizations were carried out after each separate fabrication step. **a**, Circuit diagram with two 4.68 kΩ resistors in two separate layers that are connected by a VIA. **b**, Image of the bottom layer after bonding (first heating). **c**, Image of the bottom layer after the tin VIA formation (second heating). **d**, Image of the two-layer circuit after the second layer bonding (third heating). **e**, Resistance value during the circuit fabrication process. The series resistance exactly equal to the sum of the top and the bottom resistance value. That means the second heating did not change the value of the firstly-soldered part, or likely to damage it.



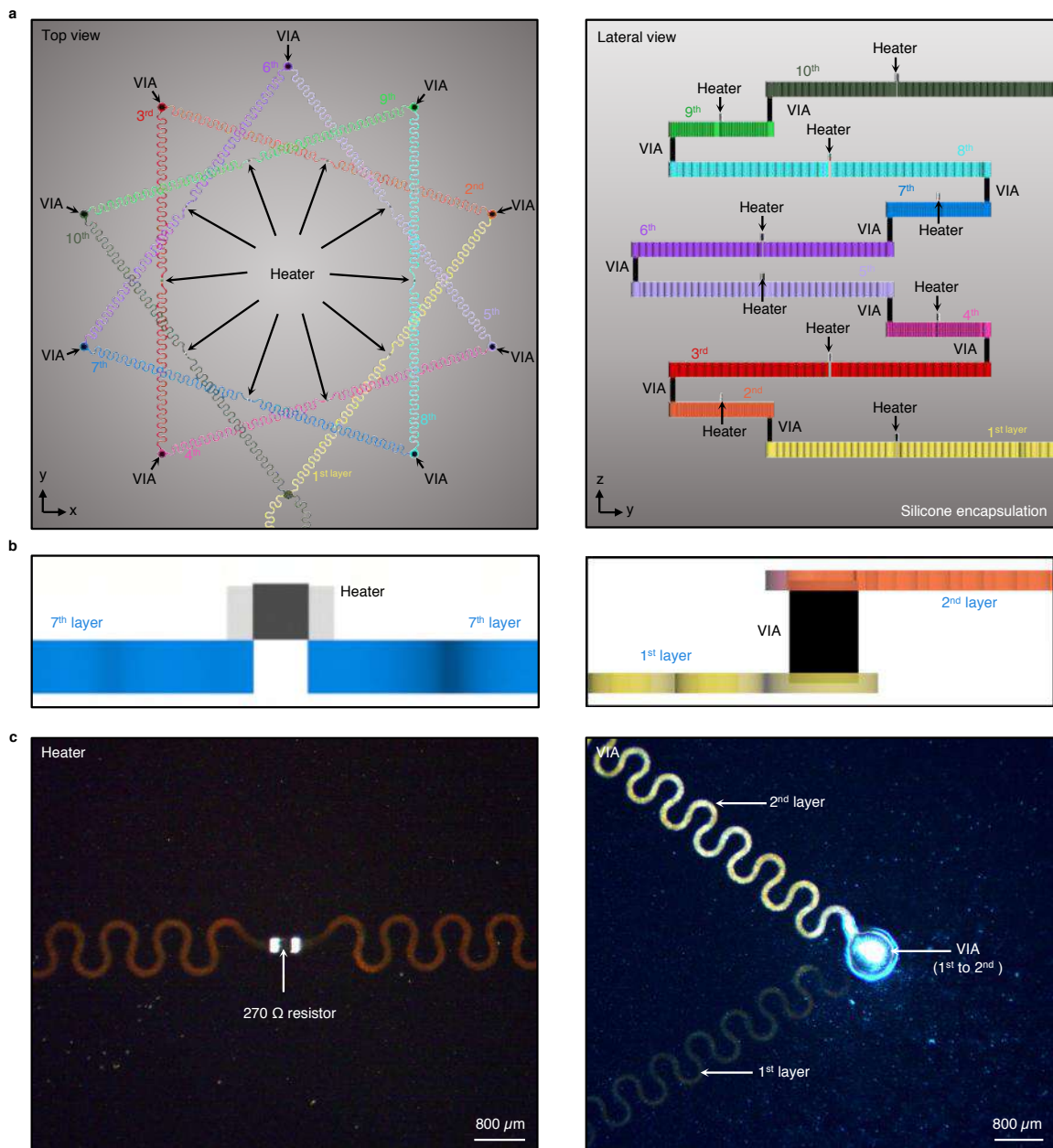
Supplementary Figure 28. Comparison experiments to highlight the influence of flux cleaning and reflow temperature on the welding behavior. **a**, Solid and strong alloy bonding formed by using flux to remove the copper oxide and high reflow temperature (150 °C), which results in good wetting on the contact pad (right panel, the zoomed-in image of the left pin of the resistor). **b**, Poor wetting behavior with high temperature (150 °C), but without flux cleaning. The presence of copper oxide precludes the alloying between tin and copper. Therefore, the solder beads up on the contact pad and the chip is displaced from the contact pad (right panel, the zoomed-in image of the left pin of the resistor). **c**, Incomplete solder paste melting by low reflow temperature (140 °C), resulting in poor bonding and possibly an open circuit (right panel, the zoomed-in image of the left pin of the resistor). The flux can help remove the copper surface oxide, which would otherwise prevent the formation of solid alloys at the interface and thus lead to large contact resistance and weak bonding. Temperature has to be controlled carefully to melt the $\text{Sn}_{42}\text{Bi}_{57.6}\text{Ag}_{0.4}$ paste. If it is too high, it melts the solidified alloys in previous layers. If it is too low, the solder paste does not melt thoroughly.



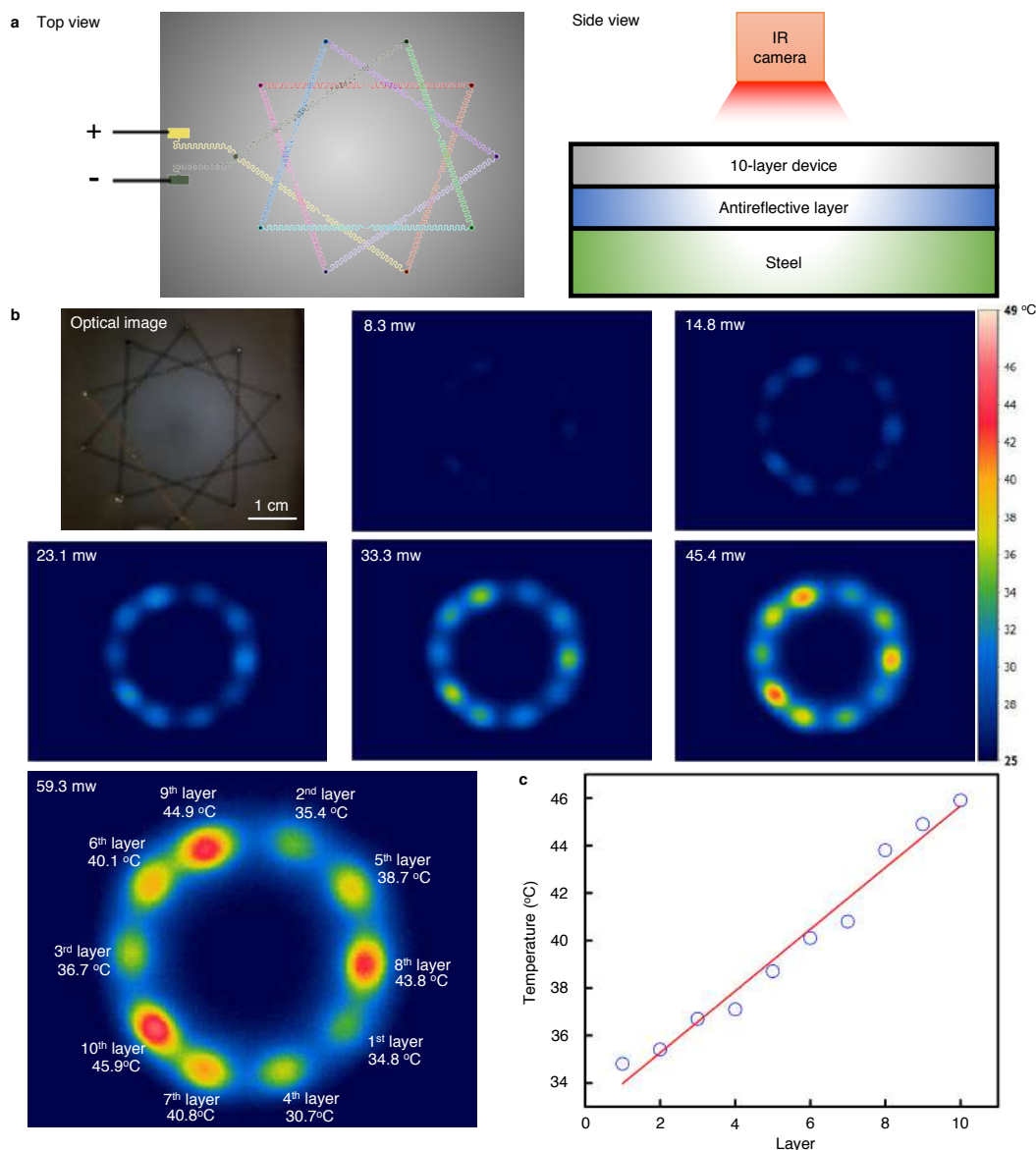
Supplementary Figure 29. Electromechanical testing of the bonding strength between the chip and the interconnect pads. To characterize the robustness of the bonding between rigid chips and interconnects, the sample bonded with high heating temperature (150 °C) and flux treatment was used to test its stretchability. **a**, Resistance measurement with 0% strain. **b**, Continuous resistance measurements from 20% to 120% tensile strain, showing the mechanical robustness of the entire device. **c**, The failure strain of the device is determined to be ~138%. During the entire stretching process, the interface bonding between the rigid chip and interconnect pads was very stable and did not show any evidence of delamination. The serpentine interconnect was broken before the bonding between the rigid chip and interconnect pads fails, when it was stretched to 138%.



Supplementary Figure 30. High electrical performance of the VIAs. The laser ablation and solder paste injection methods form the VIAs through thick (100 μm) and stretchable silicone. The as-formed VIAs were used to connect circuits in different layers, adjacent and non-adjacent. Besides, the VIA material was $\text{Sn}_{42}\text{Bi}_{57.6}\text{Ag}_{0.4}$ metal alloy, which had very high conductivity. Furthermore, when heated, a layer of Cu-Sn alloy will form between the VIA and the copper interconnects (for both top and bottom copper wires), which built strong bonding between the VIAs and the interconnects in different layers and made the VIAs very stable. **a**, I-V curves of the VIA before and after stretching (100% strain). The straight line means it is an ohmic contact between the VIA and copper interconnects. The resistance of the VIAs is only round 68.7 $\text{m}\Omega$. The overlapped two lines indicate the resistance didn't change noticeably with the strain from 0% to 100%. **b**, VIA impedance spectroscopy under free standing and 100% tensile strain states. The impedance increases with frequency, because of the skin effect for r.f. transmission wires and the increased inductive reactance value at higher frequencies (inductive reactance $X_L = 2\pi fL$, where f is the frequency and L is the wire inductance). For our VIA, the impedance slightly increased when the frequency was higher than 1 MHz, and dramatically increased when the frequency was above 50 MHz.



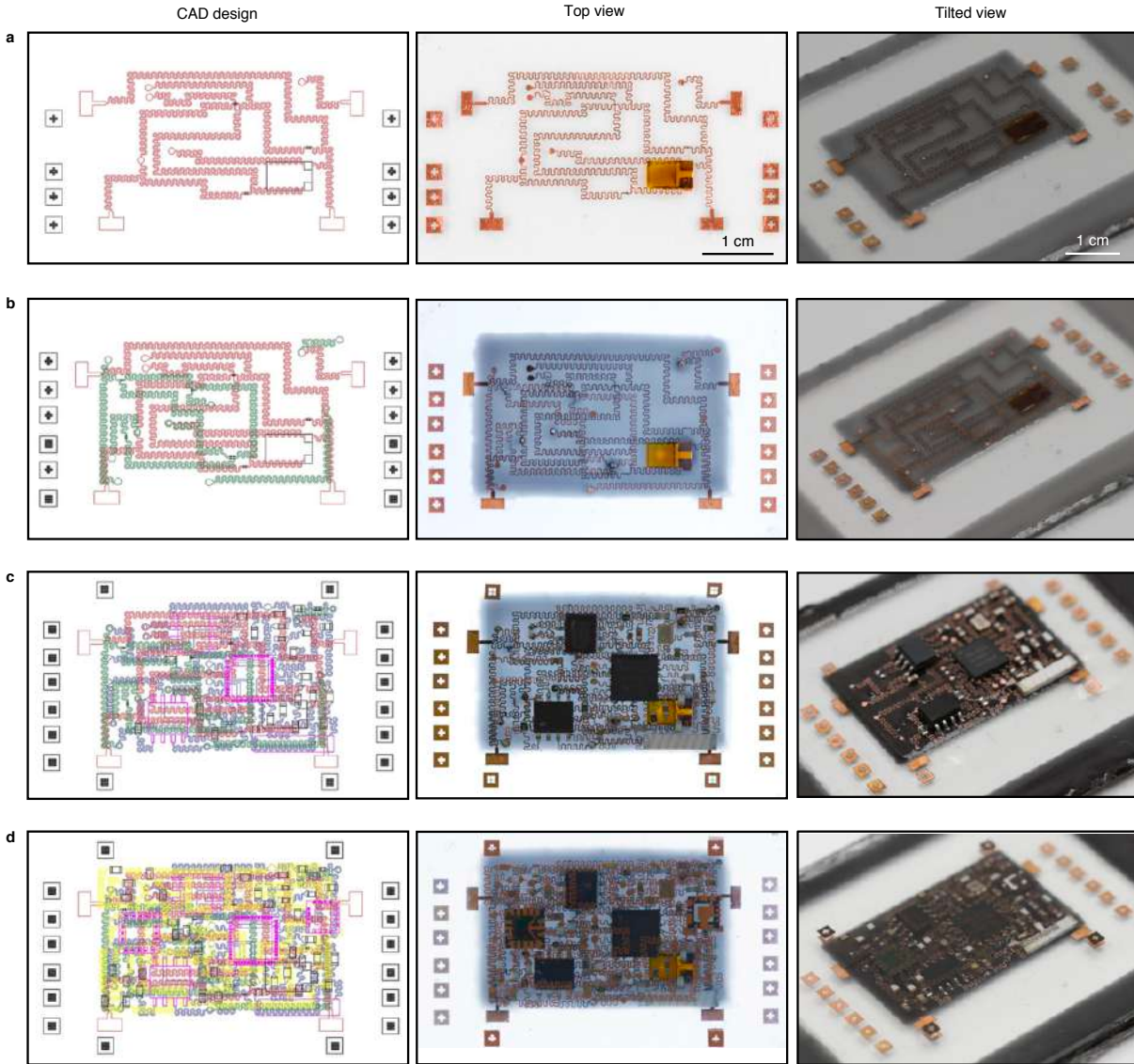
Supplementary Figure 31. Illustration of the 10-layer stretchable decagram device structure. **a**, Schematic top view (left) and cross sectional view (right) to show the multilayered device structure. The device has 10 layers, with a heater in each layer and a VIA vertically connecting the adjacent layers in series. The entire device is fully encapsulated by silicone. **(b)** Detailed schematics and **(c)** optical images of the heater (left) and VIA (right).



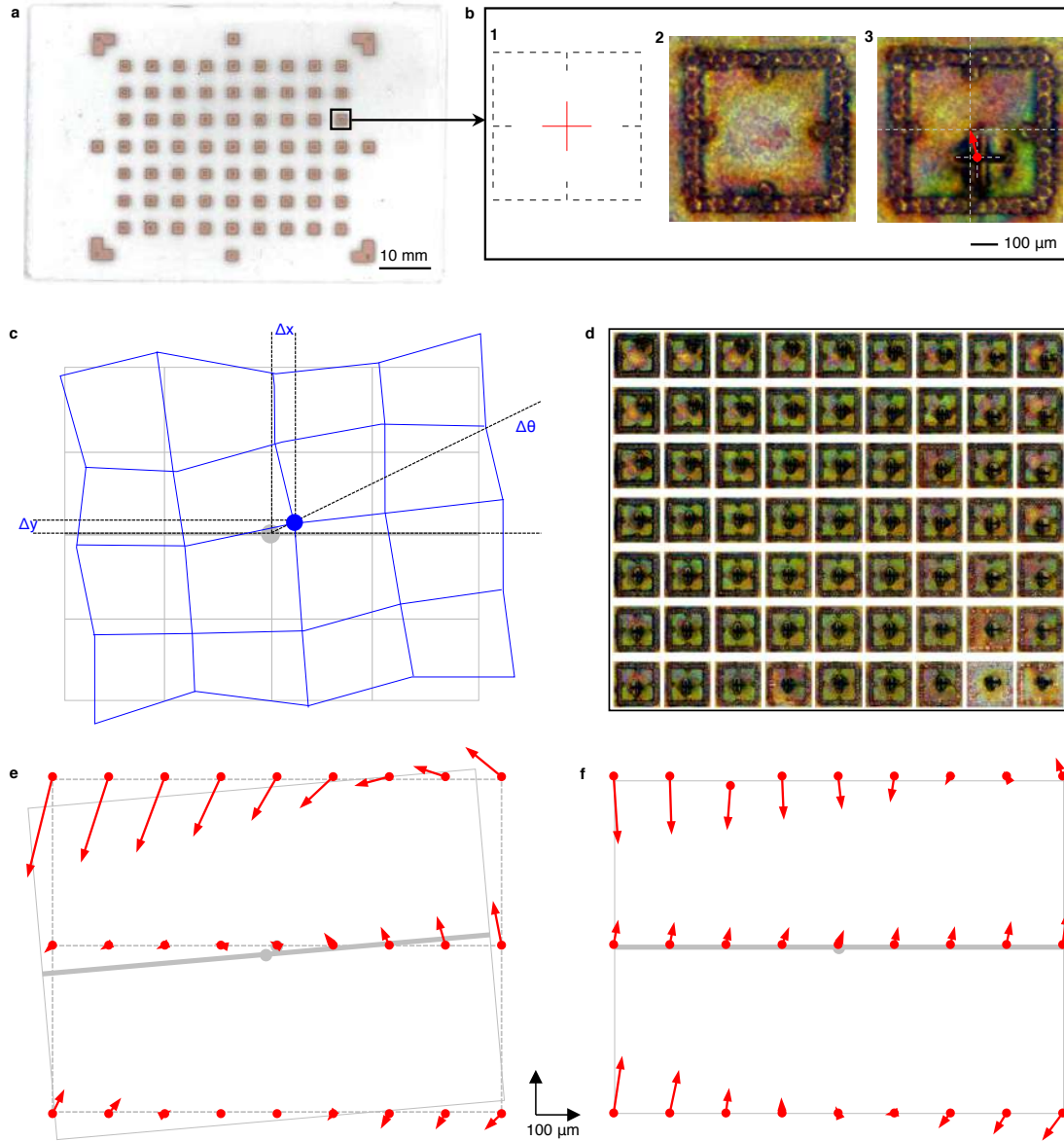
Supplementary Figure 32. Thermal imaging setup for the 10-layer stretchable decagram device. **a**, Schematic top and cross-sectional views of the setup. An external DC supply is used to drive the device. An IR camera (Therm-App® TH, resolution 384x288 pixels, sensitivity < 0.07 K) is used to image the temperature distribution on the device surface. A steel board at the bottom is used as the heat sink to increase the thermal dissipation of the device. An antireflective layer (a white paper or black plastic) is used to decrease the IR reflection from the environment. **b**, Thermal images of the device with different heating power. **c**, Temperature summary of heaters in different layers.

Layer by layer fabrication

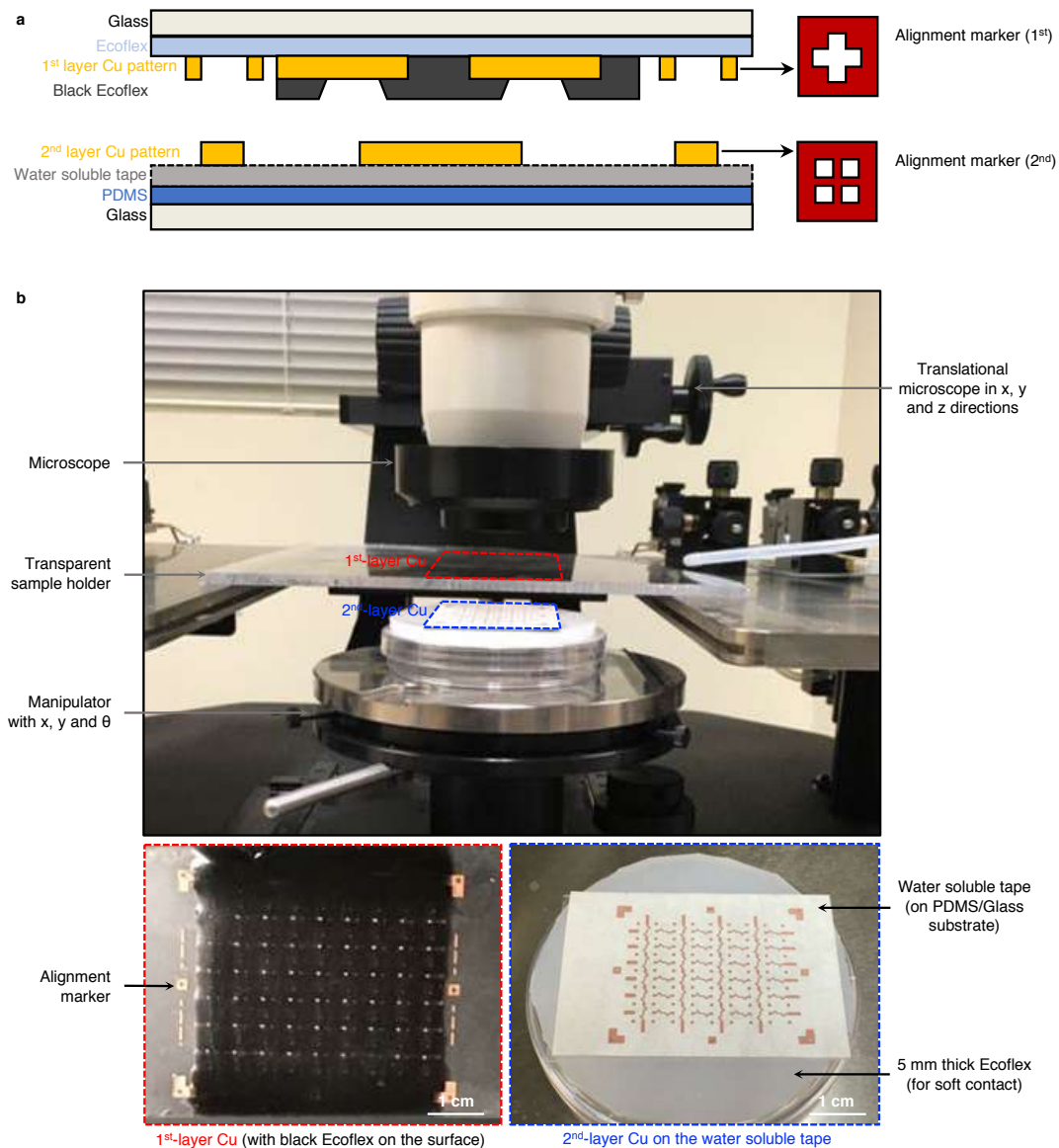
✱ Alignment markers



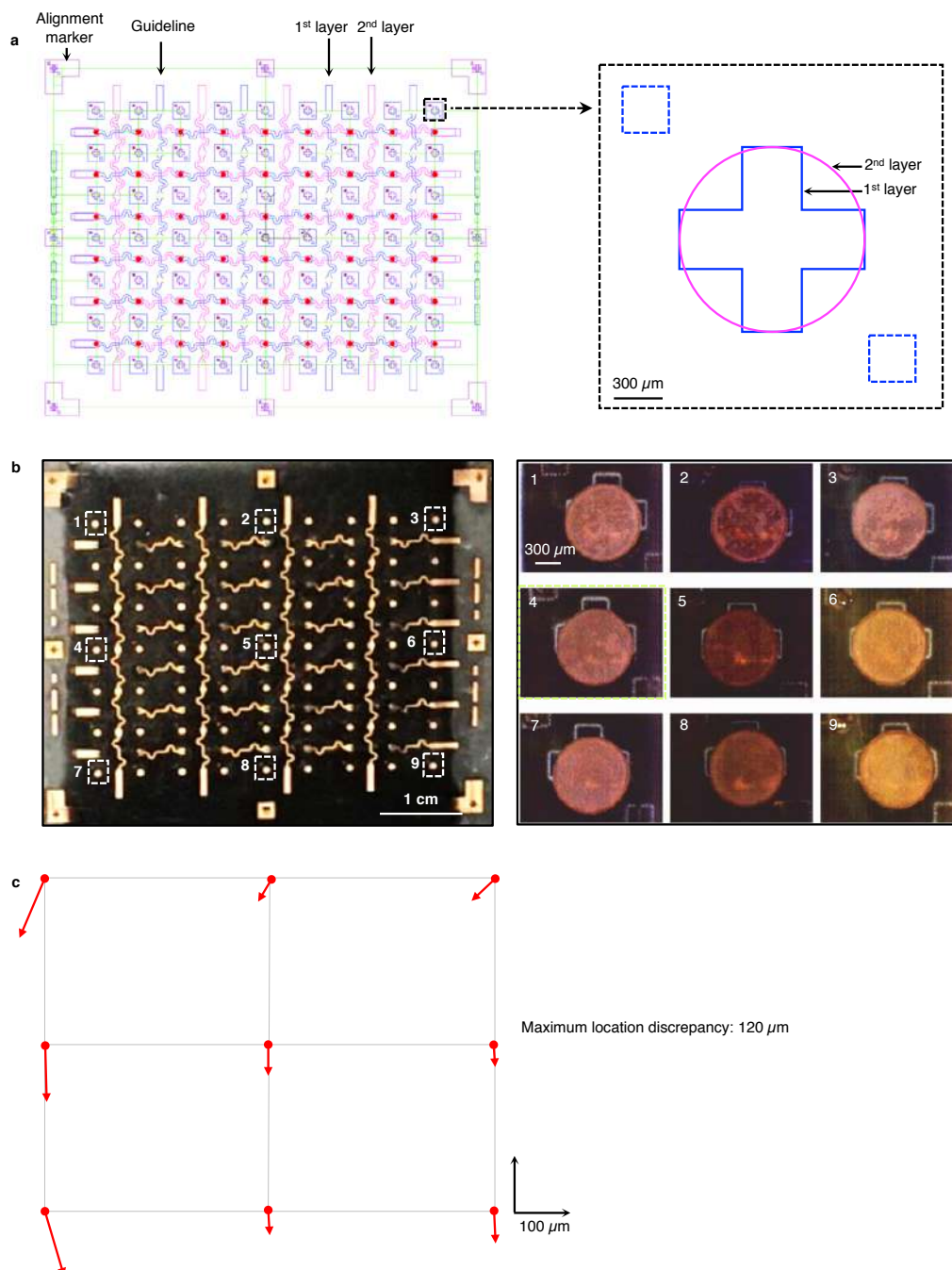
Supplementary Figure 33. Layer by layer fabrication process for the four-layer stretchable system. The images show the fabrication process from the (a) 1st layer to the (d) 4th layer, in CAD design (first column), device top view (second column), and device titled view (third column).



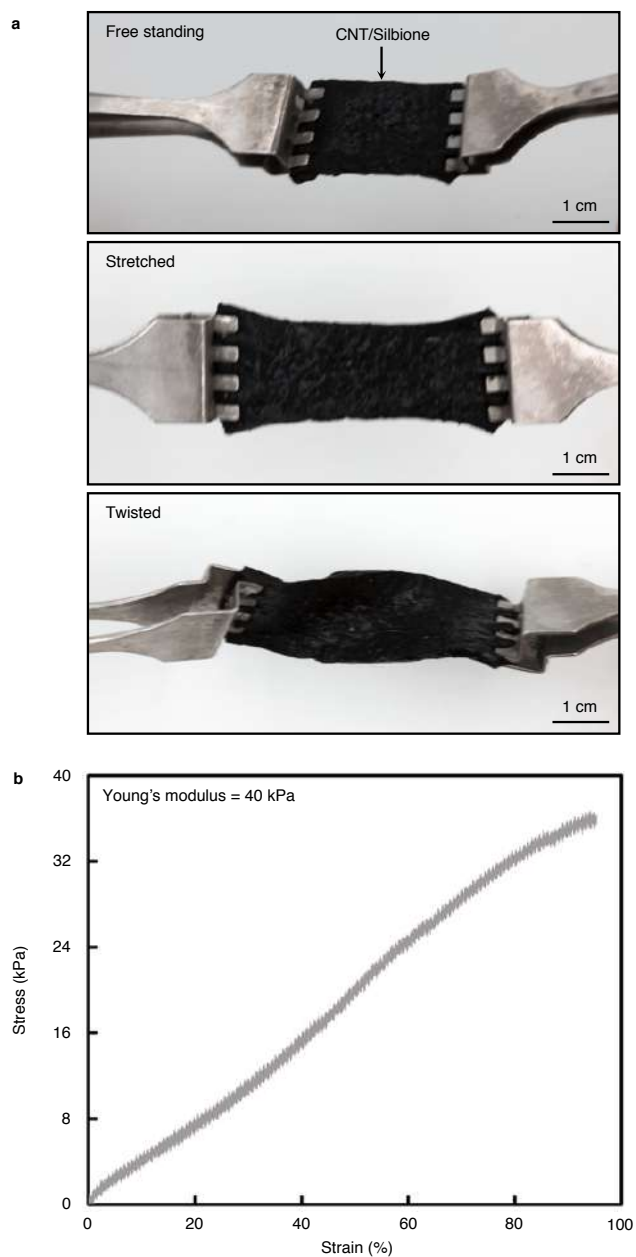
Supplementary Figure 34. Evaluation of interconnection distortion during the transfer printing process. **a**, Overview of a test sample. **b**, (1) Alignment marker design, the black line for 1st ablation (before transfer) and the red line for 2nd ablation (after transfer); Examples of actual laser marker (2) before transfer and (3) after transfer. Red vector shows the location discrepancy between the 1st and the 2nd ablations. **c**, Schematic laser alignment error (with horizontal shift Δx , vertical shift Δy , and rotation $\Delta\theta$) and sample distortion after transfer. **d**, A compiled photo of alignment markers at each location. **e**, The arrows show the total misalignment between the 1st and 2nd laser ablation patterns, which include both the laser alignment error and transfer distortion. By calculation, the location discrepancies and laser alignment error are Δx , Δy , $\Delta\theta$: -29 μm , -24 μm , 0.14°, respectively. **f**, Transfer distortion, regardless of the laser alignment. (Maximum distortion: 152 μm , Average distortion in rms: 14 μm).



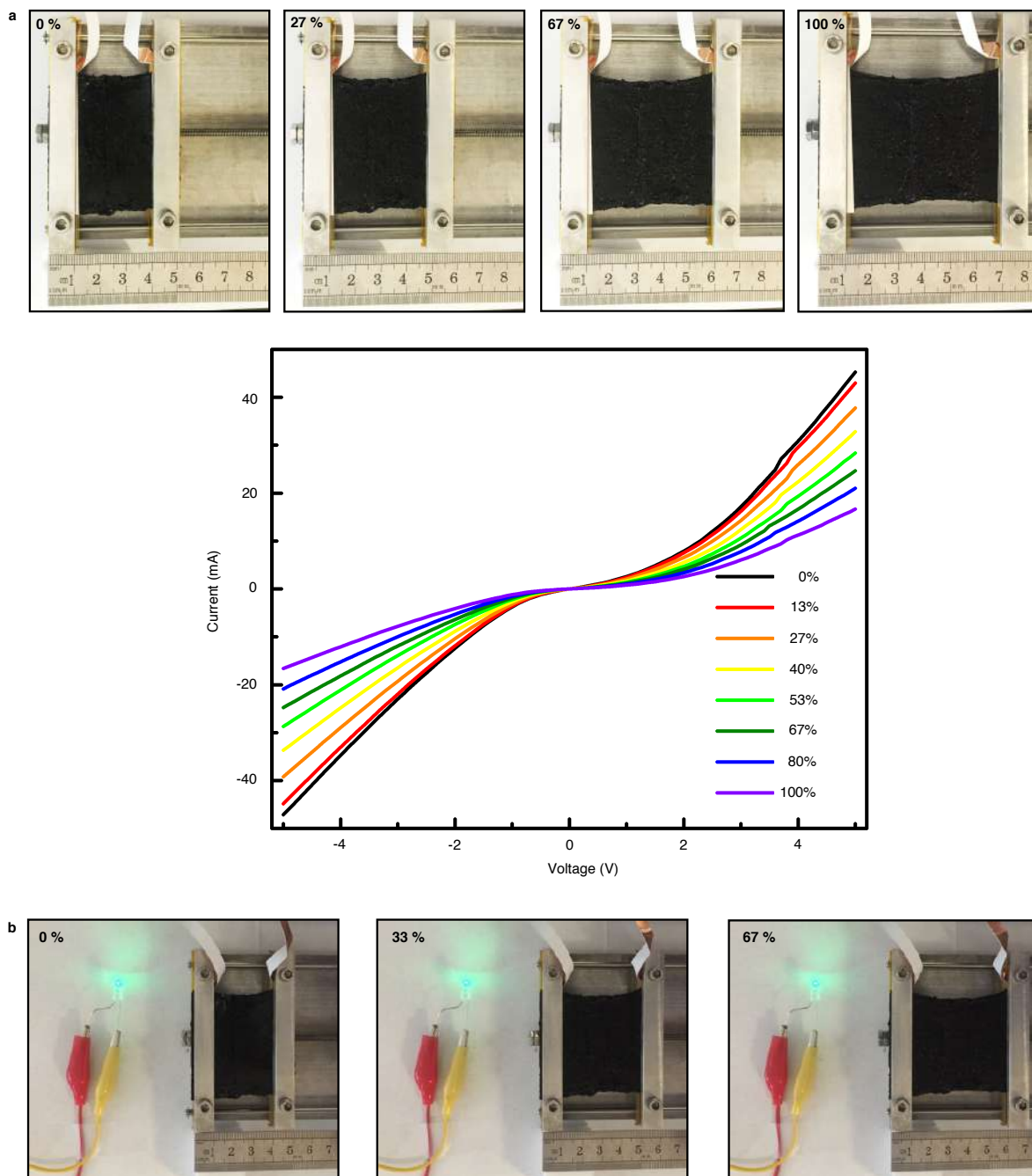
Supplementary Figure 35. Setup for aligned transfer printing. The multilayered device is fabricated layer by layer. The subsequent layer should be well-aligned with the existing layers for VIA connections. **a**, Schematic illustration of the alignment. Every layer has the marker for alignment. The layer to be transferred is on water soluble tape and fixed by PDMS temporarily. **b**, The alignment system, composed of a microscope and a mechanical stage. The first layer is fixed on a transparent holder and the second layer is placed on a 5 mm thick Ecoflex. The Ecoflex is used as the buffer for soft contact with the first layer, which will protect the sample from excessive pressure.



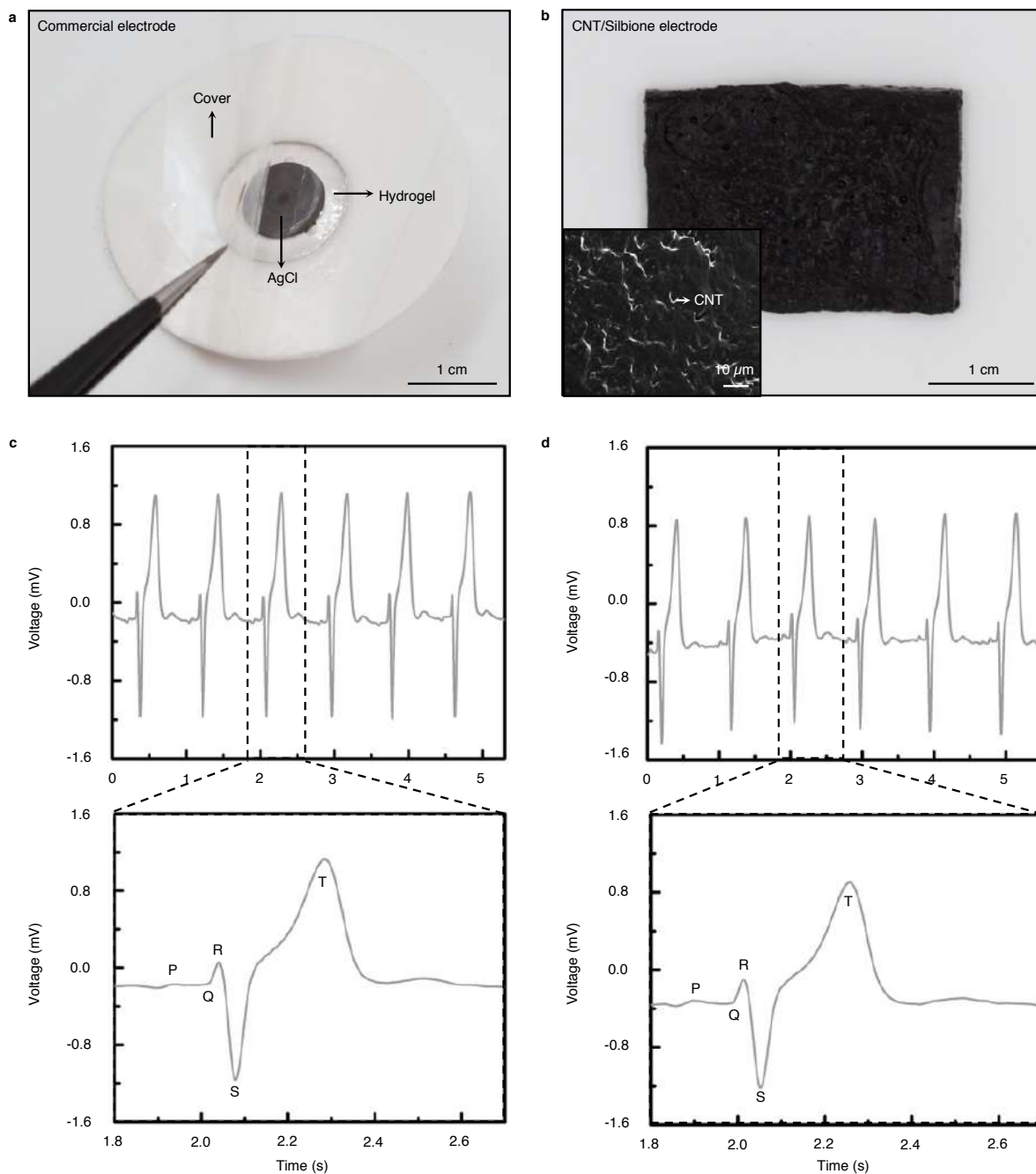
Supplementary Figure 36. Error evaluation of aligned transfer printing. **a**, Two-layer pattern design for the transfer error evaluation. The blue layout is the first layer and the carmine layout is the second layer. Shown on the right is the ideal alignment of the markers. **b**, The integrated two-layer device after transfer printing. Shown on the right is the marker distribution on the device. After checking the marker shift, the aligned transfer printing error is evaluated, as shown in (c). The max error is $\sim 120 \mu\text{m}$.



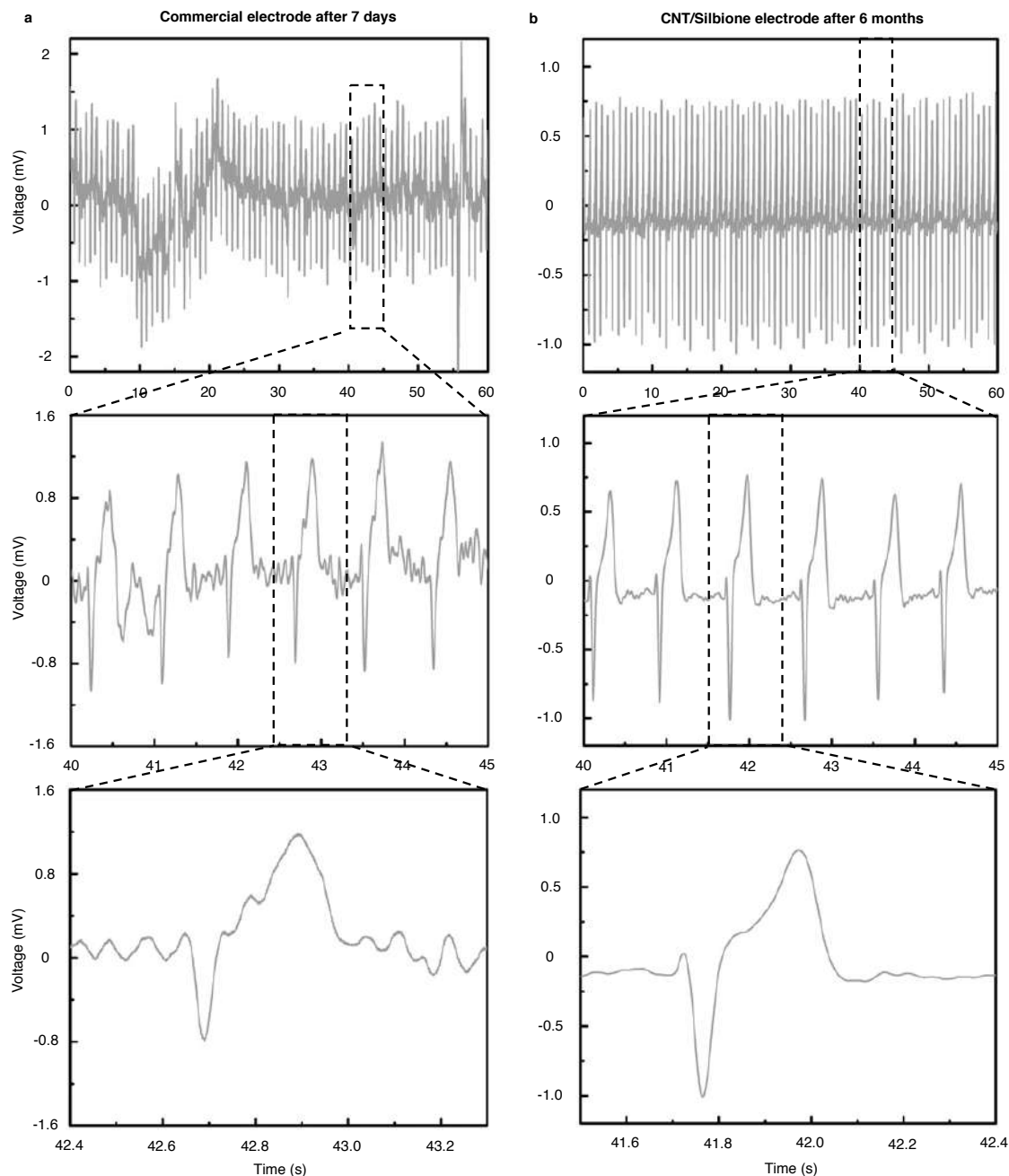
Supplementary Figure 37. Mechanical properties of the soft CNT/Silbione EP sensors. a, Optical images showing the sensor can be stretched and twisted. **b,** Stress vs. strain relationship of the EP sensor indicating its ultra-low Young's modulus of 40 kPa.



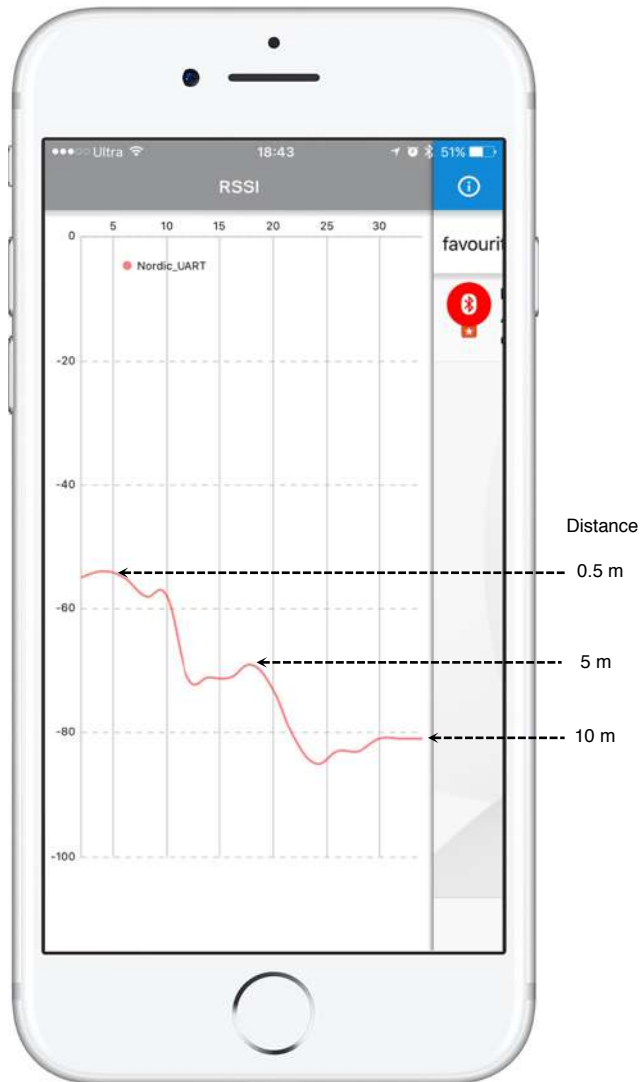
Supplementary Figure 38. Electrical properties of the soft CNT/Silbione EP sensors. a, Optical images of the sensor (with dimensions $\sim 30 \times 56 \times 1$ (L \times W \times T) mm³) under different levels of uniaxial strain and associated I-V curves. **b,** The sensor itself can be used as a stretchable electrical connection to light up a LED at 3 V.



Supplementary Figure 39. ECG signals acquired with fresh commercial electrodes and homemade soft CNT/Silbione electrodes. The similar results of these two types of electrodes with high signal-to-noise-ratios (SNR) and the well defined P, Q, R, S, and T waveforms indicate the excellent sensing capability of the soft CNT/Silbione electrodes. Optical images of (a) the commercial AgCl/Ag-hydrogel electrode and (b) soft CNT/Silbione electrode, respectively. The inset of (b) shows the magnified CNT/Silbione composites in SEM. ECG signals acquired from the chest with (c) the commercial and (d) CNT/Silbione electrodes, respectively.



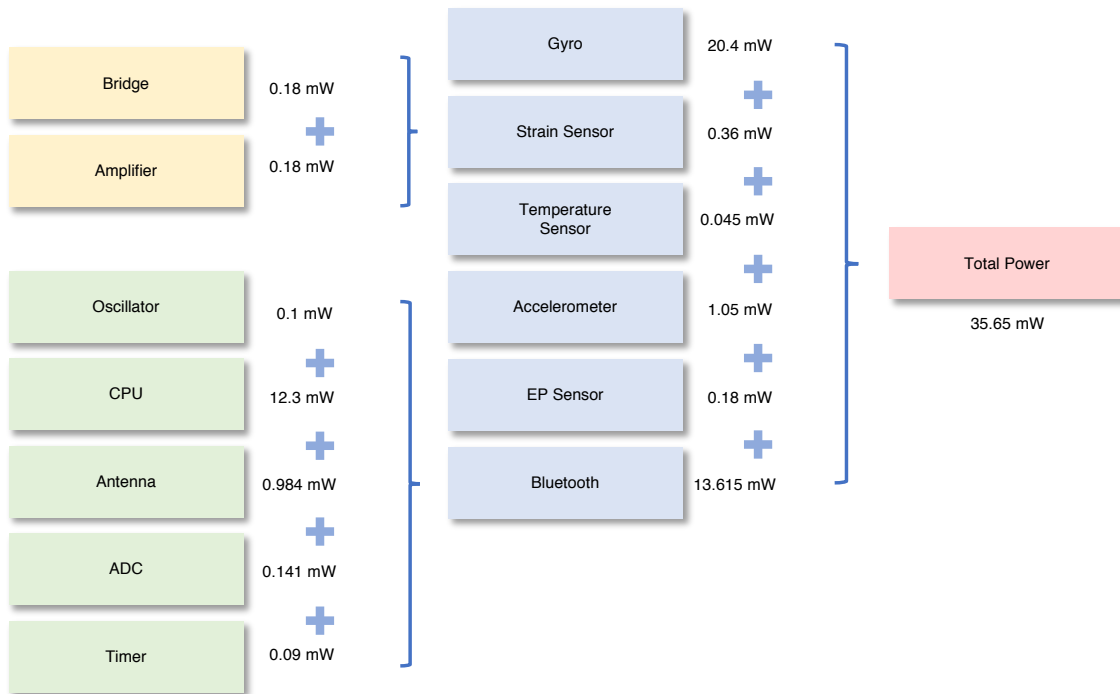
Supplementary Figure 40. Durability comparison between the commercial electrode and our soft CNT/Silbione electrode. **a**, The ECG signals acquired by the commercial electrode, which has been exposed in air for 7 days with the plastic covers removed. The fluctuating and noisy signals are due to the hydrogel that is dried out when exposed in air, which increases the impedance between the electrode and the skin. **b**, The stable ECG signals acquired by the CNT/Silbione electrode, which has been exposed to air for around 6 months, showing the electrode's superb durability.



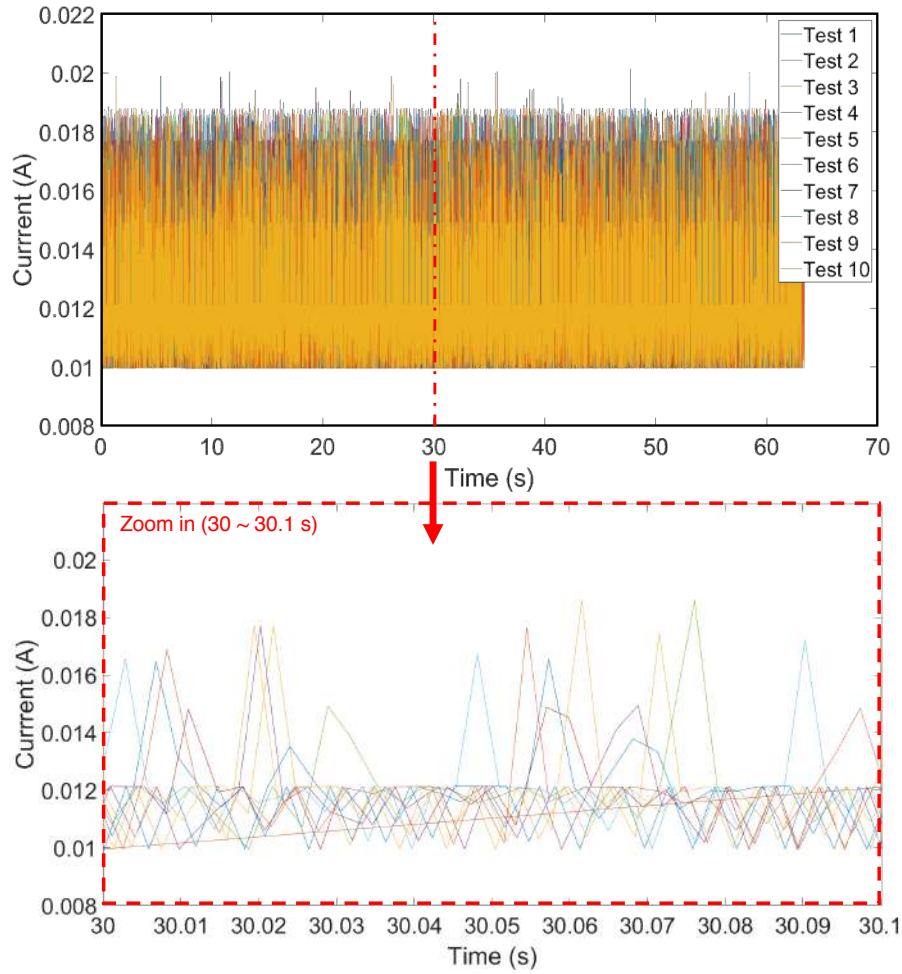
Hardware: iPhone 6 Plus; Software: NRF Connect

Supplementary Figure 41. Test of the Bluetooth signal strength from the multilayered stretchable device by the received-signal-strength-indicator (RSSI). The measurement hardware is a smartphone (iPhone 6 Plus with software NRF Connect).

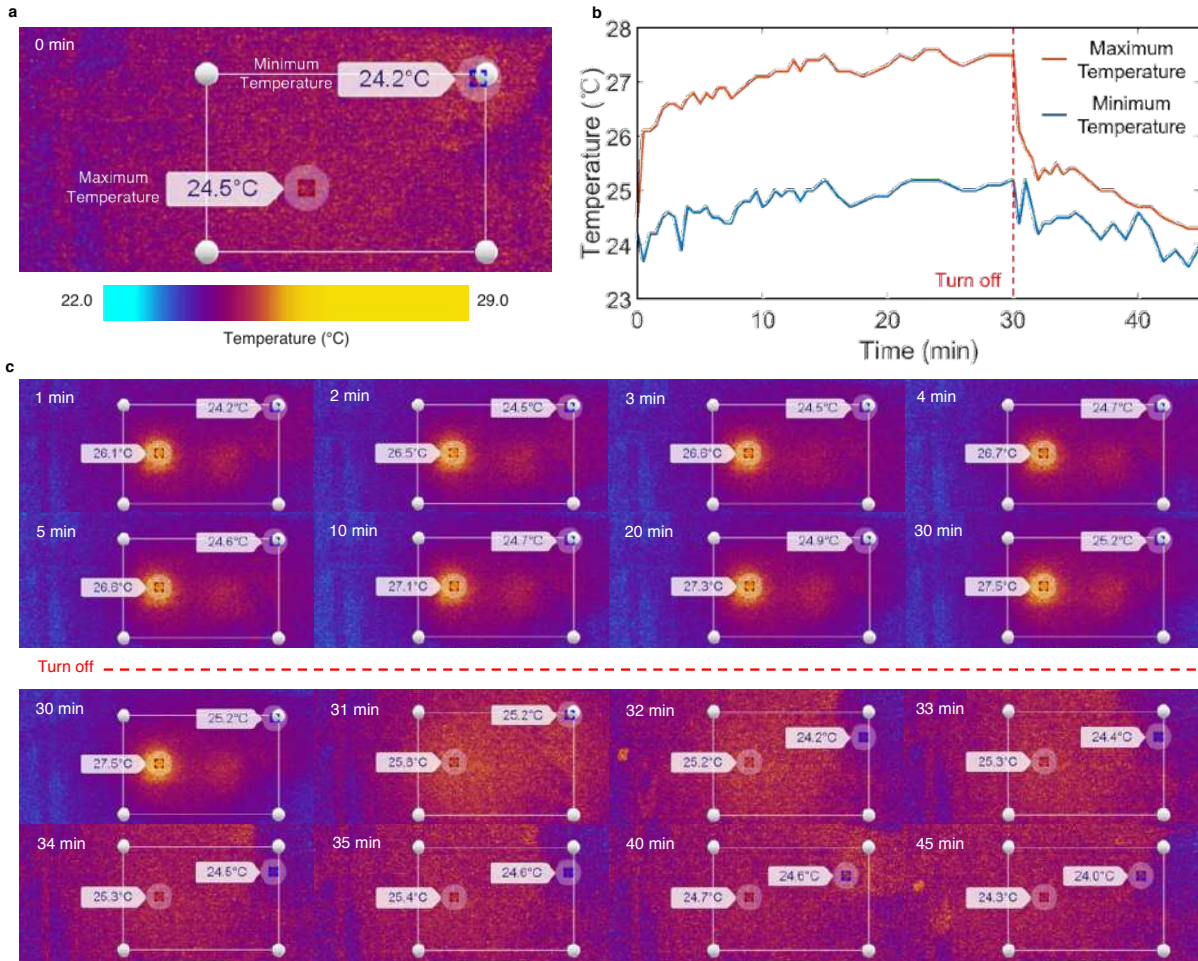
Theoretical Power Calculation



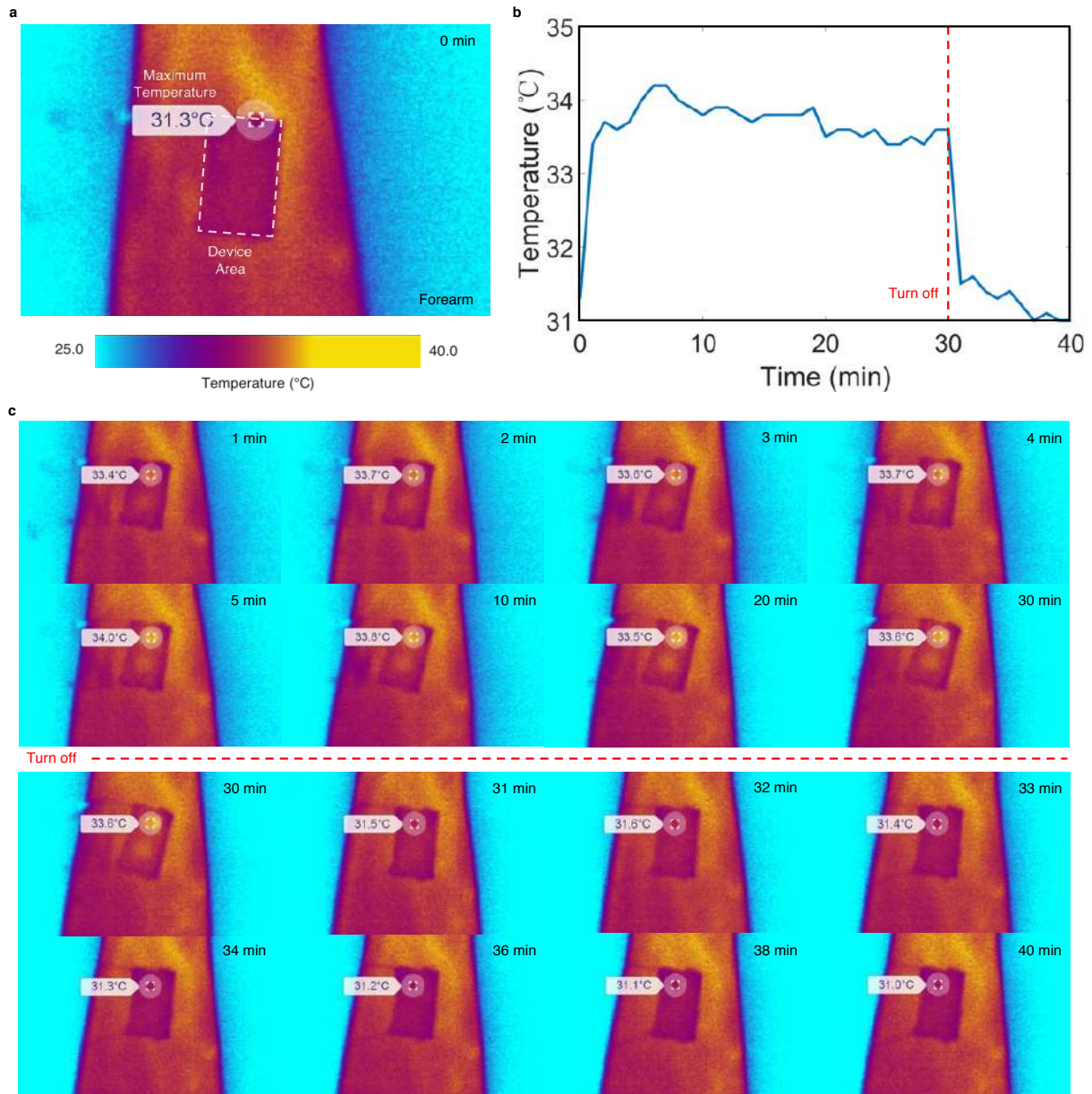
Supplementary Figure 42. Theoretical power calculation workflow and results. The total power dissipation is composed of six parts, including the gyro, strain sensor, temperature sensor, accelerometer, EP sensor, and Bluetooth. Only one main chip is used for these four parts: gyro, temperature sensor, accelerometer, and EP sensor part. Thus, the power consumption of each one of these parts can be calculated from the corresponding chips. The strain sensor, however, includes two parts, a bridge and an amplifier. Thus, its power consumption should be the sum of those two parts. Similarly, the power consumption of Bluetooth should be the sum of the six component chips. All the data are calculated from the official datasheet of the corresponding chips. The calculated total power is 35.65 mW (theoretical value).



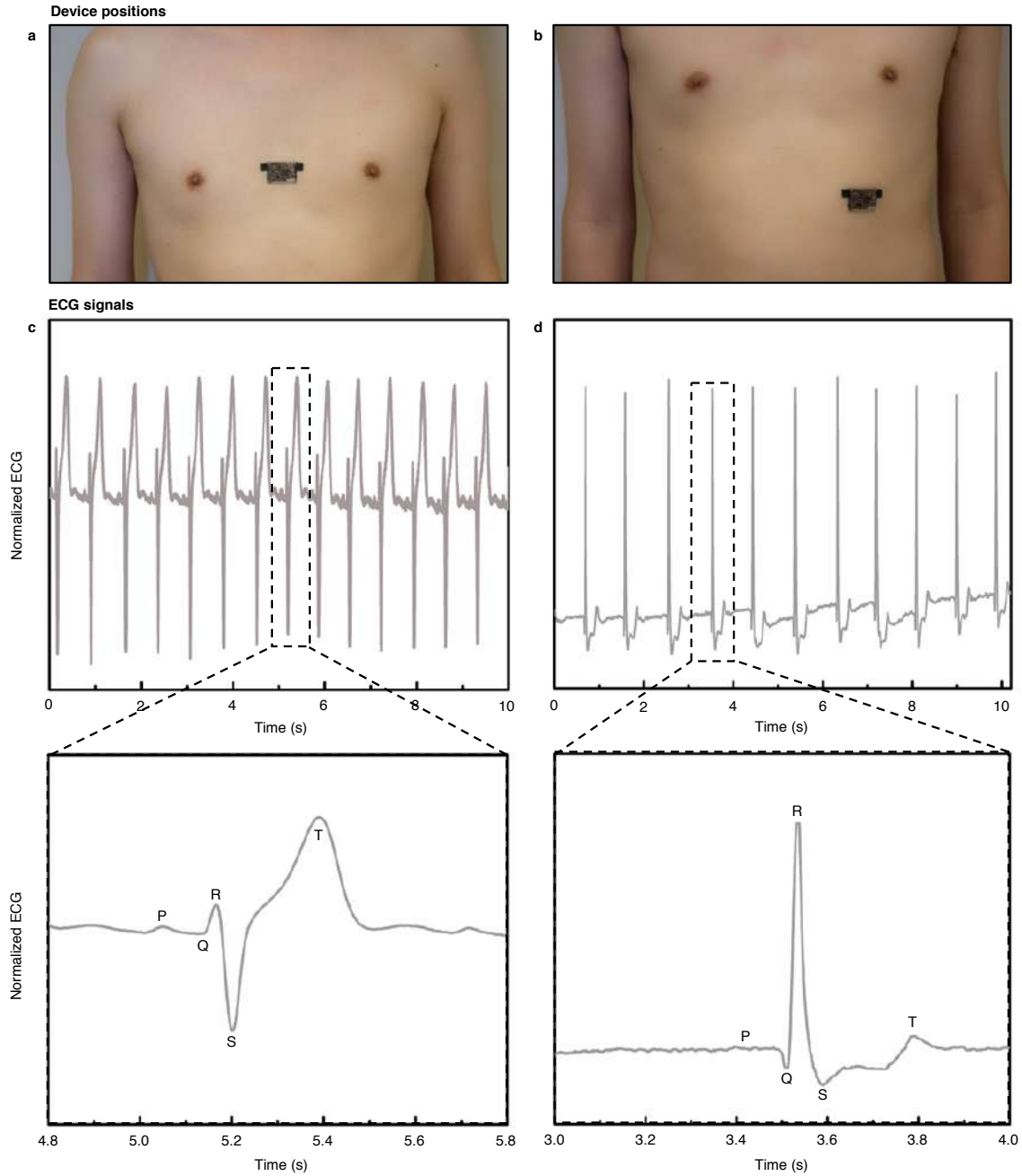
Supplementary Figure 43. Dynamic current consumption for the working device at 3 V DC supply. The current flow of the entire stretchable device was measured with a source meter (Keysight B2901). A DC voltage of 3 V was applied to drive the device. Data from 30~30.1 s is zoomed in to show the dynamic current consumption in each test. The average power was calculated by: $\bar{P} = \frac{1}{T} V \int_0^T I dt$, where \bar{P} is the average power, V is the device working DC voltage, I is the working current, and T is the total time of one test. Ten tests were carried out to calculate the average power dissipation, which was around 35.62 mW (experimental value), which is very similar to our theoretical value 35.65 mW (Supplementary Fig. 42).



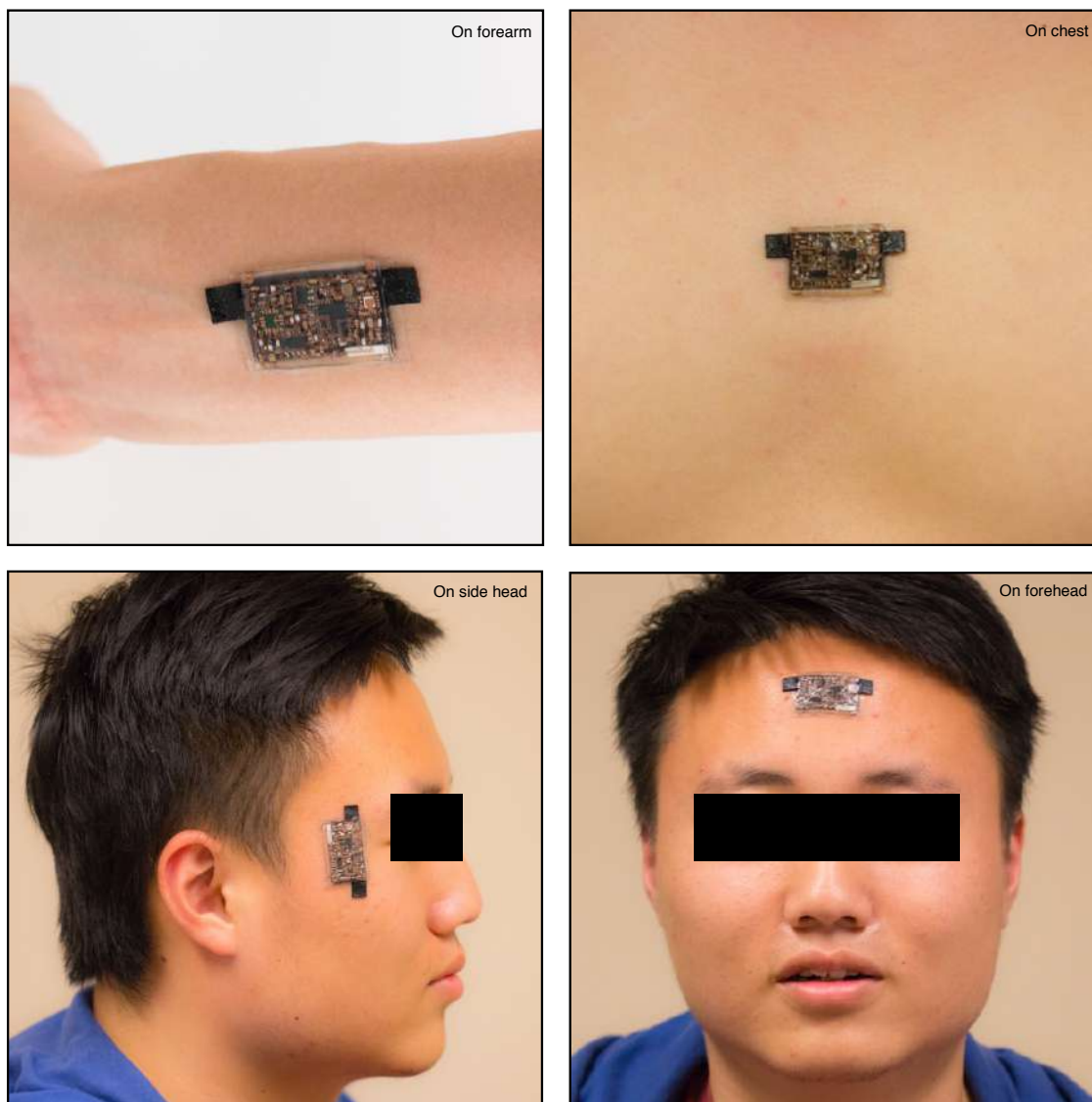
Supplementary Figure 44. Temperature variation of the device when working and resting (measured by an IR camera, on the bench at room temperature 24 °C). **a**, Temperature profile of the device right after being turned on. The rectangular area represents the actual device. Points with maximum and minimum temperature in the area are labeled. **b**, Maximum and minimum temperature variations of the device after turning on at 0 min and turning off at 30 min; **c**, IR images of the device after turning on 1~45 min. The device is turned off at 30 min. The highest temperature is located on the gyro chip, which has the biggest power dissipation. The temperature of the gyro chip increases 2.7 °C in the first 10 mins and is stable at 27.2 °C. When the system is shut down, the device temperature recovers to the room temperature in ~10 mins.



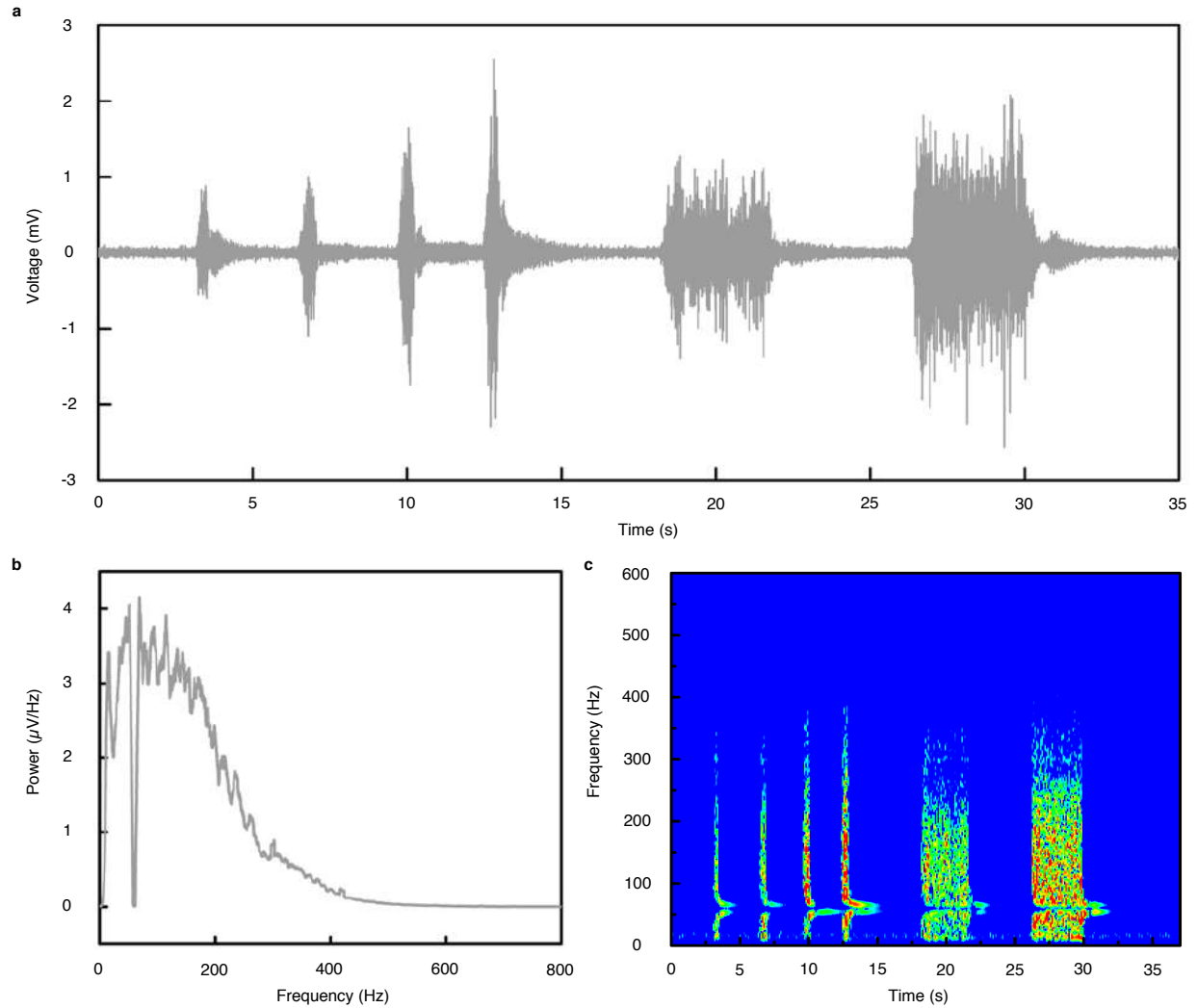
Supplementary Figure 45. Temperature variation of the device when working and resting (measured by an IR camera, on human forearm). **a**, Temperature profile of the device right after being turned on. The rectangular area represents the actual device. Points with maximum and minimum temperature in the area are labeled. **b**, Maximum temperature variations of the device after turning on at 0 min and turning off at 30 min; **c**, IR images of the device after turning on 1~40 min. The device is turned off at 30 min. The highest temperature of the system increases to 33.6 °C in 5 mins, only 2.3 °C higher than resting state 31.3 °C, which is acceptable for human skin.



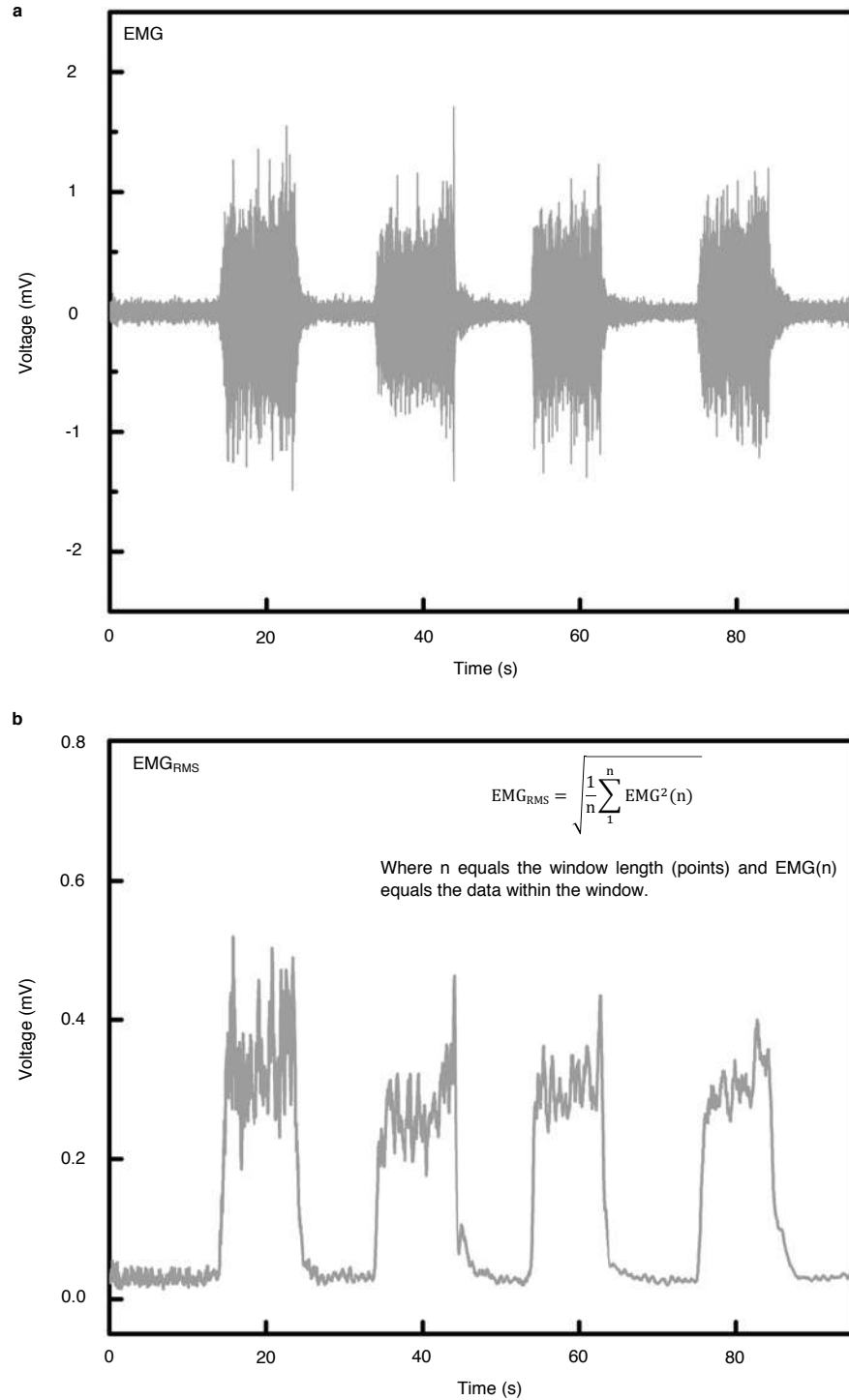
Supplementary Figure 46. ECG signals acquired from different positions of the human body. Images showing the device attached on **(a)** the chest and **(b)** the abdominal area. The power source for these measurements is omitted in the images for clarity purposes. Corresponding ECG signals acquired from **(c)** the chest and **(d)** the abdominal area, respectively.



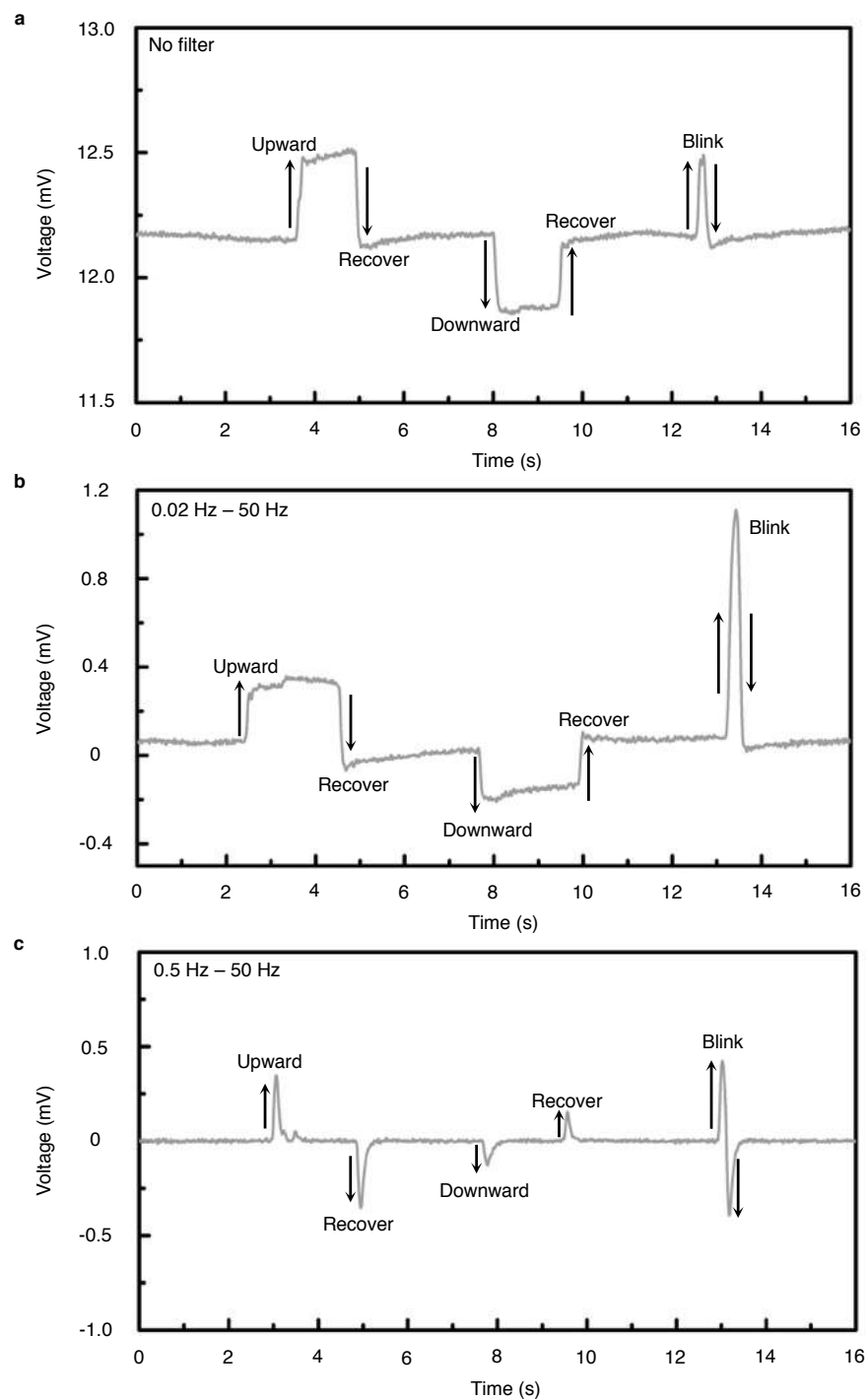
Supplementary Figure 47. Optical images showing the positions where the EP signals are acquired: on the forearm for EMG, on the chest for ECG, on the side head for EOG, and on the forehead for EEG. The power source for these measurements is omitted in the images for clarity purposes.



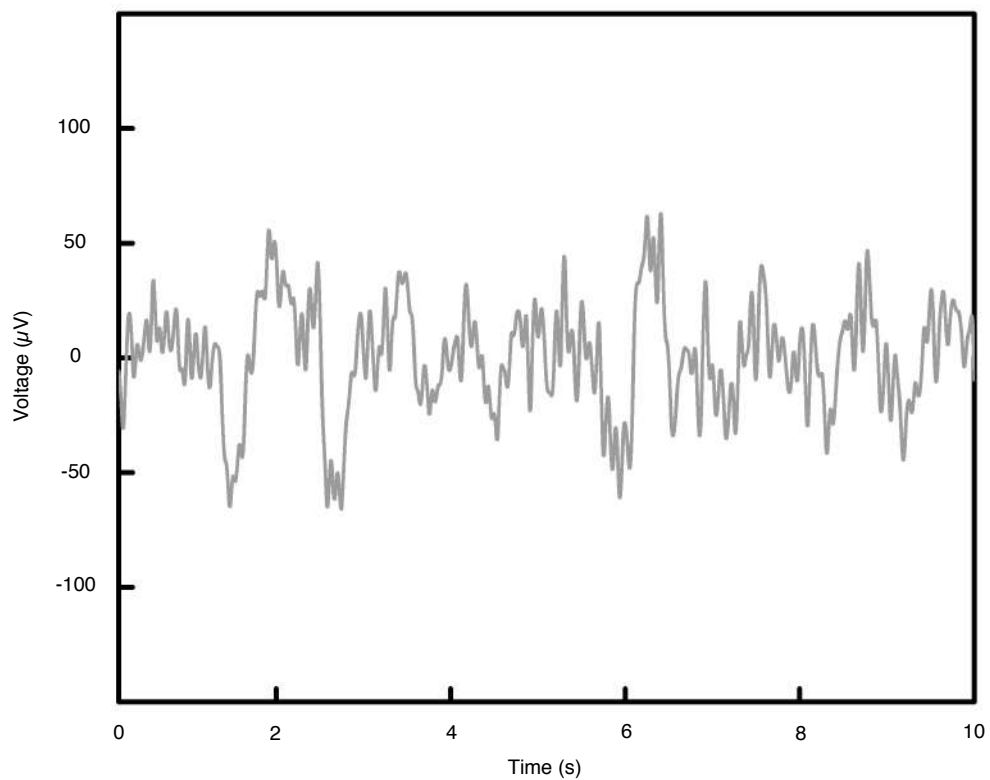
Supplementary Figure 48. EMG signals acquired from the forearm to show the signal frequency spectrum. a, EMG time-domain signals with 60 Hz notch filter. **b,** EMG signals from Fast Fourier Transform (FFT) analysis, showing the frequency distribution of the signals. The dip at around 60 Hz is from the notch filter. **c,** EMG power spectral density analyzed by Short-Time Fourier Transform (STFT), showing the time-domain EMG power distribution.



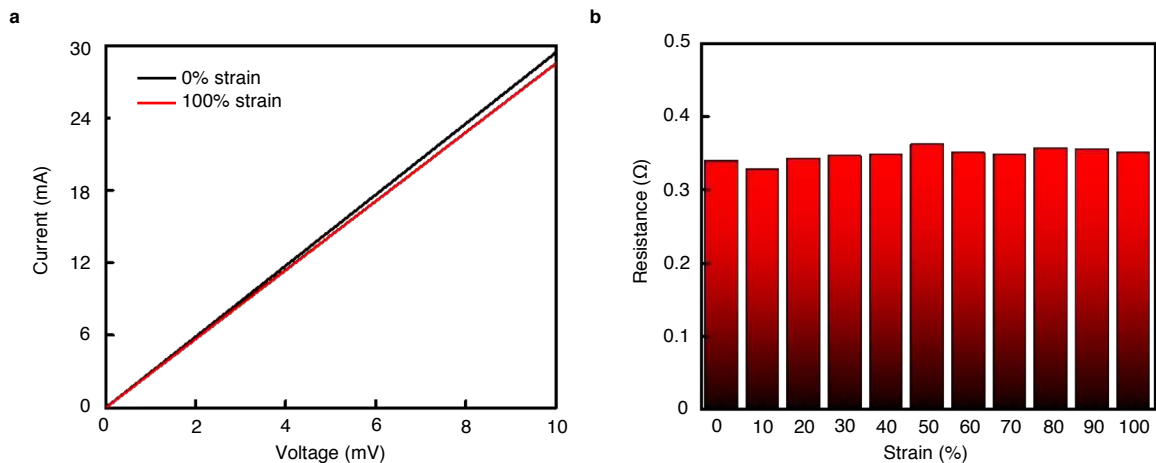
Supplementary Figure 49. EMG power analysis with root-mean-square envelope. a, The raw data of EMG signals acquired from the forearm with periodic clenching. **b,** Amplitude analysis with root-mean-square EMG envelope to quantify the signals.



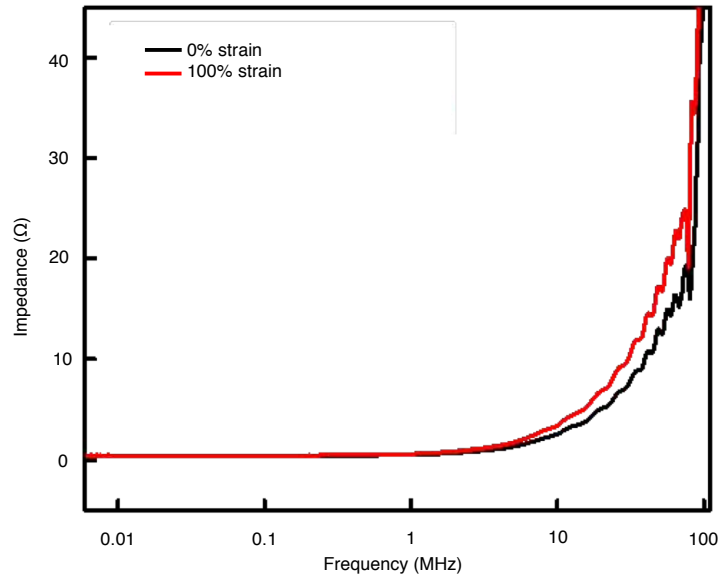
Supplementary Figure 50. EOG signals processed with different filters. **a**, EOG signals without a filter. There is a bias voltage of ~ 12.2 mV in the baseline, which is due to the charge accumulation between the two EP sensors. EOG signals with band-pass filters of **(b)** 0.02 Hz – 50 Hz and **(c)** 0.5 Hz – 50 Hz. The low frequency signal bias is removed. In **(c)** the EOG signals are also largely distorted from the original one. For our study, the filter of 0.02 Hz – 50 Hz is chosen.



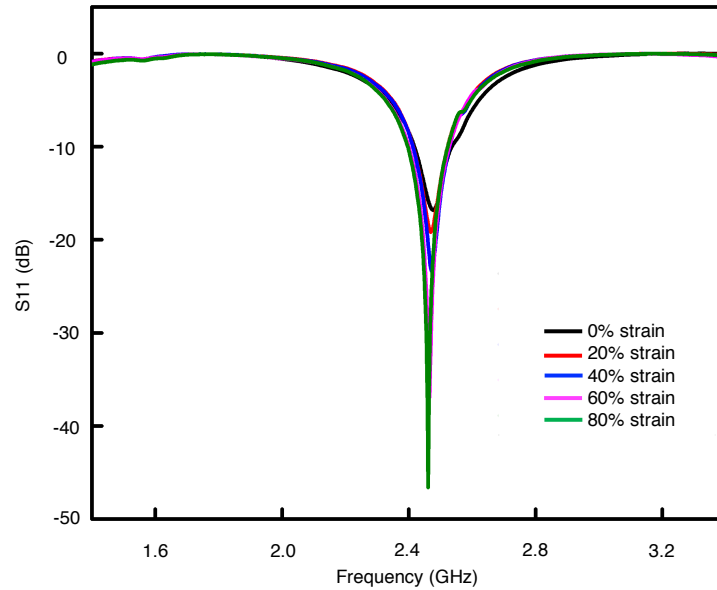
Supplementary Figure 51. EEG signals in the voltage-time domain. The signal noise level is around 15 μV with a signal/noise ratio ~ 7 for this measurement.



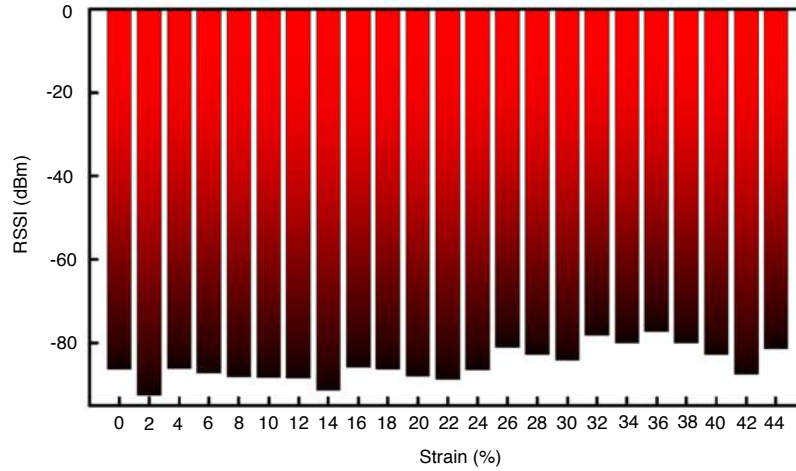
Supplementary Figure 52. Quantitative resistance evaluation of the interconnect under strain. **a**, I-V curves of the copper interconnect (width: 0.15 mm; pad-to-pad length: 5.68 mm; thickness: 0.02 mm) tested under 0% and 100% strain. From the slope of the straight line, the resistance of the copper interconnect can be calculated to be 0.34 Ω (0%) and 0.35 Ω (100%). **b**, With strain from 0% to 100% (increment 10%), the interconnect resistance was measured. The resistance varied in a narrow band from 0.33 Ω to 0.36 Ω , which indicates stable electrical properties of the interconnects.



Supplementary Figure 53. Interconnect impedance spectroscopy of serpentine under free standing and 100% strain states. To evaluate the serpentine interconnect performance at high frequencies, the 5.75 mm pad-to-pad length serpentine's (width: 0.15 mm; thickness: 0.02 mm) impedance spectroscopy under 0% and 100% strain states was measured from 6 KHz to 100 MHz. Two conclusions can be drawn from the data. First, the interconnect impedance increases with increasing frequency, especially when the frequency is higher than 10 MHz due to the skin effect and increased inductive reactance at higher frequencies. Second, with interconnect strain increased from 0% to 100%, the impedance increases 7% with the frequency less than 1 MHz and increases up to around 34% especially in the high frequency range (larger than 10 MHz), which owns to the larger wire inductance due to the interconnect deformation.

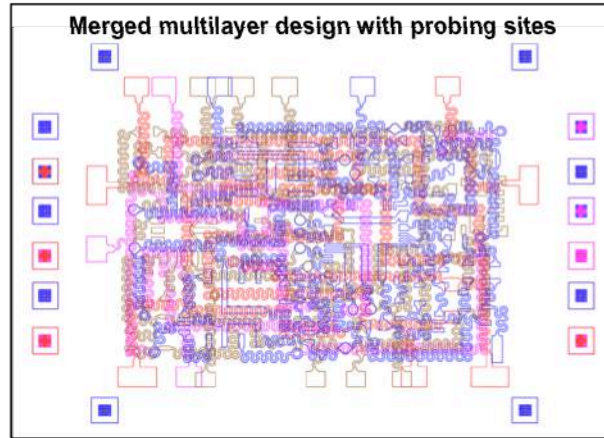


Supplementary Figure 54. S11 test of a 5.75 mm pad-to-pad length serpentine connected with the 2.4 GHz ceramic antenna under different levels of strain. The resonance frequency shift slightly from 2.475 GHz (0% strain) to 2.461 GHz (80% strain) due to the serpentine interconnect deformation and the corresponding S11 amplitude decreases from -16.79 dB to -46.59 dB, which means less reflection loss when the interconnect is deformed from serpentine geometry (0% strain) to buckled geometry (80% strain).

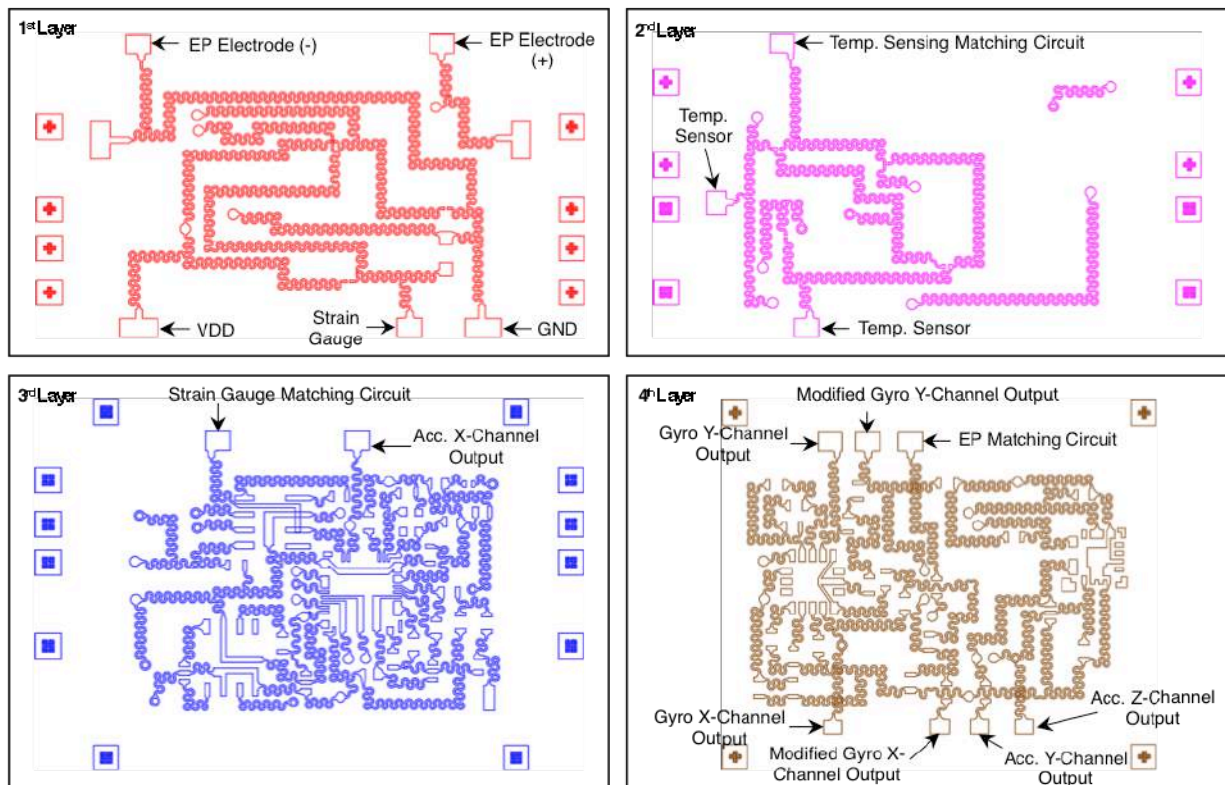


Supplementary Figure 55. The received-signal-strength-indicator (RSSI) of the Bluetooth signal from the multilayered device under strain from 0% to 44%. As the serpentine is very stable at low frequencies and is more sensitive to the strain when the frequency is higher than 10 MHz (Supplementary Figure 53), for the Bluetooth communication, we connect a 16 MHz oscillator to the BLE chip and a 2.4 GHz antenna is used for the wireless communication, which means the Bluetooth module may be the vulnerable part in the design. Therefore, we characterize the Bluetooth signal as a means for quantitative measurements of the multilayered system under strain. The received-signal-strength-indicator (RSSI) of the Bluetooth signal from the multilayered system is measured under different strain levels, with the receiver at a distance of several meters. It can be seen that the RSSI varied randomly from -75 dBm to -90 dBm with the strain from 0% to 44% of the entire system, which means the Bluetooth module work well with strain values up to 44%. For strain levels higher than 44%, the device is broken possibly due to the interconnect failure and no Bluetooth signal can be detected.

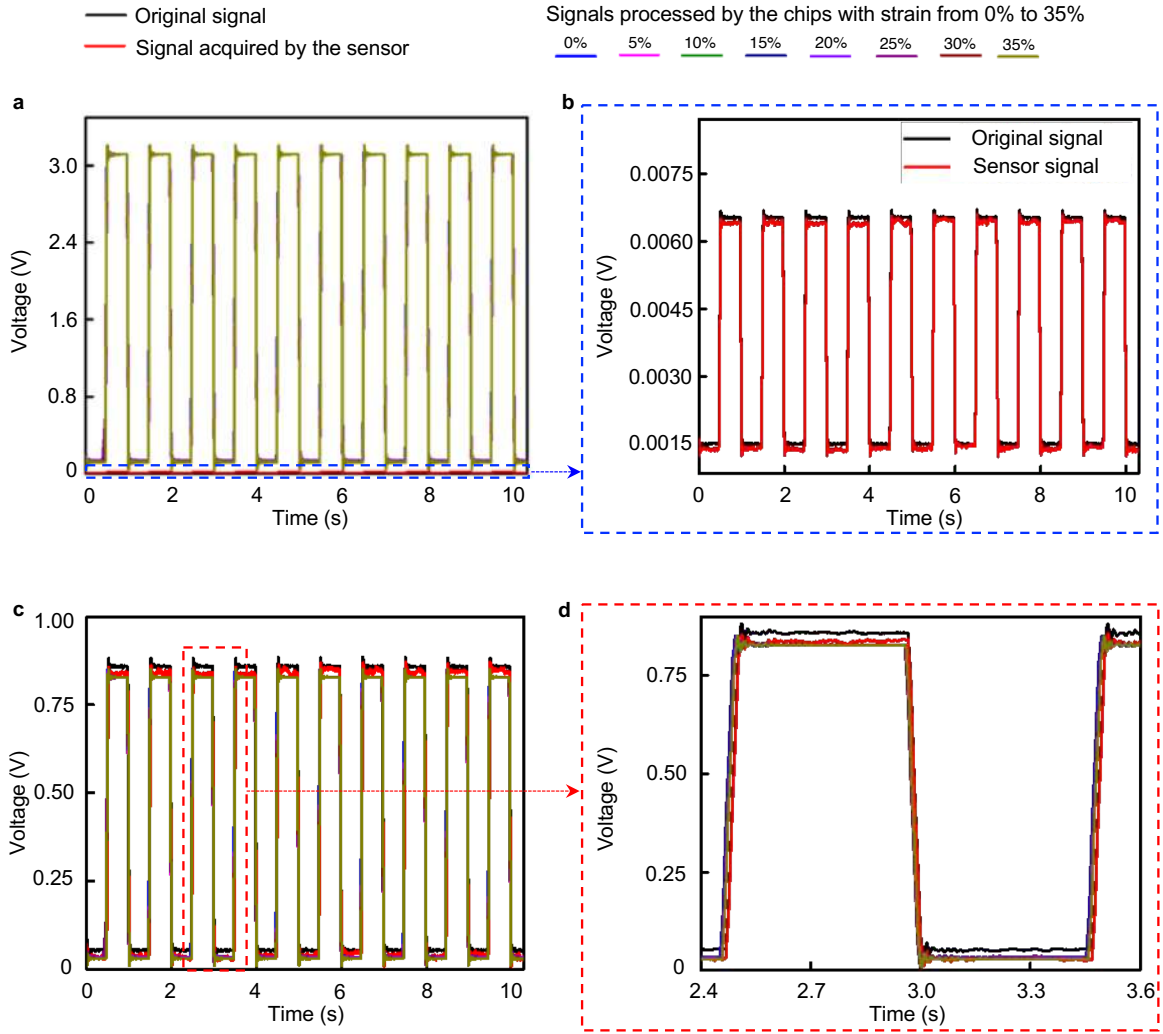
a



b

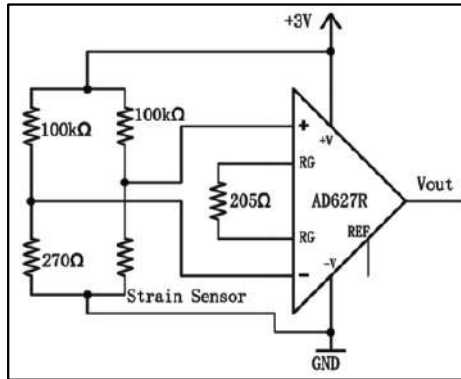


Supplementary Figure 56. The redesigned four-layer system with probing sites to evaluate the signal accuracy and quality acquired by the sensors and processed by the chips. a, Schematics showing the merged new multilayer design with probing sites embedded. **b,** Layout designs for each separated layer with probing sites labeled.

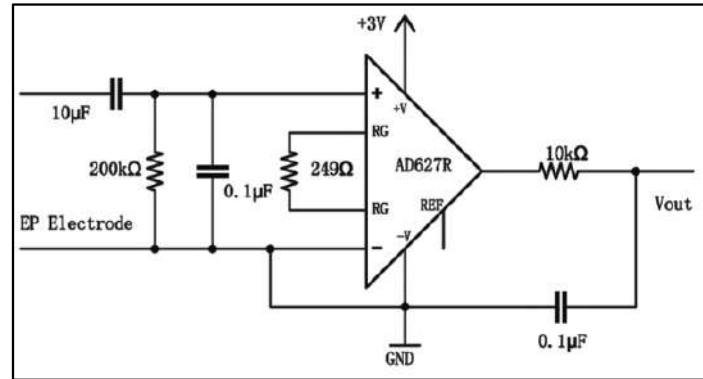


Supplementary Figure 57. Evaluation of signal accuracy and quality acquired by the sensors and processed by the chips with different levels of strain in the system. **a**, The comparison of the original signal, signals acquired by the sensor, and signals amplified for 508 times and filtered by the chips when the systems are under different levels of strain from 0% to 35%. **b**, Zoom-in view of the original signal and sensor signal. **c**, Normalized original, sensor, and chip processed signals with different levels of strain in the system, with the zoom-in view shown in **(d)**. The external strain has minimal impact on the device performance.

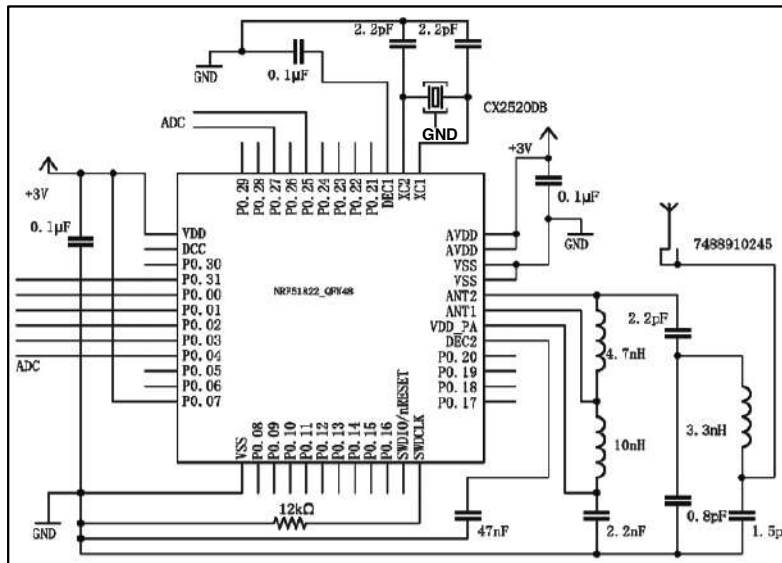
Strain sensor circuit diagram



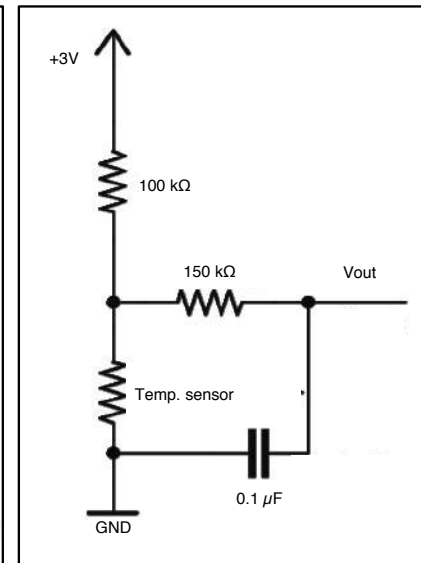
Epidermal potential circuit diagram



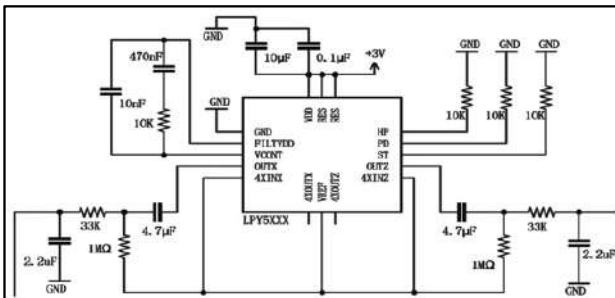
Bluetooth circuit diagram



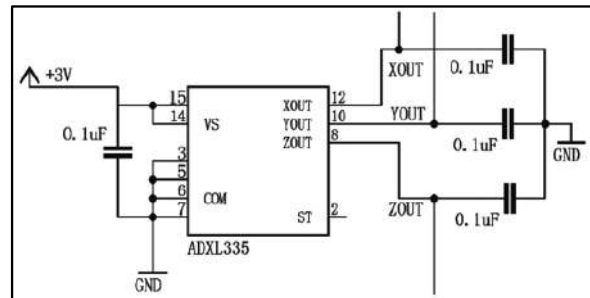
Temperature sensor circuit diagram



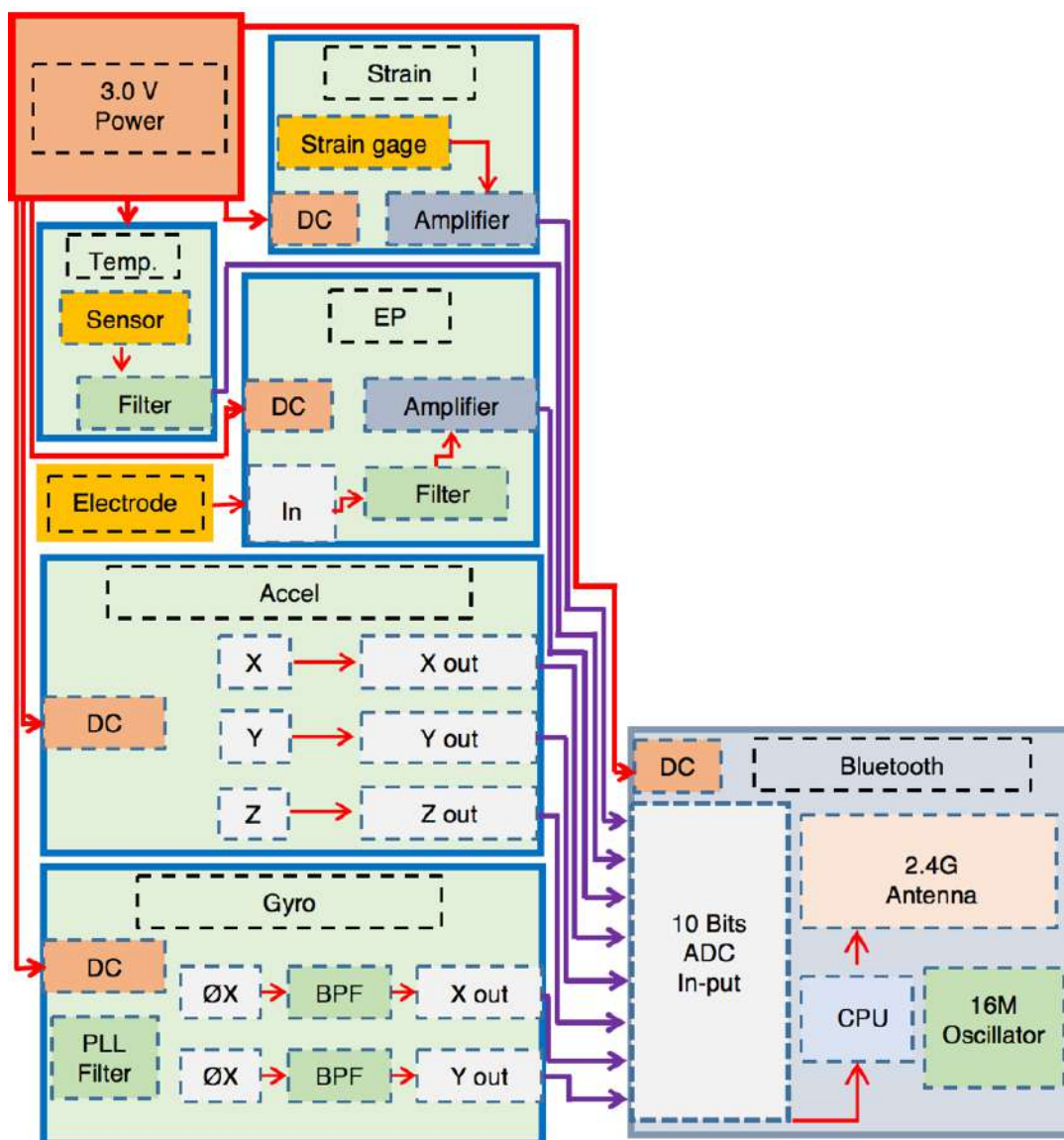
Gyroscope circuit diagram



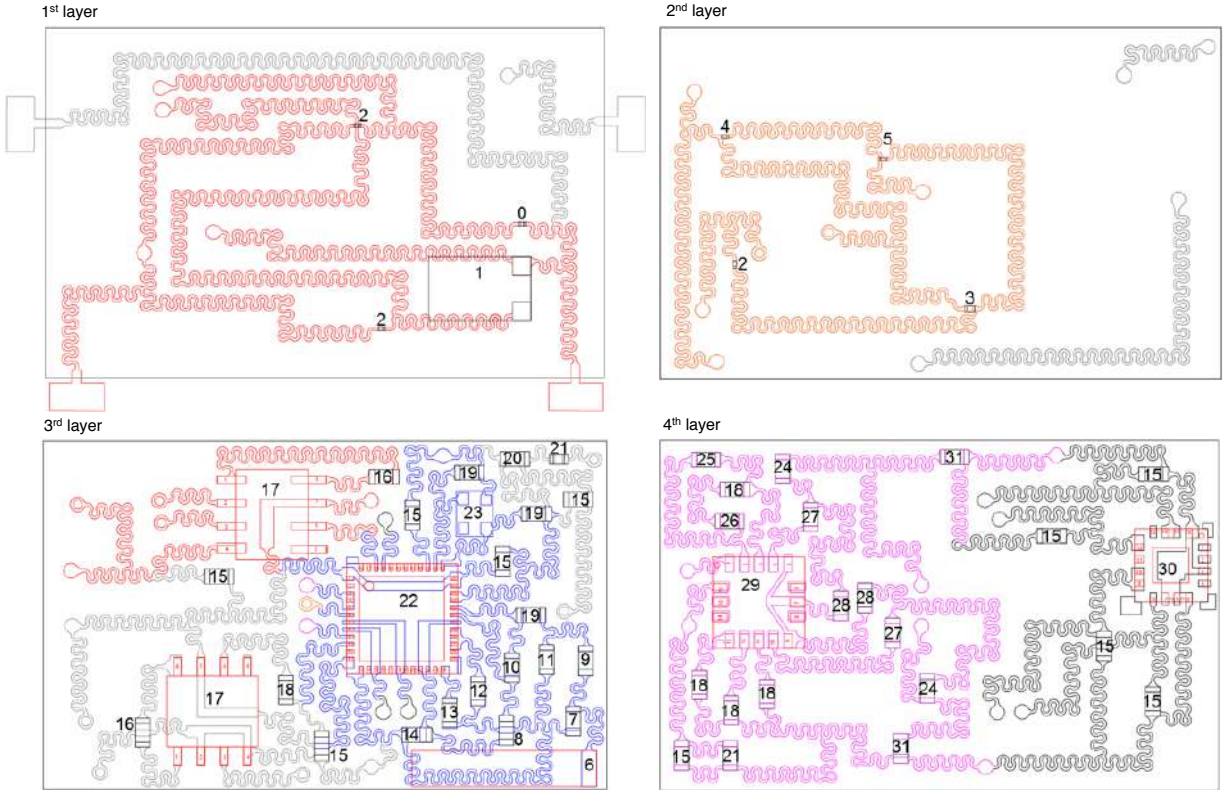
Accelerometer circuit diagram



Supplementary Figure 58. Summary of the circuit design for the multilayered stretchable system. There are mainly six parts: a strain gauge, an electrophysiological potential sensor, a temperature sensor, a two-channel posture sensor, a three-channel acceleration sensor, and the Bluetooth. Low power medical instrumentation amplifiers (AD627B) are used to amplify signals for the strain and EP sensors. A matching circuit is designed to adjust the impedance of the Bluetooth to match the 2.4 GHz antenna impedance (50 Ohm), which helps increase the Bluetooth signal strength.

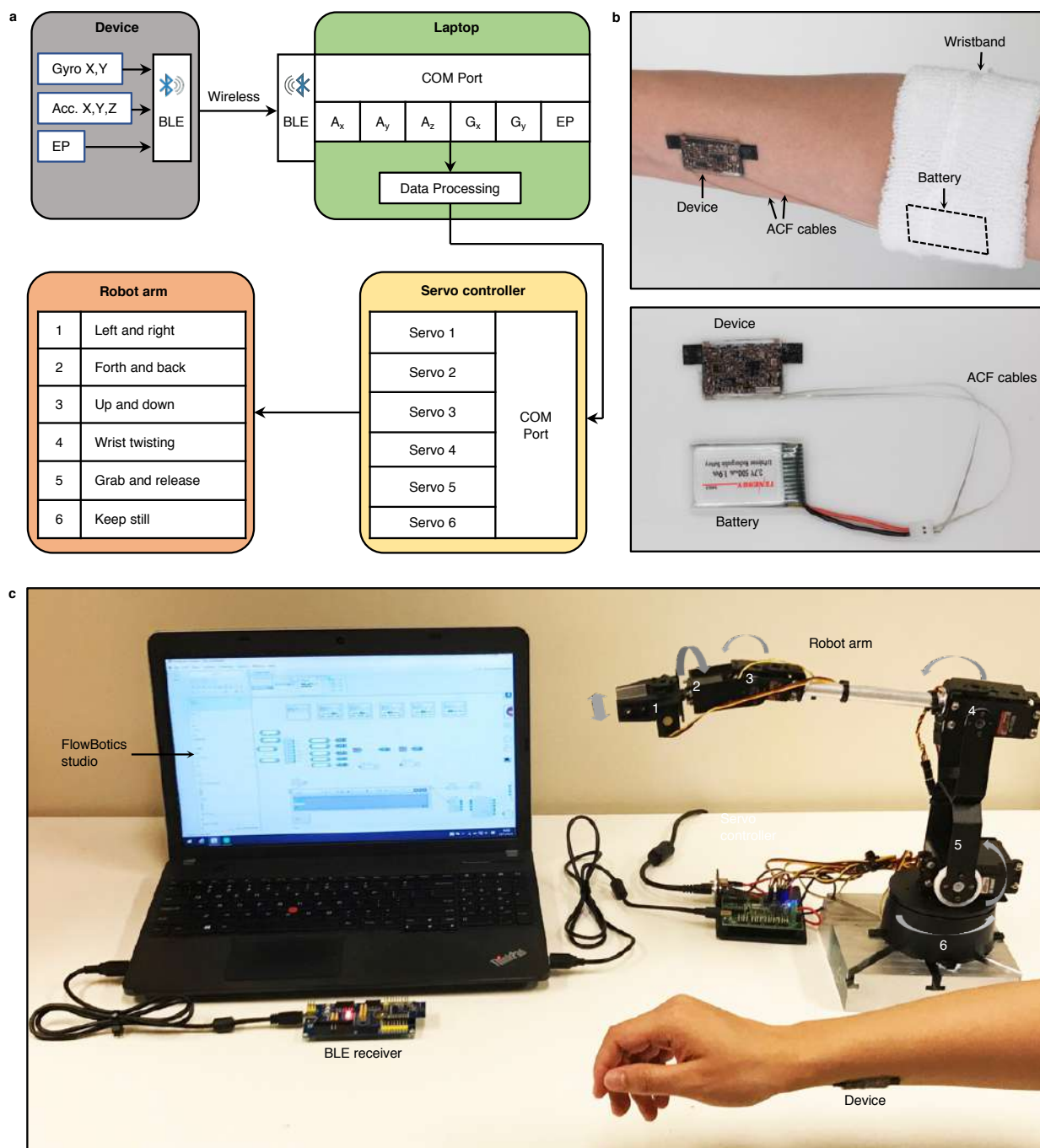


Supplementary Figure 59. Flow diagram showing the working principle of the multifunctional device. All the five sensing parts are connected with the Bluetooth for wireless data transmission. Analog sensing data are converted into digital signals with the built-in ADC from multi-protocol Bluetooth SOC (System on Chip). And then the data are transferred wirelessly with a 2.4 GHz antenna, oscillated by a 16 MHz external crystal. Both the sensing and wireless communication parts are powered by a 3 V battery.

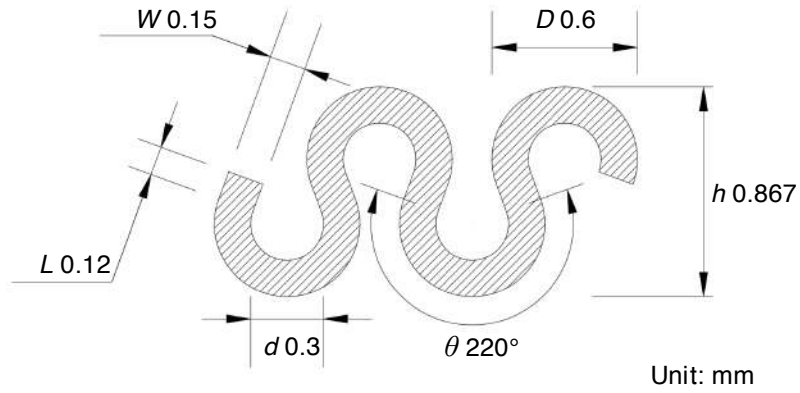


Device Number	Type	Value	Manufacturer Part Number	Device Number	Type	Value	Manufacturer Part Number
0	Resistor	270 Ohm	ERJ-XGNJ271Y	16	Resistor	249 Ohm	CR0603-FX-2490ELF
1	Strain sensor	N/A	BF350-3AA	17	Amplifier	N/A	AD627BRZ-R7
2	Resistor	100K Ohm	RC0402F104CS	18	Resistor	10K Ohm	CR0603-FX-1002HLF
3	Thermistor	N/A	NCP03WF104F05RL	19	Capacitor	2.2 pF	C0603C229C5GACTU
4	Capacitor	0.1 μ F	CL02A104KQ2NNNC	20	Resistor	200K Ohm	CR0603-JW-204ELF
5	Resistor	150K Ohm	ERJ-XGNJ154Y	21	Capacitor	10 μ F	GRM155C80J106ME11D
6	Antenna	N/A	7488910245	22	Bluetooth	N/A	NRF51822-QFAC-T
7	Capacitor	1.5 pF	CL10C1R5BB8NNNC	23	Crystal	N/A	CX2520DB16000D0GPSC1
8	Inductor	10 nH	L-14C10NJ4T	24	Resistor	33K Ohm	CR0603-FX-3302ELF
9	Inductor	3.3 nH	L-14C3N3SV4T	25	Capacitor	10 nF	GRM188R71H103KA01D
10	Inductor	4.7 nH	L-14C4N7SV4T	26	Capacitor	470 nF	C1608X7R1C474K080AC
11	Capacitor	0.8 pF	CL10C0R8BB8NNNC	27	Capacitor	4.7 μ F	CL10B475KQ8NQNC
12	Capacitor	47 nF	C0603C473K1RACTU	28	Resistor	1M Ohm	CR0603-JW-105ELF
13	Resistor	12K Ohm	CR0603-JW-123ELF	29	Gyro	N/A	LPR503ALTR
14	Capacitor	2.2 nF	GRM1885C1H222JA01D	30	Accelerometer	N/A	ADXL335BCPZ
15	Capacitor	0.1 μ F	GRM188R71C104KA01D	31	Capacitor	2.2 μ F	GRM188R61C225KE15D

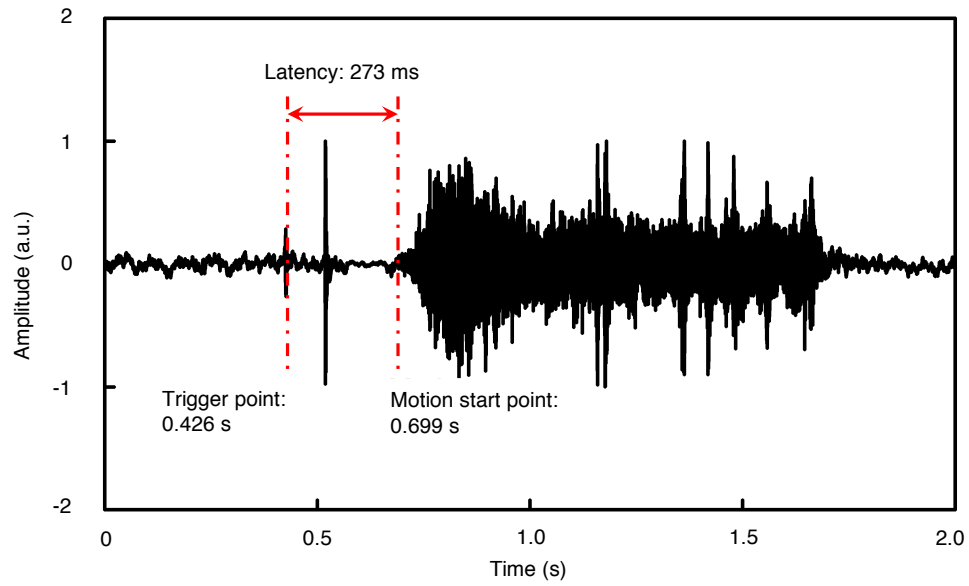
Supplementary Figure 60. Chip summary for the multilayered stretchable system. In total, 56 components, in 31 different types, are used in the design. All thick active components, such as the amplifiers, Bluetooth, antenna, gyroscope, and accelerometer, are integrated into the 3rd and 4th layer with an offset method to avoid direct overlap of thick chips.



Supplementary Figure 61. Robotic arm controlling system. **a**, Work flow of the controlling system. **b**, The device is powered by a lithium polymer battery connected by the anisotropic conductive film (ACF) cables. The battery is fixed on the arm by a wristband. **c**, A picture showing the overall setup of the controlling system.



Supplementary Figure 62. Mechanical pattern design of the serpentine electrodes. Horseshoe serpentine design is employed as the interconnect between the components, with 0.6 mm for external diameter (D), 0.3 mm for internal diameter (d), 220° for curvature (θ), 0.12 mm for ribbon length (L), and 0.15 mm for ribbon width (W). The total height of each horseshoe h is 0.867 mm.



Supplementary Figure 63. The latency of the commercial robotic arm hardware and software. To quantify the delay from the robotic arm hardware (Lynxmotion AL5D arm with upgraded wrist rotate) and software (FlowBotics Studio), the audio signal of the system is recorded and the time between the trigger command and robot arm motion starting point is identified to be the robot system latency, which is around 273 ms.

Supplementary References

1. Ma, Y. et al. Soft Elastomers with Ionic Liquid-Filled Cavities as Strain Isolating Substrates for Wearable Electronics. *Small* **13**, (2017).
2. Tang, J., Li, J., Vlassak, J. J. & Suo, Z. Adhesion between highly stretchable materials. *Soft Matter* **12**, 1093-1099, (2016).
3. Li, J. et al. Tough adhesives for diverse wet surfaces. *Science* **357**, 378-381, (2017).
4. Johnson, H., Johnson, H. W. & Graham, M. *High-speed signal propagation: advanced black magic*, (2003).
5. Lin, Y. et al. Advances toward bioapplications of carbon nanotubes. *Journal of Materials Chemistry* **14**, 527-541, (2004).
6. Garibaldi, S., Brunelli, C., Bavastrello, V., Ghigliotti, G. & Nicolini, C. Carbon nanotube biocompatibility with cardiac muscle cells. *Nanotechnology* **17**, 391, (2005).
7. Park, Y.-H. et al. Assessment of dermal irritation potential of MWCNT. *Toxicology and Environmental Health Sciences* **2**, 115-118, (2010).
8. Ema, M., Matsuda, A., Kobayashi, N., Naya, M. & Nakanishi, J. Evaluation of dermal and eye irritation and skin sensitization due to carbon nanotubes. *Regulatory Toxicology and Pharmacology* **61**, 276-281, (2011).
9. Grunlan, J. C., Mehrabi, A. R., Bannon, M. V. & Bahr, J. L. Water-Based Single-Walled-Nanotube-Filled Polymer Composite with an Exceptionally Low Percolation Threshold. *Advanced Materials* **16**, 150-153, (2004).
10. Huang, J.-E., Li, X.-H., Xu, J.-C. & Li, H.-L. Well-dispersed single-walled carbon nanotube/polyaniline composite films. *Carbon* **41**, 2731-2736, (2003).
11. Supronowicz, P. et al. Novel current-conducting composite substrates for exposing osteoblasts to alternating current stimulation. *Journal of Biomedical Materials Research Part A* **59**, 499-506, (2002).
12. Jung, H.-C. et al. CNT/PDMS composite flexible dry electrodes for long-term ECG monitoring. *IEEE Transactions on Biomedical Engineering* **59**, 1472-1479, (2012).
13. Lam, C.-W., James, J. T., McCluskey, R. & Hunter, R. L. Pulmonary toxicity of single-wall carbon nanotubes in mice 7 and 90 days after intratracheal instillation. *Toxicological Sciences* **77**, 126-134, (2004).
14. Warheit, D. B. et al. Comparative pulmonary toxicity assessment of single-wall carbon nanotubes in rats. *Toxicological Sciences* **77**, 117-125, (2004).
15. Huczko, A. et al. Pulmonary Toxicity of 1-D Nanocarbon Materials. *Fullerenes, Nanotubes, and Carbon Nanostructures* **13**, 141-145, (2005).
16. Muller, J. et al. Respiratory toxicity of multi-wall carbon nanotubes. *Toxicology and Applied Pharmacology* **207**, 221-231, (2005).
17. Fan, J. A. et al. Fractal design concepts for stretchable electronics. *Nat. Commun.* **5**, 3266, (2014).
18. Aoki, H. Laser processing method to form an ink jet nozzle plate. (1998).
19. Bohme, R. & Zimmer, K. Laser fabrication of micro sized diffractive and refractive optical devices in fused silica and glass. *CLEO/Europe IEEE Cat.* 688, (2003).
20. Klank, H., Kutter, J. P. & Geschke, O. CO₂-laser micromachining and back-end processing for rapid production of PMMA-based microfluidic systems. *Lab on a Chip* **2**, 242-246, (2002).

21. Itzkan, I. et al. The thermoelastic basis of short pulsed laser ablation of biological tissue. *Proceedings of the National Academy of Sciences of the United States of America* **92**, 1960-1964, (1995).
22. Patel, R. S. & Wassick, T. A. Laser processes for multichip module's high-density multilevel thin film packaging. **2991**, 217-223, (1997).
23. Cho, K. *et al.* Analysis of latency performance of Bluetooth low energy (BLE) networks. *Sensors* **15**, 59-78, (2014).